1-1-2014

Three Dimensional Dirac Semimetals

Saad Zaheer
University of Pennsylvania, saadzaheer@alum.mit.edu

Three Dimensional Dirac Semimetals

Abstract
We extend the physics of graphene to three dimensional systems by showing that Dirac points can exist on the Fermi surface of realistic materials in three dimensions. Many of the exotic electronic properties of graphene can be ascribed to the pseudorelativistic behavior of its charge carriers due to two dimensional Dirac points on the Fermi surface. We show that certain nonsymmorphic spacegroups exhibit Dirac points among the irreducible representations of the appropriate little group at high symmetry points on the surface of the Brillouin zone. We provide a list of all Brillouin zone momenta in the 230 spacegroups that can host Dirac points.

We describe microscopic considerations necessary to design materials in one of the candidate spacegroups such that the Dirac point appears at the Fermi energy without any additional non-Dirac-like Fermi pockets. We use density functional theory based methods to propose six new Dirac semimetals: BiO_2 and SbO_2 in the β-cristobalite lattice (spacegroup 227), and $BiCaSiO_4$, $BiMgSiO_4$, $BiAlInO_4$, and $BiZnSiO_4$ in the distorted spinels lattice (spacegroup 74). Additionally we derive effective Dirac Hamiltonians given group representative operators as well as tight binding models incorporating spin-orbit coupling.

Finally we study the Fermi surface of zincblende (spacegroup 216) HgTe which is effectively point-like at Γ in the Brillouin zone and exhibits accidental degeneracies along a threefold rotation axis. Whereas compressive strain gaps the band structure into a topological insulator, tensile strain shifts the accidental degeneracies away from Γ and enlarges the Fermi surface. States on the Fermi surface exhibit nontrivial spin texture marked by winding of spins around the threefold rotation axis and by spin vortices indicating a change in the winding number. This is confirmed by microscopic calculations performed in tensile strained HgTe and $Hg_{0.5}Zn_{0.5}$ Te as well as **k.p** theory.

We conclude with a summary of recent work on the physics of Dirac semimetals especially after the observation of the topological Dirac semimetals Cd_3As_2 and Na_3Bi and outline topics for future research. Symmetry protected Dirac semimetals, on the other hand, have yet to be observed experimentally.

Degree Type
Dissertation

Degree Name
Doctor of Philosophy (PhD)

Graduate Group
Physics & Astronomy

First Advisor
Eugene J. Mele

Keywords
Diamond, Dirac Semimetals, Graphene, Spacegroup representations, Weyl Semimetals, Zincblende

THREE DIMENSIONAL DIRAC SEMIMETALS

Saad Zaheer

A DISSERTATION

in

Physics and Astronomy

Presented to the Faculties of the University of Pennsylvania

in

Partial Fulfillment of the Requirements for the

Degree of Doctor of Philosophy

2014

Supervisor of Dissertation

Eugene J. Mele
Professor of Physics

Graduate Group Chairperson

Marija Drndic, Professor of Physics

Dissertation Committee

Mirjam Cvetic, Fay R. and Eugene L. Langberg Professor of Physics
Charles L. Kane, Class of 1965 Endowed Term Chair Professor of Physics
Justin Khoury, Associate Professor of Physics
Tom C. Lubensky, Christopher H. Browne Distinguished Professor of Physics

THREE DIMENSIONAL DIRAC SEMIMETALS

Dedicated to the memory of my great grandparents and their children, accomplished religious scholars in their own right whose lives were so untimely cut short a century ago, and to my parents who have, through enormous personal sacrifices, enabled rekindling of the scholarly tradition within our family.

ACKNOWLEDGEMENTS

This dissertation could not have been completed without the help and support of many wonderful people in my academic and personal life. First and foremost, I would like to thank my advisor, Prof. Eugene Mele, for his mentorship, support, and kindness. Prof. Mele allowed me unfettered freedom to pursue any problems or projects I desired, and gave me complete ownership of our work from conception to completion. Under his supervision, I have learned not only how to solve problems but how to conceive research projects, chart a path for their solution, and bring them to completion. Prof. Mele's limitless generosity in giving me his time and attention during our numerous discussions has benefitted me tremendously. His affability is evidenced by the fact that I barely recall ever making an appointment to speak with him, but I have knocked on his door countless times without being turned away. I do not believe that many doctoral students are so lucky as to have had so much of their advisors' time. My lifelong regret will be not to have made sufficient use of it.

I am grateful for the fact that I worked under the combined supervision of Profs. Charles Kane and Andrew M. Rappe in addition to Prof. Mele. I want to thank Prof. Kane for the many hours of discussions during our Friday meetings and otherwise, for asking foundational questions that underlie the bulk of my research on Dirac points, and for patiently answering all of my questions. Prof. Kane's presence in our group and willingness to share so much of his precious time have been priceless assets during my educational journey through Penn. I would also like to thank Prof. Andrew M. Rappe for allowing me the opportunity to collaborate with his many gifted colleagues and students, for hosting our group in the Chemistry quarters every Friday, and for his leadership on shepherding our projects to completion. Prof. Rappe's probing insights

on topological insulators and unique perspective and experience in materials design were extremely useful during the herculean task of designing symmetry protected Dirac semimetals.

I am highly indebted to my friend and colleague Prof. Jeffrey Teo who has patiently taught me everything I know about topological band theory and has inspired many ideas discussed in this dissertation. I am also highly indebted to my friend and colleague Dr. Steve Young, who not only performed almost all the numerical calculations, but contributed heavily towards the analytical understanding of Dirac points. I have been fortunate to have had a colleague in Steve who is an excellent physicist as well as a remarkable chemist. I would also like to thank Mr. Daniel Cellucci, Ms. Julia Steinberg, Dr. Dmitry Volja, and Dr. Sugata Chowdhury whom I have collaborated with directly, and Dr. Fan Zhang and Ms. Madeleine Phillips who have through numerous insights and useful discussions made research at Penn such a pleasurable experience.

I would like to thank the physics department for their generosity, especially for trusting me to TA advanced graduate level courses given my lack of preparation at times and for my selfish desire to learn by teaching. I would like to thank Prof. Burt Ovrut, Prof. Justin Khoury, Prof. Charles Kane, and Prof. Arjun Yodh for allowing me to interact with students in their classes. I have learned a great deal from these experiences. Finally, I would like to thank Prof. Tom Lubensky, Prof. Randall Kamien, Prof. Mark Trodden, and Prof. Mirjam Cvetic for their instruction on various subjects in theoretical physics.

I would like to thank my family for their undying love and support. My mother, Ms. Farhat Zaheer, and my father, Mr. Zaheer Ahmad, have made tremendous personal

sacrifices to enable me to pursue my dreams from a very young age. They gave me the freedom to pursue any career paths I chose, and with enormous forbearance have lived through the separation of their only son for the last fifteen years. My dearest sisters, Dr. Misbah Zaheer, Ms. Muniba Zaheer, and Ms. Mashal Zaheer have constantly supported me and never once failed to lend an ear to listen. I would especially like to thank Dr. Zaheer for her hospitality and generosity in sharing her beautiful home and family with me during numerous weekend visits to Virginia.

I am fortunate to have another set of parents in my aunt, Ms. Nuzhat Shaheen, and her husband, Mr. Mohammad M. Khan. Aunt Nuzhat's unending generosity and graciousness in welcoming me to her home in New Jersey every weekend during the past five years has blunted any sense of being away from my family. I have a second home to call my own in the Khan household for which I am eternally grateful.

Last, I would like to thank my dear friends in Philadelphia. Mr. Hernan Piragua, Mr. Prashant Subbarao, Ms. Stephanie Cheng, Mr. Garrett Hemann, Mr. Seleeke Flingai, Ms. Kathleen Kozak, Dr. Rose Mutiso, Mr. Kory Johnson, Mr. Diomedes Saldana-Greco, Mr. Ahmad Iqbal Chaudhary, Dr. Brendon Baker, Prof. Jacob Abernethy, Ms. Liwei Xu, Mr. James Stokes, Mr. Zain Saleem, Mr. Ali Zaidi, Mr. Barry Slaff, Mr. Barlow Holley, Dr. Adrian Balan, Mr. Mehmet Noyan, Ms. Ashley Reichardt, Mr. Noah Rahman, Ms. Alexandra Savoy-Knitter, Ms. Mariam Naeem, Ms. Asja Radja, and Ms. Joanna Flores have made living in Philadelphia a memorable experience and I am going to miss them all very much. My dearest friends from college who despite being scattered across the country continue to encourage my work and inspire me everyday: Prof. Zeeshan Syed, Mr. Rehan Tahir, Dr. Ebad Ahmed, Dr. Daanish Maqbool, Mr. Shakeel Avadhany, Mr. Arya Tafvizi, Mr. Michael Zomnir, and Dr. Jerzy Szablowski; I remain your most humble servant.

ABSTRACT

THREE DIMENSIONAL DIRAC SEMIMETALS

Saad Zaheer

Eugene J. Mele

We extend the physics of graphene to three dimensional systems by showing that Dirac points can exist on the Fermi surface of realistic materials in three dimensions. Many of the exotic electronic properties of graphene can be ascribed to the pseudorelativistic behavior of its charge carriers due to two dimensional Dirac points on the Fermi surface. We show that certain nonsymmorphic spacegroups exhibit Dirac points among the irreducible representations of the appropriate little group at high symmetry points on the surface of the Brillouin zone. We provide a list of all Brillouin zone momenta in the 230 spacegroups that can host Dirac points.

We describe microscopic considerations necessary to design materials in one of the candidate spacegroups such that the Dirac point appears at the Fermi energy without any additional non-Dirac-like Fermi pockets. We use density functional theory based methods to propose six new Dirac semimetals: BiO_2 and SbO_2 in the β-cristobalite lattice (spacegroup 227), and $BiCaSiO_4$, $BiMgSiO_4$, $BiAlInO_4$, and $BiZnSiO_4$ in the distorted spinels lattice (spacegroup 74). Additionally we derive effective Dirac Hamiltonians given group representative operators as well as tight binding models incorporating spin-orbit coupling.

Finally we study the Fermi surface of zincblende (spacegroup 216) HgTe which is effectively point-like at Γ in the Brillouin zone and exhibits accidental degeneracies

along a threefold rotation axis. Whereas compressive strain gaps the band structure into a topological insulator, tensile strain shifts the accidental degeneracies away from Γ and enlarges the Fermi surface. States on the Fermi surface exhibit nontrivial spin texture marked by winding of spins around the threefold rotation axis and by spin vortices indicating a change in the winding number. This is confirmed by microscopic calculations performed in tensile strained HgTe and $Hg_{0.5}Zn_{0.5}Te$ as well as $\mathbf{k} \cdot \mathbf{p}$ theory.

We conclude with a summary of recent work on the physics of Dirac semimetals especially after the observation of the topological Dirac semimetals Cd_3As_2 and Na_3Bi and outline topics for future research. Symmetry protected Dirac semimetals, on the other hand, have yet to be observed experimentally.

TABLE OF CONTENTS

LIST OF TABLES

LIST OF ILLUSTRATIONS

PREFACE

This dissertation is based on research conducted at the University of Pennsylvania during the period from 2010 through 2014. A bulk of ideas presented here have already appeared in the following journal articles, which we attach as appendices at the end of this dissertation for reference,

1. *Dirac semimetal in three dimensions.* (Young et al., 2012)

2. *Spin texture on the Fermi surface of tensile-strained HgTe.* (Zaheer et al., 2013)

3. *Bulk Dirac points in distorted spinels.* (Steinberg et al., 2014)

Certain passages that appear in Chapters 4 and 5 have been quoted verbatim from the above papers.

Chapter 1 begins with an introduction to the idea of Dirac points, defines what we mean by symmetry protected Dirac semimetals, and contrasts them with topological Dirac semimetals and Weyl semimetals. Chapter 2 describes the underlying theory behind the existence of three dimensional Dirac points. Section 2.2 introduces the representation theory of spacegroups while Section 2.3 demonstrates methods to construct Dirac Hamiltonians given a specific group representation. Brief references to the contents of Chapter 2 have appeared in the journal articles and presentations given by this author but a complete description of the underlying theory as it is applied to three dimensional Dirac points in crystalline solids appears in this dissertation for the first time. Therefore, I have attempted to give as many details of the calculations as possible.

Chapter 3 provides a complete list of all the Brillouin zone momenta in the 230 space-groups that can host Dirac points. Besides the high symmetry points, the list includes other details about every little group to make our description self-contained and avoid the need for reference books to go along with the reading of this dissertation. Group character tables and representative operators are, however, omitted. Representation theory of crystallographic spacegroups is a fascinating subject studied by many authors, an unhappy consequence of which has been an abundance of notation used to classify symmetry groups and their attributes. We have not attempted to create a new naming convention however, and used notation chosen by Bradley and Cracknell (1976).

Chapters 4 and 5 contain most of the results already published in the journal articles mentioned above. To this end, the author is indebted to the efforts and contributions of his collaborators and has borrowed from their results to make the description self-contained. We would be remiss without acknowledging that almost all the density functional theory calculations were performed by Dr. Steve Young, Ms. Julia Steinberg, and Mr. Daniel Cellucci. Certain key details concerning the derivation of $\mathbf{k} \cdot \mathbf{p}$ theories that were omitted in the journal articles listed above have been added to Chapters 4 and 5.

Chapter 6 concludes with a review of some fascinating research on the physics of Dirac points that has come to the fore after our seminal study (Young et al., 2012). We discuss a number of unanswered questions with the hope of inspiring further research into the physics of Dirac semimetals.

Chapter 1

Introduction

This dissertation is devoted to the study of Dirac points in three dimensional solids arising as a consequence of crystallographic symmetry. Following the discovery of topological insulators in two (Kane and Mele, 2005a,b; Konig et al., 2007) and three dimensions (Hasan and Kane, 2010; Fu et al., 2007; Moore and Balents, 2007; Roy, 2009; Zhang et al., 2009; Hsieh et al., 2009), there has been considerable interest, besides numerous related topics, in the study of semimetallic phases that mediate the phase transition (band inversion) between a topological and a normal insulator. In a three dimensional solid, a band inversion tuned by a single parameter can be described in terms of a pseudorelativistic Dirac-like Hamiltonian, where energy is linearly proportional to momentum and the size of the mass term sets the band gap while its sign distinguishes between the topology of the band insulator (Murakami, 2007; Young et al., 2011). We are interested in the special case when the mass term equals zero, and the ensuing band degeneracy looks like a point with linearly dispersing energy bands as a function of momentum.

Thus we define a Dirac semimetal as a material where the Fermi surface consists of fourfold degenerate points at specific momenta in the Brillouin zone (BZ) and the energy bands disperse linearly as a function of momentum in the vicinity of these points. Throughout the following pages, we assume that spin-orbit coupling is present and, consequently, the fourfold degeneracy includes spin. This distinction is not absolutely necessary and Dirac semimetals may well arise in systems where spin-orbit coupling is negligible and all states are spin degenerate (Mañes, 2012) but we ignore that

possibility in order to allow the Dirac semimetal to make contact with topological insulating as well as normal insulating states. We make such restrictive assumptions to focus on systems that lie at a multi-critical point between various insulating as well as semimetallic phases; for example, breaking symmetries or tuning phenomenological parameters can turn a Dirac semimetal into a topological insulator, a Weyl semimetal, a quantum Hall insulator, as well as a quantum anomalous Hall insulator (Xu et al., 2011) in addition to a normal insulator. Figure 1.1 shows the various topological insulating and semimetallic phases obtained by adding perturbations to the Dirac semimetal state in BiO_2. Therefore, it is a valuable exercise to try to identify crystallographic systems that exhibit Dirac points and design materials within these systems that exhibit those Dirac points on the Fermi surface. This we have attempted to do in this dissertation.

Our study has also been motivated by the remarkable electronic properties due to the two dimensional Dirac points at the Fermi energy in graphene (Fig. 1.2). The theoretical study of graphene goes back many decades (Wallace, 1947), but its experimental realization ten years ago (Novoselov et al., 2004) sparked tremendous research activity leading to many important advancements in condensed matter physics and elsewhere (Castro Neto et al., 2009). Dirac points in graphene are protected by a combination of time reversal and inversion symmetries. Although both time reversal and inversion are symmetries of bulk graphene, the special points (zone corners) where the Dirac points occur are not invariant under either time reversal or inversion separately. However, the zone corners are invariant under a product of time reversal and inversion and this product symmetry protects the Dirac point. We further note that the Dirac points in graphene are not protected in the presence of spin-orbit coupling; a critical fact behind the realization of two dimensional topological insulators (Kane

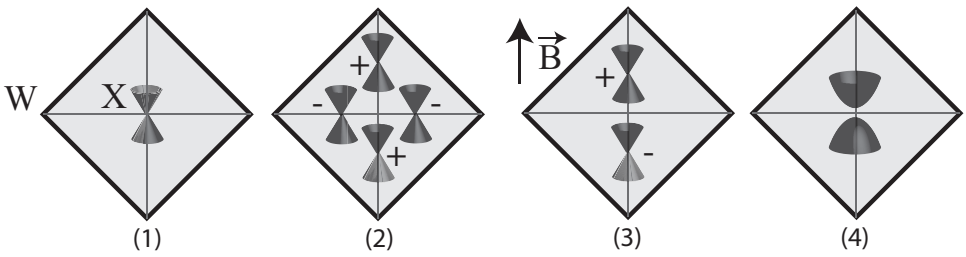

Figure 1.1: Dirac, Weyl and insulating phases in the diamond lattice indicated by conical bands shown on a Brillouin zone face. Figure 4.1 shows the full Brillouin zone of the diamond lattice. (1) States at the Dirac point at X span a four dimensional projective representation of the little group at X. (2) Four Weyl points on the zone face due to a small inversion breaking perturbation. The Chern number of each Weyl point is indicated. (3) Two Weyl points appear on the line from X to W for a time-reversal-symmetry-breaking Zeeman field **B** oriented along that direction. **B** oriented along other directions gaps the Dirac point because of broken rotation symmetry. (4) Gapped phase obtained by breaking the fourfold rotation symmetry or by applying a magnetic field in any direction except along $\hat{x}$, $\hat{y}$, or $\hat{z}$. The insulating phase can be a normal, strong or a weak topological insulator (Fu et al., 2007).

and Mele, 2005b). The three dimensional Dirac points discussed in this dissertation are protected despite the presence of spin-orbit coupling.

It is natural to ask whether the physics of graphene can be extended to a three dimensional solid. The degeneracy of bands that mediate the transition between the topological and normal insulating phase in Bi_2Se_3 provides an example (Young et al., 2011) of such a three dimensional Dirac point. But this Dirac point is not protected by any symmetries. Therefore, we ask if it is possible to find a realistic system where a three dimensional Dirac point is protected by a symmetry, as in graphene. A phenomenological model of *s*-electrons on the diamond lattice provides an existence proof for such a three dimensional Dirac point (Fu et al., 2007), underlying most of the results presented in this dissertation.

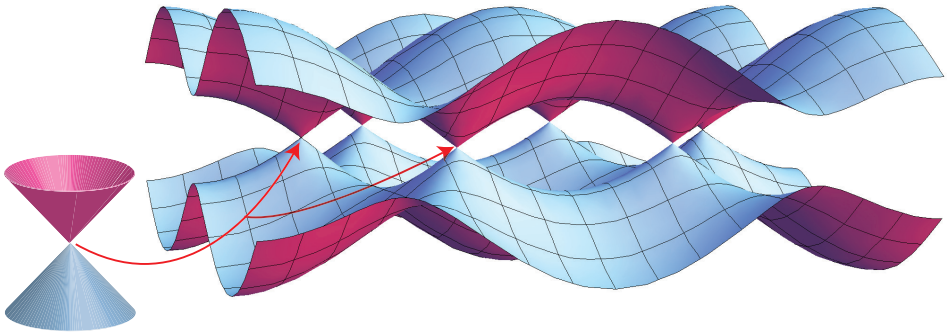

Figure 1.2: Dirac points in graphene. Energy bands $\mathcal{E}(\mathbf{k})$ in a phenomenological tight-binding model are plotted as a function of the two dimensional momentum coordinates (k_x, k_y). Valence and conduction bands are degenerate at the zone corners and the bands disperse linearly in $\mathbf{k}$ around those points. Degeneracy at the zone corner is protected by the product symmetry $\mathcal{P}\Theta$ where $\mathcal{P}$ and Θ are inversion and time reversal symmetries respectively.

1.1. Types of Dirac points

Since the publication of our seminal study of symmetry protected Dirac points in a three dimensional material (Young et al., 2012), a number of authors have investigated other mechanisms under which Dirac points may arise (Wang et al., 2012, 2013). At the outset, we outline differences and similarities between the research presented here and results obtained by other authors.

- **Symmetry protected Dirac points.** These Dirac points occur at high symmetry points in the Brillouin zone and are protected by crystallographic symmetries. Addition of a mass term to the effective Hamiltonian is analogous to breaking a crystallographic symmetry and can give rise to strong topological, weak topological, and normal insulating as well as the Weyl semimetal phase. Such Dirac points have been shown to exist using density functional theory methods in $BiO_2, SbO_2, BiZnSiO_4, BiMgSiO_4, BiCaSiO_4$ and $BiAlInO_4$ (Young

et al., 2012; Steinberg et al., 2014). Figure 1.3 shows the three Dirac points on the Fermi surface of BiO_2 on a specific plane in the BZ that connects the three X points. Symmetry protected Dirac points are yet to be discovered experimentally.

- **Dirac points due to band inversion.** These Dirac points can occur anywhere in the BZ as long as inversion symmetry is present and a phenomenological parameter such as the strength of the spin-orbit coupling or tensile strain etc. is tuned to a critical value. Addition of a mass term to the effective Dirac Hamiltonian is analogous to perturbing the value of a phenomenological parameter and can give rise to strong topological, weak topological, and normal insulating as well as the Weyl semimetal phase. Examples of such Dirac points are generally found during the phase transition between a topological and a normal insulator (Young et al., 2011; Sa et al., 2012; Liu et al., 2014a). A bulk Dirac point at the topological quantum phase transition was reported experimentally in $TlBi(S_{1-x}Se_x)_2$ (Sato et al., 2011) upon the acquisition of a mass gap by the surface Dirac cone as the bulk bands tuned into the normal insulating regime.

- **Dirac points due to band inversion and symmetry.** These Dirac points occur along high symmetry lines in the BZ such as threefold or fourfold rotation axes, but the occurrence of a high symmetry line is not sufficient to guarantee their existence. A critical ingredient is the tuning of a phenomenological parameter such as spin-orbit coupling or tensile strain to a range of critical values such that bands with distinct eigenvalues under said rotation symmetry intersect with each other and are protected from hybridizing due to the orthogonality of their representations under the rotation group. Addition of a mass term to the effective Dirac Hamiltonian is analogous to a perturbation that breaks the

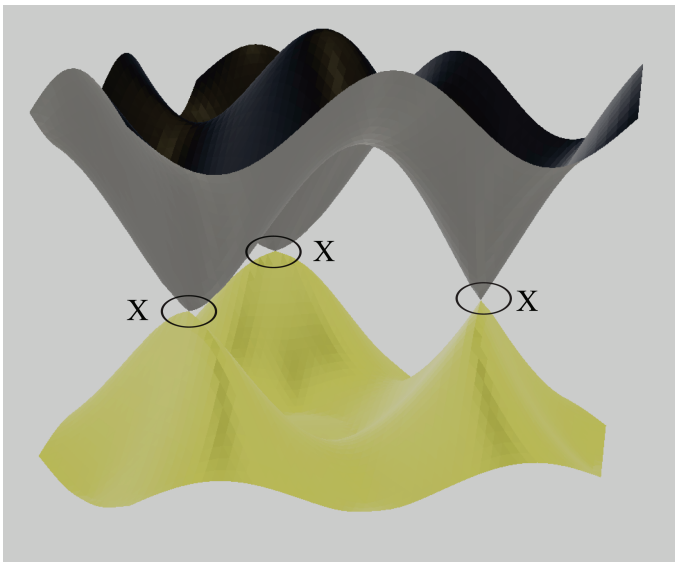

Figure 1.3: 3D Dirac semimetal in β-cristobalite BiO_2. Although the Dirac points are three dimensional, the conduction and valence bands $\mathcal{E}(\mathbf{k}_\parallel, k_\perp)$ are plotted as a function of $\mathbf{k}_\parallel$ while $k_\perp$ is fixed and defines a plane connecting the three X points in the BZ (Fig. 4.1). Each band is twofold degenerate due to inversion symmetry. Dirac points appear at the center of the three zone faces of the BZ.

rotation symmetry protecting the degeneracy between inverted bands and can give rise to a strong topological, weak topological, or a Weyl semimetal phase. These Dirac points come in pairs, and cannot be gapped to obtain a normal insulator under weak perturbations. Therefore, such Dirac points have been termed topological. Figure 1.4 provides a schematic illustration of the mechanism behind topological Dirac semimetals. Thus far, topological Dirac semimetals have been predicted to exist in Cd_3As_2, Na_3Bi, K_3Bi and Rb_3Bi (Wang et al., 2012, 2013), while Cd_3As_2 and Na_3Bi have been found to exhibit bulk three dimensional Dirac points experimentally (Neupane et al., 2014; Borisenko et al., 2013; Liu et al., 2014b).

The focus of this dissertation is on symmetry protected Dirac points. In particular, we will investigate crystallographic symmetry criteria that allow the possibility of

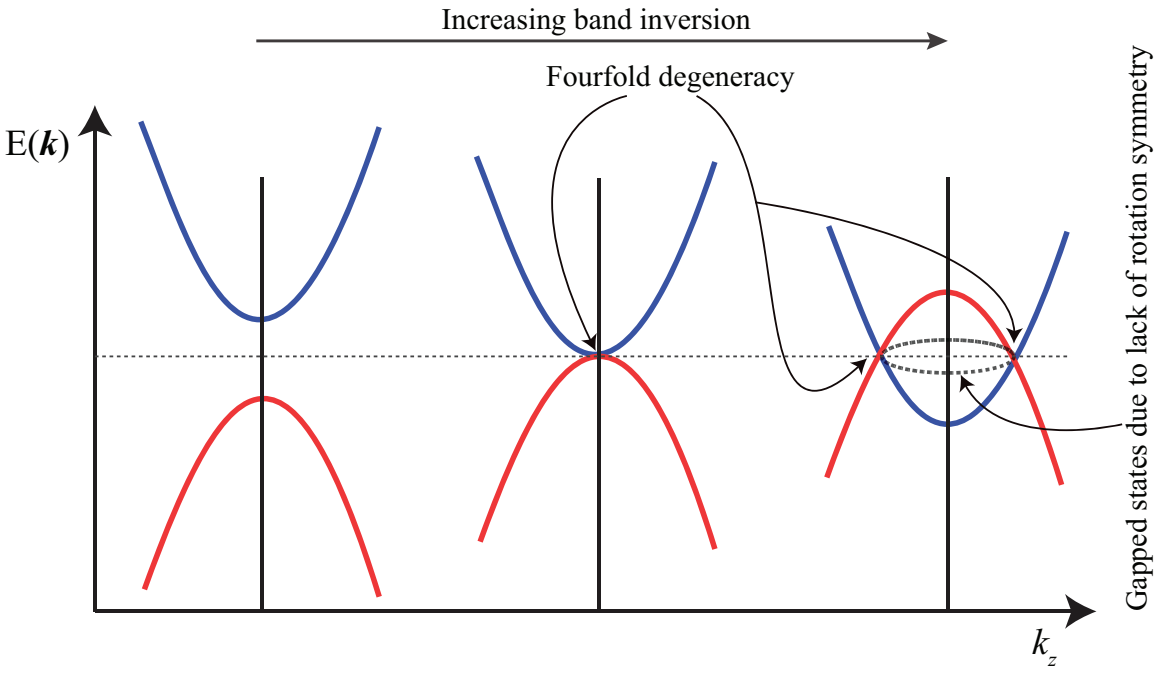

Figure 1.4: Schematic illustration of Dirac points arising due to band inversion and stabilized by rotation symmetry. Schematic conduction and valence bands plotted as a function of k_z where k_z is an axis of rotation symmetry. Bands invert relative to each other as a parameter is tuned from left to right. The bands intersect on a surface in three dimensional momentum space, but hybridize except on points where the surface intersects the rotation axis k_z because both bands belong to orthogonal representations of the rotation group along k_z.

Dirac cones among the representations of a specific spacegroup. Once the symmetry criteria is established, we will discuss empirical design principles that could be applied to elements of the periodic table to engineer a material such that the Dirac cone appears at the Fermi energy and there are no additional non-Dirac-like states at the Fermi level. We note that this approach is somewhat distinct from the path taken to find topological insulators or topological Dirac semimetals where the 'rules of thumb' include looking for materials with heavy atoms (strong spin-orbit coupling) as well as the existence of orthogonal orbitals (s and p; p and d, or a combination thereof) in the vicinity of the Fermi energy. The presence of s and p orbitals near the Fermi level in a particular material increases the possibility of band inversions

in the presence of strong spin-orbit coupling. For example, in HgTe and in CdTe without spin-orbit coupling, valence orbitals nearest to the Fermi energy are p-like whereas the conduction orbitals nearest to the Fermi energy are s-like. As spin-orbit coupling is introduced, the s-singlet turns into as $s_{1/2}$-doublet, whereas the p-triplet splits into a $p_{3/2}$-quadruplet and a $p_{1/2}$-doublet. Ordinarily, one would expect the $s_{1/2}$ doublet to lie above the p-states in energy. This is exactly the case in CdTe. However, the stronger spin-orbit coupling in HgTe pushes the $s_{1/2}$-doublet below the $p_{3/2}$-quadruplet in energy resulting in an 'inversion' of the band order (Bernevig et al. (2006) and Fig. 5.5). This 'inversion' of the band ordering is necessary to realize both a topological insulator, and a topological Dirac semimetal (Fig. 1.4). Approaches to find such systems are driven by looking for materials that could realize such a band inversion.

The search for symmetry protected Dirac semimetals takes a different path as we show in the Chapters that follow. Prior discussion has also made mention of Weyl semimetals, which are another kind of three dimensional topological semimetals. In the following Section, we describe Weyl semimetals and distinguish them from Dirac semimetals.

1.2. Weyl Semimetals

Weyl semimetals derive their name from the similarity of their effective Hamiltonian at the Fermi level with the Weyl Hamiltonian of particle physics (Wan et al., 2011; Burkov and Balents, 2011). In three spatial dimensions, the massless Dirac Hamiltonian decouples into two copies of a Weyl Hamiltonian each carrying opposite charge. Such a two state Hamiltonian can also describe a point where two energy bands are degenerate and disperse linearly in all three directions to leading order in momentum.

The Weyl Hamiltonian describing such a twofold degeneracy at a point $\mathbf{k}_1$ in the BZ can be written as,

$$\mathcal{H}(\mathbf{k}) = (k_x - k_{1x})\sigma_x + (k_y - k_{1y})\sigma_y + (k_z - k_{1z})\sigma_z, \tag{1.1}$$

where σ_i are the usual Pauli matrices. Within the two-state space, any perturbation to this Hamiltonian will be proportional to a linear combination of the Pauli matrices. Such a perturbation, however large, only shifts the degeneracy away from $\mathbf{k}_1$ and can never gap the system. Hence, the Weyl Hamiltonian of Eq. (1.1) is protected against all perturbations. This fact can be quantified by assigning this particular Hamiltonian a topological number, or a charge. In this case, the topological number is the first Chern number of states on the Fermi surface (Fig. 1.5) of the Weyl Hamiltonian. The Chern number of a Weyl Hamiltonian can be calculated using,

$$n = \frac{1}{2\pi i}\int_{\partial S} d\mathbf{a}\cdot\nabla\times\langle\psi_{\mathcal{E}_F}(\mathbf{k})|\nabla|\psi_{\mathcal{E}_F}(\mathbf{k})\rangle \tag{1.2}$$

where the surface ∂S in $\mathbf{k}$-space is defined by solving $\mathcal{H}(\mathbf{k})\psi(\mathbf{k}) = \mathcal{E}_F\psi(\mathbf{k})$ for fixed $\mathcal{E}_F$. In a general basis, the Weyl Hamiltonian, $\mathcal{H}(\mathbf{k}) = \sum_{ij} v_{ij}k_i\sigma_j$, and the Chern number $n = \mathrm{sgn}(\det[v_{ij}])$. The Chern number of the Hamiltonian in Eq. (1.1) is $+1$.

In the presence of time reversal symmetry, every state at $\mathbf{k}$ has a Kramers partner at $-\mathbf{k}$. Therefore, a Weyl degeneracy located at a point $\mathbf{k}_1$, described by Eq. (1.1), has a counterpart at $-\mathbf{k}_1$. Under time reversal symmetry, the orientation of the surface integral in Eq. (1.2) changes sign. However, time reversal is anti-unitary, so the Chern number of the two Weyl points at $\mathbf{k}_1$ and $-\mathbf{k}_1$ is the same i.e. $+1$. On the other hand, the presence of time reversal symmetry mandates that the total Chern number of the Fermi surface should be zero. Hence, there must exist two more Weyl degeneracies

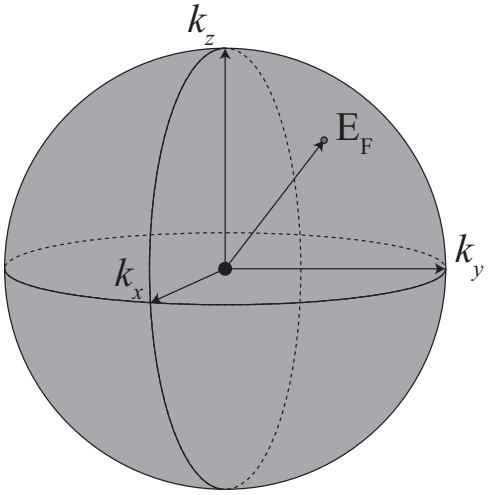

Figure 1.5: Fermi surface of an isotropic Weyl point centered at the origin. A nonzero Chern number implies the existence of a singularity (charge ± 1) within the surface.

at points $\mathbf{k}_2$ and $-\mathbf{k}_2$ with Chern number -1.

We conclude that a Weyl semimetal in the presence of time reversal symmetry exhibits at least four (or multiples of four) point-like twofold degeneracies at the Fermi surface and the energy bands disperse linearly in all three directions around the Weyl points (Halász and Balents, 2012). If inversion symmetry is present, the orientation of the surface integral in Eq. (1.2) changes sign so the Chern numbers at $\mathbf{k}_1$ and $-\mathbf{k}_1$ have opposite sign because inversion is unitary. Therefore, when both inversion and time reversal symmetry are present, $\mathbf{k}_1 = \mathbf{k}_2$, and instead of four distinct twofold point-like degeneracies, we have two distinct fourfold point-like degeneracies described by a massless Dirac equation unless $\mathbf{k}_1$ is time reversal symmetric in which case there will be only one fourfold point-like degeneracy. Such a system will be described by a massless Dirac Hamiltonian, and defines a Dirac semimetal. In summary, we note the following differences between Weyl and Dirac semimetals,

- Weyl semimetals exhibit twofold whereas Dirac semimetals exhibit fourfold point-like degeneracies on the Fermi surface.

- Unlike symmetry protected Dirac points, Weyl points either come in a pair of two (if inversion symmetry is present) or two pairs of two (if time reversal symmetry is present).

- Weyl points are topologically protected (nonzero Chern number) whereas Dirac points are not protected (zero Chern number). However, the existence of a nonzero topological number in the bulk signals the presence of surface states due to the bulk boundary correspondence. Therefore, Weyl semimetals exhibit topologically protected Fermi arcs on the two dimensional boundary of a system (Wan et al., 2011; Burkov and Balents, 2011), whereas Dirac semimetals do not exhibit any topologically protected surface states. Topological Dirac semimetals, described above, exhibit Fermi arcs because they are perturbatively connected to topological insulators (Wang et al., 2012, 2013).

The central question addressed in this dissertation is whether there exists a symmetry that might protect a Dirac point because, as discussed above, a Dirac point is a combination of two Weyl points with opposite Chern number and is not protected topologically. Note that it is also possible for Weyl points of the same Chern number to be degenerate. In such a situation, the degeneracy can be stabilized by a point group symmetry, as we will show explicitly for threefold rotation symmetry in Section 2.3. Such semimetals are topological in nature and have been termed 'Multi-Weyl' topological semimetals (Fang et al., 2012).

Chapter 2

Symmetry protected Dirac points in three dimensions

A Dirac point occurs when four energy bands are degenerate at a point $\mathbf{k}_0$ such that each band disperses linearly to lowest order in $\mathbf{k}$ about $\mathbf{k}_0$ (Young et al., 2012). In such a case, the low energy effective Hamiltonian can be written as a four band Dirac Hamiltonian $\mathcal{H}(\mathbf{k}) = \sum_i v_i(k_i - k_{0,i})\gamma_i$ centered at $\mathbf{k}_0$ where $\{\gamma_j\}$ are 4×4 Hermitian matrices and v_i are Fermi velocities. The central question underlying the existence of a Dirac Hamiltonian at $\mathbf{k}_0$ is whether $v_i \neq 0$ for all i. The space of 4×4 Hermitian matrices is spanned by a basis of 16 Hermitian matrices that consist of the identity matrix, 5 Dirac matrices Γ^a, and their 10 commutators $\Gamma^{ab} = [\Gamma^a, \Gamma^b]/2i$. We choose a basis such that $\Gamma^{(1,2,3,4,5)} = \{\tau_x \otimes I, \tau_z \otimes I, \tau_y \otimes \sigma_x, \tau_y \otimes \sigma_y, \tau_y \otimes \sigma_z\}$, where $\{\tau_i\}$ and $\{\sigma_j\}$ are the usual 2×2 Pauli matrices. If $\{\sigma_i\}$ denotes the spin degree of freedom, the time reversal operator can be chosen to be $\Theta = i\sigma_y \mathrm{K}$ where K denotes complex conjugation. It follows that the Dirac matrices Γ^a are even under time reversal symmetry whereas their commutators Γ^{ab} are odd. Therefore if $\mathbf{k}_0$ is time reversal symmetric ($\mathbf{k}_0 \equiv -\mathbf{k}_0$ up to reciprocal lattice translations), the matrices γ_i must be linear combinations of the 10 commutators Γ^{ab}. This is an example of a symmetry constraining the space of possible 4×4 Hermitian matrices in a Dirac-like Hamiltonian.

Other symmetries can further constrain which Dirac matrices might appear in the Hamiltonian. Suppose there exists a Dirac point at $\mathbf{k}_0$ described by a Hamiltonian of

the form,

$$\mathcal{H}(\mathbf{k}) = v_x(k_x - k_{0,x})\gamma_x + v_y(k_y - k_{0,y})\gamma_y + v_z(k_z - k_{0,z})\gamma_z \tag{2.1}$$

where γ_i are chosen from the set $\{\Gamma^a, \Gamma^{ab}\}$. In principle, the Dirac point at $\mathbf{k}_0$ can be gapped by a mass term proportional to one of the matrices in the set $\{\Gamma^a, \Gamma^{ab}\}$ unless that matrix violates a symmetry at $\mathbf{k}_0$. Therefore, if it can be shown that all possible mass terms break at least one symmetry at $\mathbf{k}_0$, the Dirac point is protected under all symmetry preserving perturbations. Thus one can identify the symmetry groups which allow Dirac points to exist. This method is tedious because, as we show later, it requires complete knowledge of regular and projective four dimensional irreducible representations of spacegroup elements. Regular representations of spacegroups can be calculated by choosing representative operators of those elements of a four dimensional irreducible representation of $SU(2)$ that belong to the 32 point groups. Projective representations of $SU(2)$ require knowledge of a factor system that governs multiplication rules between all the unitary operators in the representation. In the theory of spacegroups, the factor system arises from knowledge of translations within a unit cell. But the existence of a unit cell and consequent spatial periodicity restricts $SU(2)$, or rather accurately $SO(3)$, to a set of finite subgroups (the 32 point groups). Since we are concerned with spacegroups, direct calculation of the finitely many projective representations (with all possible factor systems) of the 32 point groups appears to this author a simpler task than calculating possibly infinitely many projective representations of $SU(2)$.

Fortunately, this has been done by many authors during the last century (Bradley and Cracknell (1976) and references therein). Our task is to understand the underlying theory well enough to be able to use their results to meet our goals. Therefore, we look

for four dimensional irreducible representations (FDIRs) among the double-valued representations of all the 230 spacegroups and then apply certain group theoretic criteria to classify a subset of the FDIRs which allow linear dispersion in all directions and carry zero total Chern number. This method is equivalent to the more direct path outlined earlier.

This Chapter is organized as follows. In Section 2.1, we describe the relationship between the Chern number of a FDIR and rotational symmetries within the symmetry group at the Dirac point. We develop a simple test based on rotation eigenvalues of states along a rotation axis to predict whether a certain FDIR will carry nonzero total Chern number. This we call the 'Chern number test'. In Section 2.2 we introduce the representation theory of spacegroups and prove that symmetry protected Dirac points can only arise as projective representations of point groups on the face of the Brillouin zone. In Section 2.3 we show explicitly that the cubic point groups do not allow three dimensional Dirac points in their representations. The remaining point groups do not have enough symmetry to exhibit FDIRs among their regular representations, although the non-cubic point groups exhibit FDIRs among their projective representations. In Section 2.4 we show that the Kronecker product of a FDIR with the vector representation of the symmetry group can be used to ensure that the FDIR splits linearly in all directions. This completes all steps necessary to identify symmetry protected Dirac points in the 230 spacegroups.

2.1. Chern number and Dirac points

A Dirac point is guaranteed to have zero total Chern number if it is known to be a combination of two Weyl points with opposite Chern numbers, but a given FDIR is not, a priori, known to have such a characteristic. However, the Chern number of a

FDIR at a time reversal symmetric momentum can be calculated up to an integer if the momentum in question lies on a rotation symmetry axis. This relationship between Chern numbers and rotation eigenvalues can be used to test whether FDIRs at time reversal symmetric momenta have nonzero total Chern number. Most FDIRs occur on time reversal symmetric momenta, so the Chern number test applies. We find that whenever the symmetry group at a time reversal symmetric momentum contains threefold rotation symmetry, any FDIR at that point cannot have zero Chern number. For FDIRs at non-time reversal symmetric momenta, the Chern number needs to be calculated explicitly.

The total Chern number of the Fermi surface in systems with time reversal symmetry must be zero. Therefore, if a Dirac point carries nonzero Chern number (a multi-Weyl point), there must exist additional Fermi surface to cancel the excess Chern number. Such Fermi surface might obscure the physics due to the Dirac point, although the extent to which that might happen is a question yet to be addressed. We are going to require that candidate FDIRs for Dirac points should have zero total Chern number.

Given a time reversal symmetric $\mathbf{k}_0$, the Chern number of a linearly dispersing FDIR (if one exists) at $\mathbf{k}_0$ can be determined using the rotation eigenvalues of states on a rotation symmetry axis that goes through $\mathbf{k}_0$. We label such a rotation symmetry axis as $\hat{\mathbf{k}}$. The four degenerate states that span the FDIR at $\mathbf{k}_0$ can be represented as a $p_{3/2}$ quadruplet. The states $|\psi(\mathbf{k}_0 + \alpha\hat{\mathbf{k}})\rangle$ are eigenvectors of the rotation operator, where α is a real parameter. For a $2\pi/\mathrm{n}$ rotation symmetry, their eigenvalues will be $e^{i2\pi j/n}$ where $j = \{\pm 3/2, \pm 1/2\}$. On a crystal lattice where $n = \{2, 3, 4, 6\}$ the set of possible rotation eigenvalues is finite, as shown in Table 2.1.

Since $\mathbf{k}_0$ is invariant under time reversal symmetry, rotation eigenvalues of states $|\psi(\mathbf{k}_0+\alpha\hat{\mathbf{k}})\rangle$ and $|\psi(\mathbf{k}_0-\alpha\hat{\mathbf{k}})\rangle$ that lie on the same energy level are complex conjugates.

	n	2	3	4	6
j	$\exp^{2\pi ij/n}$	$\exp^{\pi ij}$	$\exp^{2\pi ij/3}$	$\exp^{\pi ij/2}$	$\exp^{\pi ij/6}$
1/2	$\exp^{\pi i/n}$	i	$\exp^{i\pi/3}$	$\exp^{i\pi/4}$	$\exp^{i\pi/6}$
3/2	$\exp^{3\pi i/n}$	$-i$	-1	$\exp^{i3\pi/4}$	i

Table 2.1: Rotation eigenvalues of a $p_{3/2}$ quadruplet for crystallographic rotation symmetries.

Time reversed states for half integer spin are orthogonal to each other and cannot be related by a phase. In a three dimensional metal, states at the same energy lie on a closed surface in momentum space. If states on the North and South poles of a constant energy surface (defined by points where the rotation symmetry axis intersects the surface) are Kramers partners, it is not possible to relate them by a phase that varies continuously over the surface. In other words, there exists a Kramers degeneracy at the time reversal symmetric momentum $\mathbf{k}_0$. The existence of this degeneracy implies that the constant energy surface must have a nonzero Chern number. We defined the Chern number in Eq. 1.2 as,

$$n_{\mathbf{k}_0} = \frac{1}{2\pi i} \sum \int_{\partial S} d^2k \ \hat{\mathbf{n}}_{\mathbf{k}} . \nabla_{\mathbf{k}} \times \langle \psi_i(\mathbf{k}) | \nabla_{\mathbf{k}} | \psi_i(\mathbf{k}) \rangle \tag{2.2}$$

where ∂S is a closed surface enclosing the point $\mathbf{k}_0$ in momentum space defined by $\mathcal{H}(\mathbf{k})\psi(\mathbf{k}) = \mathcal{E}_F \psi(\mathbf{k})$ for fixed $\mathcal{E}_F$, $\hat{\mathbf{n}}_{\mathbf{k}}$ is the unit normal pointing out of the surface, and the sum runs over all states $\psi(\mathbf{k})$ on the surface ∂S with energy $\mathcal{E}_F$.

In a two band framework, the Chern number of a surface that bisects an n-fold rotation axis is given by $(p - q) \mod n$ where $\exp^{i2\pi p/n}$ and $\exp^{i2\pi q/n}$ are rotation eigenvalues of states on the North and the South pole. If these are related by time reversal symmetry, $q = -p$, and the Chern number is $2p \mod n$. In a $p_{3/2}$ quadruplet, we have two pairs of Kramers partners on the North and South poles. Therefore, the total Chern number will be $2p + 2p' \mod n$ where p and p' can be identical or distinct

from the set $\{\pm 3/2, \pm 1/2\}$.

Figure 2.1 describes all the possibilities for p and p'. If $n = 3, 6$ the fourfold degeneracy can split into four single bands [Figs. 2.1(a) and (b)] only, and the Chern number is $2 \mod n$ where $n = 3, 6$. It is not possible for the fourfold degeneracy to split into twofold degenerate bands with nonzero linear dispersion whenever threefold or sixfold rotation symmetry are present. It is possible for the fourfold degeneracy to split into a twofold degenerate band and a pair of nondegenerate bands [Fig. 2.3(c)] in which case the Chern number will be $0 \mod n$ for $n = 3, 6$ but the twofold degenerate band disperses quadratically as in zincblende (Section 5.1). The dispersion shown in Figure 2.3(c) does not constitute a Dirac semimetal.

For twofold and fourfold rotation symmetries, the fourfold degeneracy can split into either singlets or doublets [Figs. 2.1(c) and (d)] and in either case the Chern number is $0 \mod n$ for $n = 2, 4$. Therefore, we can draw the following conclusions:

- In the presence of a threefold or sixfold rotation symmetry, the Dirac point splits into four nondegenerate bands and carries nonzero Chern number.
- In the presence of twofold or fourfold rotation symmetry, the Dirac point splits either into four nondegenerate bands or twofold degenerate bands and carries zero Chern number.

Therefore, all time reversal symmetric momenta lying on a threefold or sixfold symmetry axis cannot host a Dirac point. The vast majority of BZ momenta which host FDIRs are time reversal symmetric so the Chern number test is sufficient (see Section 3.1). For non-time reversal symmetric momenta, the Chern number can be calculated explicitly by choosing an appropriate Dirac Hamiltonian. Section 2.3 shows how a Dirac Hamiltonian can be constructed given the little group at a specific BZ

momentum.

2.2. Irreducible representations of double spacegroups

We are interested in finding BZ momenta which host four dimensional irreducible representations (FDIRs). The representation theory of spacegroups has been studied extensively by many authors (Bradley and Cracknell (1976) and references therein). Relevant facts such as little groups of each BZ momentum and their character tables along with the identification of single and double valued representations that can occur with and without time reversal symmetry have been collected (Bradley and Cracknell, 1976). Since we will make use of these ideas extensively, we devote this Section to exploring how four dimensional representations arise at time reversal symmetric momenta without a threefold symmetry. We begin with a description of the representation theory of spacegroups. Our main conclusion is that symmetry protected Dirac points can only exist in nonsymmorphic spacegroups and that on the surface of the BZ. This does not rule out cases where Dirac points arise on rotation symmetry axes inside the BZ due to band inversion (Wang et al., 2012, 2013).

The translational symmetry of a crystal lattice implies that we can index the representations of a spacegroup G by a momentum $\mathbf{k}$ confined to the BZ. Therefore at a momentum $\mathbf{k}$, the Bloch states $|\psi(\mathbf{k})\rangle$ span irreducible representations of the little group $G_{\mathbf{k}}$ which consists of operations in G that preserve $\mathbf{k}$. Since G is a spacegroup, it consists of operations which can be denoted by $\{R|\mathbf{t}\}$ where R implements a rotation and $\mathbf{t}$ implements a translation of the lattice. The action of G on Bloch states can be represented as, $\{R|\mathbf{t}\}\psi(\mathbf{k},\mathbf{x}) = \psi(R\mathbf{k},\mathbf{x}-\mathbf{t})$. $R\mathbf{k}$ and $\mathbf{k}$ are equivalent if $R\mathbf{k}-\mathbf{k}$ equals a reciprocal lattice vector; we can then write $\{R|\mathbf{t}\}\psi(\mathbf{k},\mathbf{x}) = \exp^{-i\mathbf{k}\cdot\mathbf{t}}\psi(\mathbf{k},\mathbf{x})$. Therefore $\psi(\mathbf{k},\mathbf{x})$ is an eigenstate of $\{R|\mathbf{t}\}$, and consequently $\{R|\mathbf{t}\}$ is a member of

the little group $G_{\mathbf{k}}$.

There are two kinds of spacegroups: symmorphic and nonsymmorphic. Symmorphic spacegroups consist of point group rotations coupled with Bravais lattice translations. Therefore every element $\{R|\mathbf{t}\}$ in a symmorphic spacegroup can be written as $\{R|\mathbf{t}\} = \{E|\mathbf{t}\}\{R|\mathbf{0}\}$ under the multiplication rule of spacegroup operators,

$$\{R_1|\mathbf{t}_1\}\{R_2|\mathbf{t}_2\} = \{R_1R_2|R_1\mathbf{t}_2 + \mathbf{t}_1\}, \tag{2.3}$$

where E is the identity element. Note that $\{E|\mathbf{t}\}\{R|\mathbf{0}\} \neq \{R|\mathbf{0}\}\{E|\mathbf{t}\}$. Therefore symmorphic spacegroups can be written as a semidirect product of a point group with a translation group. There are 14 distinct Bravais lattices, each exhibiting specific point group symmetry. All appropriate semidirect group combinations of the 32 point groups with the 14 Bravais lattices yield 73 symmorphic spacegroups.

Nonsymmorphic spacegroups cannot be written as semidirect products of a point group with a translation group. They contain spacegroup operators wherein rotations are coupled with nonprimitive lattice translations like a screw axis or a glide plane. The nonprimitive translations accompanying a specific point group operation depend on a choice of coordinates. However, no choice of coordinates exists that will render *all* point group operations independent of nonprimitive translations. A well known example of a nonsymmorphic spacegroup in three dimensions is diamond. The diamond lattice consists of two identical interpenetrating FCC lattices separated by the vector $1/4(1,1,1)$ from each other. Inversion (I) of coordinates about a point on one sublattice translates the origin of the other sublattice by a vector -1/2(1,1,1) so the entire lattice must then be translated back by 1/4(1,1,1) to realize the initial configuration. This spacegroup operation can be written as $\{I|1/4(1,1,1)\}$ and since

the accompanying translation vector is nonprimitive, the two individual operations, inversion and translation by $1/4(1,1,1)$, cannot be decoupled from each other. It is possible to redefine the coordinate system so that the exchange of sublattices in diamond is accomplished by inverting about a bond center at $1/8(1,1,1)$. In this case, inversion becomes a symmorphic operation, however certain other rotation and mirror symmetries are rendered nonsymmorphic. There does not exist a choice of coordinates for which all the point group operations in diamond can be written as purely symmorphic operations. This is a defining characteristic of nonsymmorphic spacegroups of which there are 157 in total.

Representations of a symmorphic spacegroup follow from those of the corresponding point group. Recall that for a symmorphic operation,

$$\{R|\mathbf{t}\}\psi(\mathbf{k},\mathbf{x}) = \{E|\mathbf{t}\}\{R|0\}\psi(\mathbf{k},\mathbf{x}) = e^{-iR\mathbf{k}\cdot\mathbf{t}}\psi(R\mathbf{k},\mathbf{x}).$$

We can draw two conclusions from this: first, representations of symmorphic spacegroups are obtained by multiplying representations of the Bravais lattice and the corresponding point group; second, representations of the Bravais lattice group are all one dimensional. Therefore higher dimensional representations of a symmorphic spacegroup follow directly from those of the 32 point groups.

Among the 32 point groups, only the 5 cubic groups exhibit double-valued FDIRs. However all cubic groups contain threefold rotation symmetry. It turns out that cubic symmetry only appears at time reversal symmetric momenta in three dimensions. Therefore even if there is a Dirac point at one of those momenta, it will have nonzero Chern number due to the threefold symmetry as shown in Section 2.1. FDIRs in symmorphic spacegroups always arise as a result of cubic symmetry at time rever-

sal symmetric momenta. Therefore, we can conclude that symmorphic spacegroups cannot host Dirac points.

Nonsymmorphic spacegroups exhibit FDIRs at points $\mathbf{k}$ even if the little group $\mathrm{G}_{\mathbf{k}}$ does not contain threefold rotations. Recall that in a nonsymmorphic spacegroup, $\mathrm{G}_{\mathbf{k}}$ cannot be written as a semidirect product of a point group with a translation group at some points in the BZ. In other words, we cannot decouple the action of nonsymmorphic operators on state vectors into a rotation and a translation. Suppose the unitary matrices $\mathcal{U}_{\mathbf{k}}(R)$ represent the action of the nonsymmorphic operator $\{R|\mathbf{t}\}$ on state vectors $|\psi(\mathbf{k})\rangle$ so that $\{R|\mathbf{t}\}\psi(\mathbf{k},\mathbf{x}) = e^{-i\mathbf{k}\cdot\mathbf{t}}\mathcal{U}_{\mathbf{k}}(R)\psi(\mathbf{k},\mathbf{x})$. Then the multiplication rule (Eq. 2.3) in terms of the matrices $\mathcal{U}_{\mathbf{k}}$ can be written as,

$$\begin{aligned} e^{-i\mathbf{k}\cdot\mathbf{t}_2}\mathcal{U}_{\mathbf{k}}(R_1)\mathcal{U}_{\mathbf{k}}(R_2) &= e^{-i\mathbf{k}\cdot R_1\mathbf{t}_2}\mathcal{U}_{\mathbf{k}}(R_1R_2) \\ \mathcal{U}_{\mathbf{k}}(R_1)\mathcal{U}_{\mathbf{k}}(R_2) &= e^{-i(R_1^{-1}\mathbf{k}-\mathbf{k})\cdot\mathbf{t}_2}\mathcal{U}_{\mathbf{k}}(R_1R_2). \end{aligned} \tag{2.4}$$

The phase appearing in Eq. (2.4) is 1 unless $\mathbf{t}_2$ is nonprimitive and $R_1^{-1}\mathbf{k}-\mathbf{k}$ is a nonzero reciprocal lattice vector. $\mathbf{t}_2$ is nonprimitive (fraction of a lattice translation) in some elements in nonsymmorphic spacegroups, whereas $R_1^{-1}\mathbf{k} = \mathbf{g}_i + \mathbf{k}$, where $\mathbf{g}_i$ is a reciprocal lattice translation, holds for momenta only on the *surface* of the Brillouin zone. Eq. (2.4) shows that the matrices $\mathcal{U}_{\mathbf{k}}$ form a representation of the operators $\{R_i\}$ which corresponds to the rotation counterparts of the elements of the little group $\mathrm{G}_{\mathbf{k}}$. In fact the set of point group operators $\{R_i\}$ is always isomorphic to one of the 32 point groups. This holds for both symmorphic and nonsymmorphic little groups. If, however, the phases in Eq. (2.4) are nonzero, the representation $\mathcal{U}_{\mathbf{k}}$ is a *projective* representation of a point group with the factor system given by $e^{-i(R_1^{-1}\mathbf{k}-\mathbf{k})\cdot\mathbf{t}_2}$ where $\mathbf{t}_2$ uniquely identifies R_2 by association in the spacegroup element $\{R_2|\mathbf{t}_2\}$, and R_1 appears in the factor system explicitly.

A projective representation Γ with factor system μ of a group is defined such that $\Gamma(g_1)\Gamma(g_2) = \mu(g_1, g_2)\Gamma(g_1 g_2)$, where $\{g_i\}$ are elements of the group. If $\mu(g_i, g_j) = 1$ for all i, j, the representation Γ is one of the ordinary representations of the group. Projective representations generalize the concept of group representation and include among them all the ordinary representations of a group. A theorem by Schur provides a prescription to determine projective representations. It stipulates that all projective representations can be obtained from regular representations of a larger group called the central extension group obtained by multiplying the original group with an appropriate Abelian group. Therefore the problem of finding projective representations reduces to finding regular representations of the central extension group and restricting the representative matrices of the larger group to the elements that correspond directly to the elements of the original group. Finite groups have only a finite set of possible factor systems. Thus, one can obtain all projective representations of a finite group by choosing an appropriate central extension group corresponding to the finitely many possible factor systems.

Finding the central extension group of a double point group is necessary to identify irreducible representations of nonsymmorphic spacegroups. Fortunately this has been done by prior authors in rigorous detail, as noted earlier, so we will be relying exclusively on their results (Bradley and Cracknell, 1976). The extent of our efforts only goes as far as understanding their theory and interpreting their results without error (Chapters 3 and 4).

We have noted earlier that only the 5 cubic double groups exhibit four dimensional representations among their ordinary representations. When we examine projective representations of the 32 point groups, we find that some of the non cubic groups exhibit four or higher dimensional representations. These representations will be the

key ingredient in realizing Dirac points in three dimensional crystals.

2.3. Hamiltonian construction for symmorphic spacegroups

In this Section we provide, with explicit examples, a method to determine the Dirac Hamiltonian given a four dimensional irreducible representation of a point group. Calculations shown in this Section have been repeated in Sections 4.1, 4.2, and 5.2.1 for spacegroups 227 (diamond), 74 (distorted spinels), and 216 (zincblende) respectively. In three dimensions, there are 32 distinct point groups. For reference, we will use Bradley and Cracknell (1976) for character tables and representative operators in each irreducible representation. We show how to derive an effective Hamiltonian given group representative operators if it is supposed that energy and momentum are linearly related around a point of degeneracy. Among double valued regular representations, the cubic group with inversion symmetry O_h, the cubic group O, and the tetrahedral group with mirror planes T_d have four dimensional irreducible representations. All the remaining 29 point groups have at most two dimensional irreducible representations. We note that the procedure described in this Section can only be used to construct *regular* representations of point groups, and only works for symmorphic spacegroups. For nonsymmorphic spacegroups, we use representative operators from Bradley and Cracknell (1976).

The groups O and T_d are subgroups of the cubic group with inversion symmetry, O_h. We begin our discussion by calculating the effective Hamiltonian in the vicinity of a fourfold degeneracy at a point $\mathbf{k}_0$ assuming that the little group $G_{\mathbf{k}_0}$ is O_h. This situation arises, for example, at $\Gamma(\mathbf{k}_0 = \mathbf{0})$ in spacegroups 221-230. Furthermore, we assume that the point $\mathbf{k}_0$ is symmetric under time reversal. This assumption is not too restrictive because a significant number of four dimensional irreducible

representations occur at time reversal symmetric momenta.

In a four band framework, we can express the Hamiltonian in terms of sixteen independent Hermitian operators $\Gamma_{\mu\nu} = \tau_\mu \otimes \sigma_\nu \equiv \tau_\mu \sigma_\nu$[1] where $\tau_\mu = \{\mathbf{I}, \tau_1, \tau_2, \tau_3\}$ and $\sigma_\nu = \{\mathbf{I}, \sigma_1, \sigma_2, \sigma_3\}$. σ_i and τ_i are the usual 2×2 Pauli matrices. We choose basis such that the time reversal operator $\Theta = i\Gamma_{02}\mathrm{K} = i\sigma_2\mathrm{K}$, where K denotes complex conjugation. Without loss of any generality, we assume a massless Dirac Hamiltonian centered at $\mathbf{k}_0$,

$$\mathcal{H}(\mathbf{k}) = \sum_{i=x,y,z} \alpha_i k_i \gamma_i \tag{2.5}$$

where $\gamma_i^2 = \mathbf{I}$ and the matrices γ_i are linear combinations of the Dirac matrices $\Gamma_{\mu\nu}$. Time reversal symmetry requires $\mathcal{H}(-\mathbf{k}) = \sum_{i=x,y,z} \alpha_i k_i \Theta \gamma_i \Theta^\dagger$ which restricts the matrices γ_i to be linear combinations of the following set,

$$\{\sigma_1, \sigma_2, \sigma_3, \tau_1\sigma_1, \tau_1\sigma_2, \tau_1\sigma_3, \tau_2, \tau_3\sigma_1, \tau_3\sigma_2, \tau_3\sigma_3\}$$

The group O_h can be generated by multiplying elements of the cubic group O with the inversion operation I. The cubic group O consists of the following symmetry operations and their products: fourfold rotations about the three principal axes of a cube; threefold rotations about four independent diagonal axes connecting the four corners of a cube; and twofold rotations about the six independent axes bisecting opposite edges. Figure 2.2 illustrates our choice of orientation and labeling of symmetry axes. The cubic group for particles with half integer spin is isomorphic to an abstract group with 48 elements (Bradley and Cracknell, 1976). It can be generated by the following set of operations: C_{4z}^+, fourfold anticlockwise rotation about $\hat{z}$;

[1] We omit the tensor product sign $\otimes$ and the identity matrix $\mathbf{I}$ for brevity. Therefore, $\tau_\mu \equiv \tau_\mu \otimes \mathbf{I}$ and $\sigma_\mu \equiv \mathbf{I} \otimes \sigma_\mu$.

$\bar{C}_{4x}^{+}$, fourfold anticlockwise rotation about $\hat{x}$; and C_{31}^{+}, threefold anticlockwise rotation about an axis parallel to $1/\sqrt{3}(\hat{x}+\hat{y}+\hat{z})$. The bar on $\bar{C}_{4x}^{+}$ implies that its character $\chi(\bar{C}_{4x}^{+}) = -\chi(C_{4x}^{+})$, although both $\bar{C}_{4x}^{+}$ and C_{4x}^{+} act identically on real space vectors such as $\mathbf{k}$. The necessity of two distinct operators to implement fourfold rotations, for example, is clear if we recall that $SU(2)$ is a double covering of the rotation group $SO(3)$. Two distinct elements in $SU(2)$ with characters having opposite signs will map to one unique element in $SO(3)$.

In $SU(2)$, any rotation by an angle θ about an axis $\hat{n}$ can be represented by $R_{\hat{n}}(\theta) = \exp(i\vec{J}\cdot\hat{n}\theta)$ where the generators $\vec{J}$ satisfy the angular momentum commutation relations, $[J_i, J_j] = i\epsilon_{ijk}J_k$ and $\vec{J}\cdot\vec{J} = J(J+1)$. In a two band system, $J = 1/2$ whereas in a four band system $J = 3/2$. Additionally, all elements of $SU(2)$ commute with the time reversal operator, $\Theta = i\sigma_2\mathrm{K}$, which implies the constraint $\{\Theta, J_i\} = 0$ for $i = x, y, z$. This is true for the Pauli matrices which is why they can be used to represent J_i and to generate the two dimensional irreducible representation of $SU(2)$. In a four band system, we choose a convenient basis for the operators $\vec{J}$ as follows,

$$J_x = \begin{pmatrix} 0 & 0 & 0 & \frac{\sqrt{3}}{2} \\ 0 & 0 & \frac{\sqrt{3}}{2} & 0 \\ 0 & \frac{\sqrt{3}}{2} & 0 & 1 \\ \frac{\sqrt{3}}{2} & 0 & 1 & 0 \end{pmatrix}, \quad J_y = \begin{pmatrix} 0 & 0 & 0 & \frac{-i\sqrt{3}}{2} \\ 0 & 0 & \frac{i\sqrt{3}}{2} & 0 \\ 0 & \frac{-i\sqrt{3}}{2} & 0 & i \\ \frac{i\sqrt{3}}{2} & 0 & -i & 0 \end{pmatrix},$$

$$J_z = \begin{pmatrix} \frac{3}{2} & 0 & 0 & 0 \\ 0 & -\frac{3}{2} & 0 & 0 \\ 0 & 0 & -\frac{1}{2} & 0 \\ 0 & 0 & 0 & \frac{1}{2} \end{pmatrix}. \tag{2.6}$$

These operators generate rotations about any axis $\hat{n}$ using $\exp(i\vec{J}\cdot\hat{n}\theta)$. Next, we

consider inversion symmetry. If inversion commutes with rotations, as it does for all symmorphic spacegroups in three dimensions, any operator representing inversion should commute with representations of $SU(2)$. However, according to Schur's lemma, any nonzero unitary operator that commutes with all the elements of a finite dimensional irreducible representation must be proportional to the identity matrix. Therefore, if we add the operation of inversion to any irreducible representation of $SU(2)$, the corresponding unitary operator will be $-\mathbf{I}$ where $\mathbf{I}$ is the identity matrix. In a four dimensional representation, inversion will take the form $-\Gamma_{00}$. Schur's lemma does not apply for time reversal symmetry because it is antiunitary, hence although time reversal commutes with $SU(2)$, it is not proportional to the identity matrix.

Consider the effect of inversion on a 4×4 massless Dirac Hamiltonian. Under inversion $\mathcal{H}(-\mathbf{k}) = \sum_{i=x,y,z} \alpha_i k_i I \gamma_i I^\dagger \neq -\sum_{i=x,y,z} \alpha_i k_i \gamma_i$ if I commutes with γ_i. Therefore, inversion symmetry restricts the Hamiltonian to be even in $\mathbf{k}$ in all directions. We conclude that Dirac Hamiltonians are not allowed at momenta which are symmetric under groups with inversion symmetry, such as O_h. The exception to this rule occurs in nonsymmorphic spacegroups where inversion symmetry, if present, does not commute with point group operations because of accompanying nonprimitive lattice translations. For example, in the diamond lattice inversion symmetry not only changes the sign of coordinates but also exchanges the sublattices. The sublattice exchange operation does not commute with all rotations, so the operator that implements inversion symmetry is not required to commute with irreducible representations of $SU(2)$. As we show later, a Dirac Hamiltonian is allowed in the diamond lattice despite the presence of inversion symmetry because the diamond lattice is nonsymmorphic.

Subgroups of O_h without inversion symmetry, such as the cubic group O, and the tetrahedral group with mirror planes T_d carry four dimensional irreducible representations among their regular representations. We consider the cubic group O first. As mentioned earlier, the generators of the cubic group are, $C_{4z}^{+} = \exp(iJ_z 2\pi/4)$, $\bar{C}_{4x}^{+} = -\exp(iJ_x 2\pi/4)$, and $C_{31}^{+} = \exp(i(J_x + J_y + J_z)2\pi/(3\sqrt{3}))$. The first two generators yield sufficient enough constraints to uniquely identify the matrices γ_i as shown below.

$$\mathcal{H}(k_y, -k_x, k_z) = \sum_{i=x,y,z} \alpha_i k_i C_{4z}^{+} \gamma_i C_{4z}^{+\dagger} = \alpha_x k_y \gamma_x - \alpha_y k_x \gamma_y + \alpha_z k_z \gamma_z \tag{2.7}$$

$$\mathcal{H}(k_x, k_z, -k_y) = \sum_{i=x,y,z} \alpha_i k_i \bar{C}_{4x}^{+} \gamma_i \bar{C}_{4x}^{+\dagger} = \alpha_x k_x \gamma_x + \alpha_y k_z \gamma_y - \alpha_z k_y \gamma_z \tag{2.8}$$

$$\mathcal{H}(k_y, k_z, k_x) = \sum_{i=x,y,z} \alpha_i k_i \bar{C}_{31}^{+} \gamma_i \bar{C}_{31}^{+\dagger} = \alpha_x k_y \gamma_x + \alpha_y k_z \gamma_y + \alpha_z k_x \gamma_z \tag{2.9}$$

The above equations lead to a number of constraints. $[C_{4z}^{+}, \gamma_z] = 0$ implies that γ_z can be chosen from the set $\{\sigma_3, \tau_3\sigma_3\}$. $[\bar{C}_{4x}^{+}, \gamma_x] = 0$ restricts γ_x to be σ_1, while the condition $\alpha_x\gamma_x = \alpha_y C_{4z}^{+}\gamma_y C_{4z}^{+\dagger}$ leads to $\gamma_y = -\sigma_2$ and $\alpha_x = \alpha_y$. Finally the condition $\alpha_y\gamma_y = \alpha_z \bar{C}_{4x}^{+}\gamma_z \bar{C}_{4x}^{+\dagger}$ implies $\gamma_z = \sigma_3$ and $\alpha_y = \alpha_z$. One can easily check that these four γ_i also satisfy the constraints due to the threefold symmetry operator C_{31}^{+}. Therefore, the Hamiltonian is uniquely identified to be,

$$\mathcal{H}(\mathbf{k}) = \alpha_z \mathbf{I} \otimes (k_x\sigma_1 - k_y\sigma_2 + k_z\sigma_3)\,. \tag{2.10}$$

This Hamiltonian consists of two copies of the Weyl Hamiltonian each with a charge -1. Thus it describes a 'Multi-Weyl' topological semimetal first discussed in Fang et al. (2012). The sign of the Weyl charge depends on our choice of orientation but the Weyl charge being nonzero is a direct consequence of the presence of threefold

symmetry in the cubic group. In Section 2.1 we showed using the Chern number test that the presence of threefold symmetry at a time reversal symmetric momentum constrains the Dirac Hamiltonian to have a nonzero Weyl charge. The above calculations can also be extended to the case when time reversal is not a symmetry at the Dirac point $\mathbf{k}_0$. In that case, the matrices γ_i can be chosen from all sixteen Dirac matrices $\Gamma_{\mu\nu}$.

Next, we consider the tetrahedral group with mirror planes T_d. This group is a subgroup of O_h with generators $S^-_{4z} = IC^+_{4z}$, C^+_{31}, and $\bar{S}^-_{4x} = I\bar{C}^+_{4x}$. We use the symbol S to denote 'rotation reflections', which are products of a rotation operator with inversion. Mirror symmetry is a special kind of rotation reflection because it is a product of twofold rotations with inversion. In the point group T_d, neither inversion I nor fourfold rotations C_{4i} exist individually, but their product exists and can be inherited from the $SU(2)$ representation of O_h. Therefore, $S^-_{4z} = -\exp(iJ_z 2\pi/4)$, $\bar{S}^-_{4x} = \exp(iJ_x 2\pi/4)$, and $C^+_{31} = \exp(i(J_x+J_y+J_z)2\pi/(3\sqrt{3}))$. Similarly, $(S^-_{4z})^{-1}(k_x, k_y, k_z) = (-k_y, k_x, -k_z)$ and $(\bar{S}^-_{4x})^{-1}(k_x, k_y, k_z) = (-k_x, -k_z, k_y)$. The generators of T_d impose the following constraints on the Dirac Hamiltonian (Eq. 2.5),

$$\{S^-_{4z}, \gamma_z\} = \{\bar{S}^-_{4x}, \gamma_x\} = 0, \alpha_x\gamma_x = -\alpha_y S^-_{4z}\gamma_y S^{-\dagger}_{4z}, \alpha_y\gamma_y = -\alpha_z \bar{S}^-_{4x}\gamma_z \bar{S}^{-\dagger}_{4x}. \quad (2.11)$$

The only solution to the equations above is $\alpha_i = 0$. Therefore the tetrahedral group with mirror planes does not allow any Dirac points. This situation arises at Γ in the zincblende lattice (spacegroup 216), which has the symmetry of T_d. In Section 5.1 we prove group theoretically that time reversal and threefold rotation symmetry prevent the existence of three dimensional Dirac excitations in zincblende. However, the presence of mirror symmetry implies that a Dirac Hamiltonian is disallowed even in the absence of time reversal symmetry. Breaking mirror symmetry, on the other

hand, splits the fourfold degeneracy because the tetrahedral group T, does not exhibit four dimensional irreducible representations. Therefore, we conclude that regular representations of T_d cannot be described by a Dirac Hamiltonian.

Besides, O_h, O, and T_d, none of the remaining 29 point groups exhibit regular four dimensional irreducible representations. The remaining point groups exhibit twofold degenerate representations at high symmetry points in the BZ. However, if inversion and time reversal symmetry are present, energy eigenstates at every Bloch momentum $\mathbf{k}$ are twofold degenerate due to Kramers' theorem. Furthermore, rotation reflection symmetries act like inversion for every point along a line perpendicular to the reflection plane. Therefore, in the presence of rotation reflection symmetry, a twofold degenerate representation will remain degenerate along a line perpendicular to the reflection plane. We conclude that twofold degenerate representations can have a Dirac like dispersion only if the little group has no inversion or rotation reflection symmetry.

2.4. Linear splitting of Dirac points

Suppose there exists a FDIR at a point $\mathbf{k}_0$ in the BZ, and a comparison of rotation eigenvalues shows that if the four bands split linearly into distinct valence and conduction bands, the FDIR at $\mathbf{k}_0$ will have zero Chern number. It is not guaranteed however, that the FDIR will split linearly to leading order in $\mathbf{k}$. Indeed, in diamond, there exists a FDIR at Γ spanned by states belonging to a $p_{3/2}$ quadruplet, which splits into twofold degenerate bands that disperse quadratically away from Γ. In the face-centered-cubic lattice (spacegroup 209), there exists a FDIR at Γ that splits linearly, however it has nonzero Chern number due to the presence of threefold symmetry (Section 2.1). In the zincblende lattice on the other hand, the FDIR at Γ can disperse

linearly in all three directions, but exhibits a massive twofold degenerate [Fig. 2.3(c)] band along a threefold rotation axis due to mirror and time reversal symmetry.

We describe in this Section a group theoretic test based on characters of the FDIR in question and the vector representation of the symmetry group to determine whether the FDIR splits linearly in all three directions. This test was used in Dresselhaus (1955) to describe the band structure of zincblende structures in terms of powers of $\mathbf{k}$ around high symmetry points. We use $\mathbf{k}\cdot\mathbf{p}$ theory to explain our reasoning. Suppose we wish to determine the energy dispersion around a certain point $\mathbf{k}$ in the BZ for states $\psi_i^\mu(\mathbf{k},\mathbf{x})$ that span an irreducible representation $\Gamma_{\mathbf{k}}^\mu$ of $\mathrm{G}_{\mathbf{k}}$. Consider the Schrödinger equation with spin-orbit coupling (suppressing indices μ and i),

$$\left(\frac{\mathbf{p}^2}{2m}+V+\frac{\hbar}{4m^2c^2}(\nabla V\times\mathbf{p})\cdot\sigma\right)\psi(\mathbf{k},\mathbf{x})=\mathcal{E}_{\mathbf{k}}\psi(\mathbf{k},\mathbf{x}). \tag{2.12}$$

Due to translational symmetry $\psi(\mathbf{k},\mathbf{x})=u(\mathbf{k},\mathbf{x})e^{i\mathbf{k}\cdot\mathbf{x}}$ where $u(\mathbf{k},\mathbf{x})$ are lattice periodic Bloch functions that satisfy,

$$\left(\frac{\mathbf{p}^2}{2m}+V+\frac{\hbar}{4m^2c^2}(\sigma\times\nabla V)\cdot(\mathbf{p}+\hbar\mathbf{k})+\frac{\hbar\mathbf{k}\cdot\mathbf{p}}{m}\right)u(\mathbf{k},\mathbf{x})=\left(\mathcal{E}_{\mathbf{k}}-\frac{\hbar^2\mathbf{k}^2}{2m}\right)u(\mathbf{k},\mathbf{x}). \tag{2.13}$$

Following Dresselhaus (1955) we rewrite the Schrödinger equation for $u(\mathbf{k}+\delta\mathbf{k},\mathbf{x})$ where $\delta\mathbf{k}$ is a small displacement about $\mathbf{k}$, and ignore terms of $\mathcal{O}(\delta\mathbf{k}^2)$. This leads to a new term in Eq. (2.13),

$$\mathcal{H}'=\hbar\delta\mathbf{k}.\left(\frac{\mathbf{p}}{m}+\frac{\hbar}{4m^2c^2}(\sigma\times\nabla V\right)=\hbar\delta\mathbf{k}\cdot\mathbf{R}, \tag{2.14}$$

which we can treat as a perturbation and solve for the energy level $\mathcal{E}_{\mathbf{k}+\delta\mathbf{k},i}$ to linear

order in $\delta\mathbf{k}$ using perturbation theory.

$$\mathcal{E}_{\mathbf{k}+\delta\mathbf{k},i} = \mathcal{E}_{\mathbf{k},i} + \hbar\delta\mathbf{k} \cdot \mathrm{diag}\langle\psi_i^\mu(\mathbf{k})|\mathbf{R}|\psi_j^\mu(\mathbf{k})\rangle. \tag{2.15}$$

If the determinant of either of the matrices $A_l = \langle\psi_i^\mu(\mathbf{k})|R_l|\psi_j^\mu(\mathbf{k})\rangle$ vanishes, the fourfold degenerate energy level $\mathcal{E}_\mathbf{k}$ remains flat for at least one band. Hence the dispersion of the Dirac point will not be linear to lowest order for at least one band. The determinant is basis independent, and does not require knowledge of the states ψ_i^μ. Therefore we can check whether the vector valued components of the matrix $\mathbf{A}^{ij} = \langle\psi_i^\mu(\mathbf{k})|\mathbf{R}|\psi_j^\mu(\mathbf{k})\rangle$ are identically zero. Notice that $\mathbf{R}$ transforms under the vector representation $\Gamma_\mathbf{k}^V$ of $\mathrm{G_k}$. The first term in Eq. (2.14) is proportional to momentum, while the second is a spin-orbit term. The spin-orbit term transforms like a vector because $\vec{\sigma}$ does not change sign under inversion of coordinates despite the cross product in Eq. (2.14). The states $\psi_i^\mu(\mathbf{k},\mathbf{x})$ on the other hand, transform under the representation $\Gamma_\mathbf{k}^\mu$. Therefore the matrix elements $\langle\psi_i^\mu(\mathbf{k})|\mathbf{R}|\psi_j^\mu(\mathbf{k})\rangle$ will be nonzero if and if only if the Kronecker product representation $\Gamma_\mathbf{k}^{\mu*} \times \Gamma_\mathbf{k}^V \times \Gamma_\mathbf{k}^\mu$ contains the identity representation of $\mathrm{G}_\mathbf{k}$ (Bradley and Cracknell, 1976). If $\mathbf{k}$ is time reversal symmetric, the representation $\Gamma_\mathbf{k}^{\mu*}$ is unitarily equivalent to $\Gamma_\mathbf{k}^\mu$. In that case, it is sufficient to check that the symmetric Kronecker product $[\Gamma_\mathbf{k}^\mu \times \Gamma_\mathbf{k}^\mu]$ contains $\Gamma_\mathbf{k}^V$ (Hamermesh, 1989; Young et al., 2012).

We sketch a proof of the above assertions about Kronecker products adapted from Hamermesh (1989). We are interested in calculating the matrix elements $V_{ij}^{\mu\nu} = \langle\psi_i^\mu|V|\phi_j^\nu\rangle$ due to a perturbation V of the unperturbed Hamiltonian H_0. Here ψ_i^μ is the ith element of the irreducible representation Γ^μ of the symmetry group G of H_0 and ϕ_j^ν is the jth element of the irreducible representation Γ^ν of G. Notice the

distinct labeling of states as ϕ and ψ even for $\mu = \nu$ because the representation Γ^μ can occur at different energy levels at the same time. The orthogonality of distinct states belonging to the same representation and to different representations of the group G implies $V_{ij}^{\mu\nu} = 0$ unless the state vector $V\psi_j^\nu$ contains a function that transforms according to the ith row of the representation Γ^μ. Since V transforms under Γ^ρ, it can be written in terms of a basis set of functions that span Γ^ρ. Consequently, $V\psi_j^\nu$ can be written in terms of basis functions that span the representation $\Gamma^\rho \times \Gamma^\nu$ of G. The direct product $\Gamma^\rho \times \Gamma^\nu$ is, in general, reducible and if it does not contain the representation Γ^μ then the matrix element $V_{ij}^{\mu\nu}$ is guaranteed to vanish. Said differently, $V_{ij}^{\mu\nu}$ vanish if the direct product $\Gamma^{\mu*} \times \Gamma^\rho \times \Gamma^\nu$ does not contain the identity representation of G.

We are interested in matrix elements of the type $\langle\psi_i^\mu(\mathbf{k})|\mathbf{R}|\psi_j^\mu(\mathbf{k})\rangle$ where $|\psi_i^\mu(\mathbf{k})\rangle$ and $|\psi_j^\mu(\mathbf{k})\rangle$ belong to the *same* energy level, and span $\Gamma_\mathbf{k}^\mu$. If $\mathbf{k}$ is time reversal symmetric, then the representation $\Gamma_\mathbf{k}^{\mu*}$ is unitarily equivalent to $\Gamma_\mathbf{k}^\mu$. Consequently it is sufficient to consider whether $\Gamma_\mathbf{k}^\mu \times \Gamma_\mathbf{k}^V \times \Gamma_\mathbf{k}^\mu$ contains the identity representation of $\mathrm{G}_\mathbf{k}$. In general a direct product $\Gamma^\mu \times \Gamma^\mu$ consists of a symmetric part denoted $[\Gamma^\mu \times \Gamma^\mu]$ and an antisymmetric part, denoted $\{\Gamma^\mu \times \Gamma^\mu\}$. When the basis functions for the representations Γ^μ belong to the same energy level, only the symmetric combination occurs (Hamermesh, 1989). Therefore it is sufficient to check whether $\Gamma_\mathbf{k}^V$ occurs in the symmetric Kronecker product $[\Gamma_\mathbf{k}^\mu \times \Gamma_\mathbf{k}^\mu]$ for time reversal symmetric momenta $\mathbf{k}$.

Finally, even though group selection rules may permit linear splitting of bands away from the Dirac point, it is necessary to consider how the FDIR splits along lines of high symmetry. This depends on the little groups along high symmetry lines specific to each spacegroup. In general, there are three possibilities: the FDIR splits into (i) two doublets; (ii) four singlets; or (iii) one doublet and two singlets. Cases (i) and

(ii) guarantee that the valence and conduction bands are distinct [Figs. 2.3(a) and (b)] at either time reversal symmetric Dirac points or otherwise. If case (iii) occurs for a FDIR on a time reversal symmetric momentum, the twofold degenerate band remains flat due to Kramers theorem and cannot develop a finite slope. Consequently a conduction and a valence band are degenerate along a line away from the Dirac point and remain flat to linear order in $\mathbf{k}$ [Fig. 2.3(c)]. This behavior disallows a Dirac Hamiltonian, as is the case for zincblende at Γ (Young et al., 2012). However, if case (iii) occurs in the vicinity of a FDIR on a momentum which is not time reversal symmetric, it is possible for the conduction and valence bands to be distinct [Fig. 2.3(d)], and the FDIR can be described by a Dirac Hamiltonian.

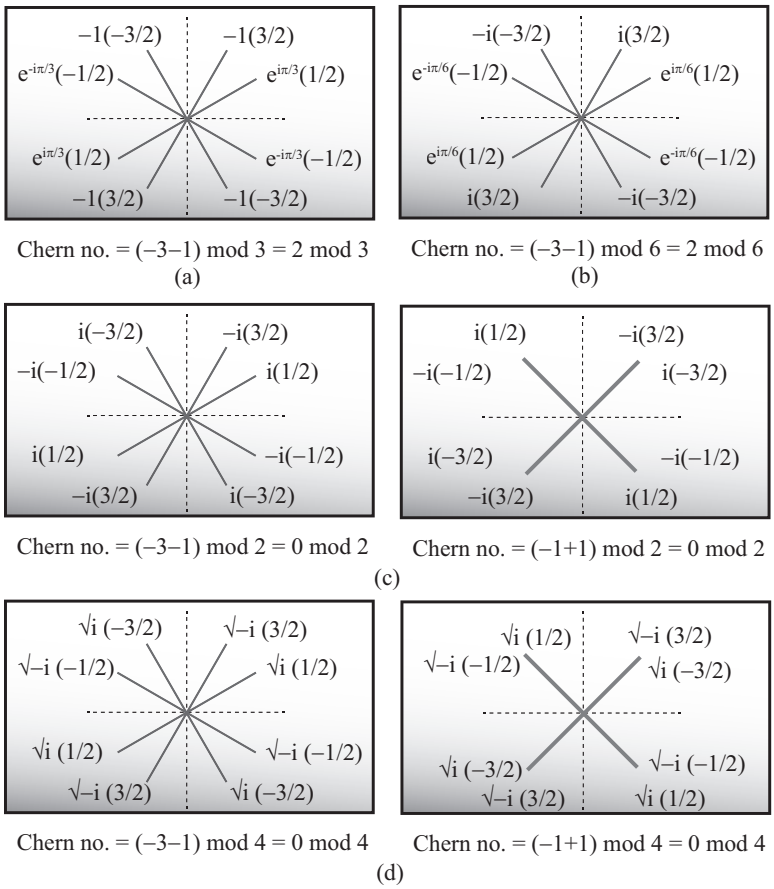

Figure 2.1: Chern number modulo n of a Dirac point occurring at a time reversal symmetric momentum in the presence of a $2\pi/n$ rotation symmetry. In all cases (a-d) we assume that the bands disperse linearly such that the only degeneracy occurs at the Dirac point. Indicated with each band is the rotation eigenvalue $e^{2\pi ij/n}$ with the corresponding j in brackets. The assignment of j to a certain band is arbitrary upto certain restrictions imposed by time reversal symmetry. For example, in (a) a different assignment of j eigenvalues to each band results in a Chern number of 1 mod 3. (a) Threefold rotation symmetry, $n = 3$. The Dirac point splits into four nondegenerate bands and exhibits nonzero Chern number. (b) Sixfold rotation symmetry, $n = 6$. The Dirac point splits into four nondegenerate bands and exhibits nonzero Chern number. (c) Twofold rotation symmetry, $n = 2$. The Dirac point splits into four nondegenerate bands (Left), or twofold degenerate bands (Right). In either case the Chern number is 0 modulo 2. (d) Fourfold rotation symmetry, $n = 4$. The Dirac point splits into four nondegenerate bands (Left), or twofold degenerate bands (Right). In either case the Chern number is 0 modulo 4.

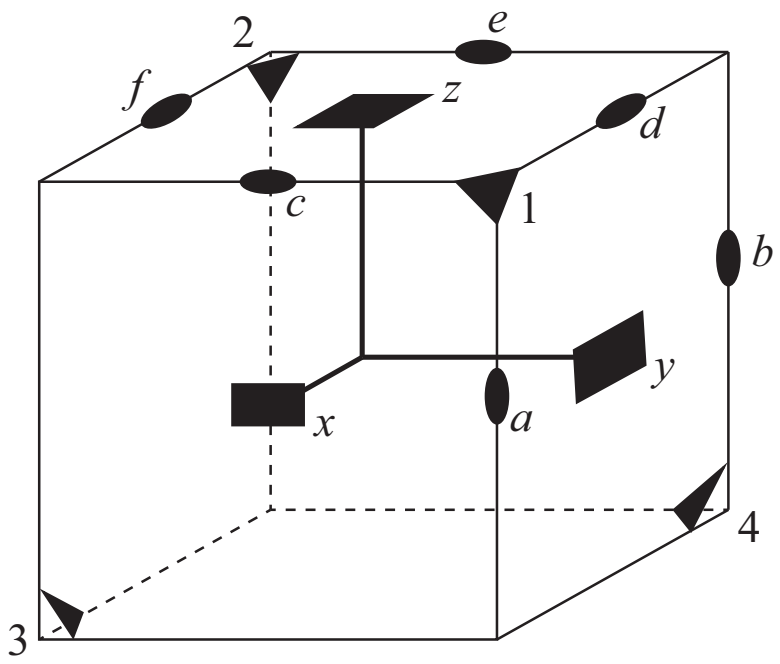

Figure 2.2: Rotational elements of the cubic point group. Three fourfold rotation axes labeled x, y, and z bisect the six cube faces. Four threefold rotation axes labeled $1, 2, 3$ and 4 join the eight diagonal corners, whereas the six twofold rotation axes labeled a, b, c, d, e and f connect the six opposite edges of a regular cube. Mirror and rotation reflection operations can be obtained by multiplying rotations with inversion.

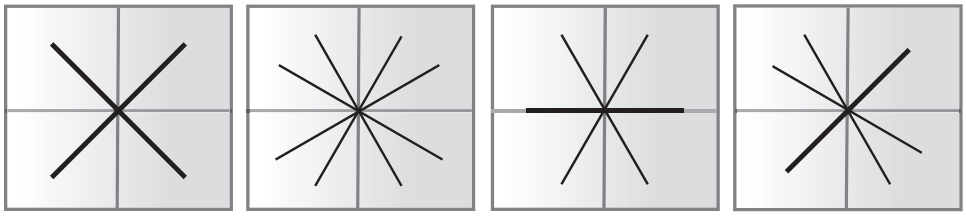

Figure 2.3: Linear splitting of fourfold degenerate irreducible representations (FDIRs). If the symmetric Kronecker product of a FDIR with itself contains the vector representation of the group to which the FDIR belongs, it will split in one of the four possible ways displayed above. (a) The FDIR splits into two twofold degenerate bands. This situation is realized at the X point of the FCC Brillouin zone in a diamond lattice. (b) The FDIR splits into four nondegenerate bands. This situation arises at the Γ point in zincblende if mirror symmetry is broken (although the FDIR in zincblende develops a nonzero Chern number due to threefold rotation symmetry at Γ). (c) The FDIR occurring at a time reversal symmetric momentum splits into two nondegenerate and one twofold degenerate band dispersing linearly. The twofold degenerate band is constrained to be flat implying quadratic dispersion along that direction. This situation arises in zincblende (HgTe for instance) at Γ along the (111) axis. (d) The FDIR occurring at a non time reversal symmetric momentum splits into two nondegenerate and one twofold degenerate band dispersing linearly.

Chapter 3

Dirac points in three dimensional space-groups

In this Chapter, we provide a list of all BZ momenta in the 230 spacegroups which exhibit three dimensional Dirac points. The methods used to classify candidate Dirac points have been discussed in previous chapters. Here we provide a guide to interpreting the various symbols and notation used in the tables of Dirac points.

Spacegroups are identified using both the numerical ordering chosen by the International Union of Crystallography and their International Symbols (Hermann-Mauguin notation). For example, the spacegroup of diamond is identified as 227 Fd3m. At the beginning of each table, the Bravais lattice is identified where $\{\mathbf{t}_i\}$ and $\{\mathbf{g}_i\}$ denote the primitive and reciprocal lattice vectors respectively. The lattice constants are given in terms of real valued parameters a, b, c. The first column under each spacegroup identifies the high symmetry BZ momentum $\mathbf{k} = (xyz) = x\mathbf{g}_1 + y\mathbf{g}_2 + z\mathbf{g}_3$ in terms of real parameters x, y, z. $\bar{x} \equiv -x$. For instance in spacegroup 11 $P2_1/m$, the high symmetry point $C = (0\frac{1}{2}\frac{1}{2})$ should be interpreted as having coordinates $\frac{1}{2}\mathbf{g}_2 + \frac{1}{2}\mathbf{g}_3$. A high symmetry point $\mathbf{k}$ is time reversal symmetric if all of x, y, z carry values which are either $0, \frac{1}{2}, \frac{\bar{1}}{2}$. Only those BZ momenta are identified which exhibit a Dirac point.

The second column identifies the abstract group G_p^n which is isomorphic to the double valued central extension group $G_{\mathbf{k}}^{0*}$ of the isogonal point group $G_{\mathbf{k}}^0$. We do not identify $G_{\mathbf{k}}^0$ for any $\mathbf{k}$ because its representations are irrelevant unless $G_{\mathbf{k}}^0$ is the same as G_p^n. In some cases the abstract group in the second column appears as $G_p^n \otimes T_n$ where T_n is an

abelian group of order n. Abelian groups have one dimensional representations so the representations of $\mathrm{G}_{\mathrm{p}}^{\mathrm{n}} \otimes \mathrm{T}_{\mathrm{n}}$ are identified from among the representations of $\mathrm{G}_{\mathrm{p}}^{\mathrm{n}}$. The third column identifies the generators of the little group $\mathrm{G}_{\mathbf{k}}$ in Herring's spacegroup notation as $\{\mathrm{R}|\mathbf{t}\}$. Here R represents a point group operation such as rotation C, mirror σ, inversion I, or identity E. Operations denoted by S are combinations of a rotation and inversion. $\mathbf{t}$ is the accompanying nonprimitive lattice translation given as (xyz).

In the fourth column, we identify the FDIR R_{m} of $\mathrm{G}_{\mathrm{p}}^{\mathrm{n}}$ that occurs at $\mathbf{k}$. In most cases, time reversal symmetry guarantees the FDIR to be the direct sum $\mathrm{R}_{\mathrm{n}} \oplus \mathrm{R}_{\mathrm{p}}$ of two dimensional representations R_{n} and R_{p}. Characters of specific representations can be identified from the character tables of abstract groups in Bradley and Cracknell (1976). In the fifth column, we identify the vector representation Γ^V of the little group. The vector representation depends on the generators of the little group $\mathrm{G}_{\mathbf{k}}$. For example, the abstract group G_{16}^{10} has two different vector representations depending on whether it has generators $\{\mathrm{C}_2, \mathrm{E}, \mathrm{I}\}$ or $\{\sigma, \mathrm{E}, \mathrm{I}\}$. Translations $\mathbf{t}$ in a spacegroup operator are irrelevant in determining the vector representation. In the sixth column, we indicate how the Dirac point splits along lines of high symmetry away from $\mathbf{k}$. High symmetry lines are identified by their alphabetical symbols as in Bradley and Cracknell (1976) and their coordinates are given as (xyz) where some or all of x, y, z are given in terms of a parameter α or $\bar{\alpha}$ where $0 < \alpha < \frac{1}{2}$. In the sixth column, the splitting of the Dirac point is indicated as $\mathrm{A} \rightarrow \mathrm{u}$, where A denotes the high symmetry line and $u = a, b, d$ which correspond to the captions of Figure 2.3. For example, in spacegroup 11 $\mathrm{P2_1/m}$ the Dirac point at Z splits into twofold degenerate bands, as in Figure 2.3(a), along $\Lambda = \alpha \mathbf{g}_3$ where $0 < \alpha < \frac{1}{2}$.

For brevity, we omit information indicating how many times the vector representation

Γ^{V} occurs in the symmetric Kronecker product $[\Gamma_{\mathbf{k}} \otimes \Gamma_{\mathbf{k}}]$ of the FDIR $\Gamma_{\mathbf{k}}$ in the case of time reversal symmetric momenta $\mathbf{k}$, or whether $\Gamma^{*}_{\mathbf{k}'} \otimes \Gamma^{V} \otimes \Gamma_{\mathbf{k}'}$ contains the identity representation R_1 for non time reversal symmetric momenta $\mathbf{k}'$, although that information has been collected and used to identify the candidate Dirac points.

3.1. Tables of symmetry protected Dirac points

Monoclinic Primitive Lattice Γ_m

Real lattice vectors $\mathbf{t}_i$	$\{(0,-b,0),(a\sin\gamma,-a\cos\gamma,0),(0,0,c)\}$
Reciprocal lattice vectors $\mathbf{g}_i$	$\{2\pi/b(-\cot\gamma,-1,0),2\pi/a(\csc\gamma,0,0),2\pi/c(0,0,1)\}$
High symmetry points	Z = $(00\frac{1}{2})$, C = $(0\frac{1}{2}\frac{1}{2})$ D = $(\bar{\frac{1}{2}}0\frac{1}{2})$, E = $(\frac{1}{2}\frac{1}{2}\frac{1}{2})$, B = $(\bar{\frac{1}{2}}00)$, A = $(\frac{1}{2}\frac{1}{2}0)$
High symmetry lines	Λ = (00α), W = $(0\frac{1}{2}\alpha)$, V = $(\bar{\frac{1}{2}}0\alpha)$, U = $(\frac{1}{2}\frac{1}{2}\alpha)$, Δ = $(\bar{\alpha}00)$, Σ = $(0\alpha0)$

11 $P2_1/m$

Z	G_{16}^{10}	$[\{C_{2z}\|00\frac{1}{2}\},\{E\|001\},\{I\|00\bar{\frac{1}{2}}\}]$	$R_9\oplus R_9$	$R_2\oplus R_2\oplus R_4$	$\Lambda\to a$
C	G_{16}^{10}	$[\{C_{2z}\|00\frac{1}{2}\},\{E\|001\},\{I\|00\bar{\frac{1}{2}}\}]$	$R_9\oplus R_9$	$R_2\oplus R_2\oplus R_4$	$W\to a$
D	G_{16}^{10}	$[\{C_{2z}\|00\frac{1}{2}\},\{E\|001\},\{I\|00\bar{\frac{1}{2}}\}]$	$R_9\oplus R_9$	$R_2\oplus R_2\oplus R_4$	$V\to a$
E	G_{16}^{10}	$[\{C_{2z}\|00\frac{1}{2}\},\{E\|001\},\{I\|00\bar{\frac{1}{2}}\}]$	$R_9\oplus R_9$	$R_2\oplus R_2\oplus R_4$	$U\to a$

13 P2/b

B	G_{16}^{10}	$[\{\sigma_z\|\bar{\frac{1}{2}}00\},\{E\|100\},\{I\|\bar{\frac{1}{2}}00\}]$	$R_9\oplus R_9$	$R_2\oplus R_4\oplus R_4$	$V\to a$
A	G_{16}^{10}	$[\{\sigma_z\|\bar{\frac{1}{2}}00\},\{E\|100\},\{I\|\bar{\frac{1}{2}}00\}]$	$R_9\oplus R_9$	$R_2\oplus R_4\oplus R_4$	$U\to a$
D	G_{16}^{10}	$[\{\sigma_z\|\bar{\frac{1}{2}}00\},\{E\|100\},\{I\|\bar{\frac{1}{2}}00\}]$	$R_9\oplus R_9$	$R_2\oplus R_4\oplus R_4$	$V\to a$
E	G_{16}^{10}	$[\{\sigma_z\|\bar{\frac{1}{2}}00\},\{E\|100\},\{I\|\bar{\frac{1}{2}}00\}]$	$R_9\oplus R_9$	$R_2\oplus R_4\oplus R_4$	$U\to a$

14 $P2_1/b$

B	G_{16}^{10}	$[\{\sigma_z\|\bar{\frac{1}{2}}00\},\{E\|100\},\{I\|\bar{\frac{1}{2}}0\bar{\frac{1}{2}}\}]$	$R_9\oplus R_9$	$R_2\oplus R_4\oplus R_4$	$V\to a$
A	G_{16}^{10}	$[\{\sigma_z\|\bar{\frac{1}{2}}00\},\{E\|001\},\{I\|\bar{\frac{1}{2}}0\bar{\frac{1}{2}}\}]$	$R_9\oplus R_9$	$R_2\oplus R_4\oplus R_4$	$U\to a$
Z	G_{16}^{10}	$[\{C_{2z}\|00\frac{1}{2}\},\{E\|001\},\{I\|\bar{\frac{1}{2}}0\bar{\frac{1}{2}}\}]$	$R_9\oplus R_9$	$R_2\oplus R_2\oplus R_4$	$\Lambda\to a$
C	G_{16}^{10}	$[\{C_{2z}\|00\frac{1}{2}\},\{E\|001\},\{I\|\bar{\frac{1}{2}}0\bar{\frac{1}{2}}\}]$	$R_9\oplus R_9$	$R_2\oplus R_2\oplus R_4$	$W\to a$

Table 3.1: Symmetry protected Dirac points in the Monoclinic Primitive Lattice

Monoclinic Base-centered Lattice Γ_m^b

Real lattice vectors $\mathbf{t}_i$	$\{(0,-b,0), 1/2(a\sin\gamma, -a\cos\gamma, -c),$ $1/2(a\sin\gamma, -a\cos\gamma, c)\}$
Reciprocal lattice vectors $\mathbf{g}_i$	$\{2\pi/b(-\cot\gamma, -1, 0), 2\pi/ac(c\csc\gamma, 0, -a),$ $2\pi/ac(c\csc\gamma, 0, a)\}$
High symmetry points	A $= (\frac{1}{2}00)$, M $= (\frac{1}{2}\frac{1}{2}\frac{1}{2})$
High symmetry lines	U $= (\frac{1}{2}\bar{\alpha}\alpha)$, $\Lambda = (00\alpha)$

15 B2/b

A	G_{16}^{10}	$[\{\sigma_z\|\frac{1}{2}00\}, \{E\|100\}, \{I\|\frac{1}{2}00\}]$	$R_9 \oplus R_9$	$R_2 \oplus R_4 \oplus R_4$	U $\to$ a
M	G_{16}^{10}	$[\{\sigma_z\|\frac{1}{2}00\}, \{E\|100\}, \{I\|\frac{1}{2}00\}]$	$R_9 \oplus R_9$	$R_2 \oplus R_4 \oplus R_4$	U $\to$ a

Table 3.2: Symmetry protected Dirac points in the Monoclinic Base-centered Lattice

Orthorhombic Primitive Γ_0

Real lattice vectors $\mathbf{t}_i$	$\{(0,-b,0),(a,0,0),(0,0,c)\}$
Reciprocal lattice vectors $\mathbf{g}_i$	$\{2\pi/b(0,-1,0),2\pi/a(1,0,0),2\pi/c(0,0,1)\}$
High symmetry points	S = $(\bar{\frac{1}{2}}\frac{1}{2}0)$, R = $(\bar{\frac{1}{2}}\frac{1}{2}\frac{1}{2})$, U = $(0\frac{1}{2}\frac{1}{2})$, T = $(\bar{\frac{1}{2}}0\frac{1}{2})$, Z = $(00\frac{1}{2})$, Y = $(\bar{\frac{1}{2}}00)$, X = $(0\frac{1}{2}0)$
High symmetry lines	C = $(\bar{\frac{1}{2}}\alpha 0)$, D = $(\bar{\alpha}\frac{1}{2}0)$, Q = $(\bar{\frac{1}{2}}\frac{1}{2}\alpha)$, P = $(\bar{\alpha}\frac{1}{2}\frac{1}{2})$, E = $(\frac{1}{2}\alpha\frac{1}{2})$, A = $(0\alpha\frac{1}{2})$, G = $(0\frac{1}{2}\alpha)$, H = $(\bar{\frac{1}{2}}0\alpha)$, B = $(\bar{\alpha}0\frac{1}{2})$, $\Lambda = (00\alpha)$

18 $P2_12_12$

S	G_{16}^8	$[\{C_{2z}\|000\},\{C_{2x}\|\frac{1}{2}\frac{1}{2}0\}]$	$R_9\oplus R_9$	$R_2\oplus R_3\oplus R_4$	$[C,D,Q]\to a$
R	G_{16}^8	$[\{C_{2z}\|000\},\{C_{2x}\|\frac{1}{2}\frac{1}{2}0\}]$	$R_9\oplus R_9$	$R_2\oplus R_3\oplus R_4$	$[Q,P,E]\to a$

19 $P2_12_12_1$

U	G_{16}^8	$[\{C_{2y}\|\frac{1}{2}\frac{1}{2}0\},\{C_{2z}\|\frac{1}{2}0\frac{1}{2}\}]$	$R_9\oplus R_9$	$R_2\oplus R_3\oplus R_4$	$[A,G,P]\to a$
T	G_{16}^8	$[\{C_{2x}\|0\frac{1}{2}\frac{1}{2}\},\{C_{2y}\|\frac{1}{2}\frac{1}{2}0\}]$	$R_9\oplus R_9$	$R_2\oplus R_3\oplus R_4$	$[H,B,E]\to a$
S	G_{16}^8	$[\{C_{2z}\|\frac{1}{2}0\frac{1}{2}\},\{C_{2x}\|0\frac{1}{2}\frac{1}{2}\}]$	$R_9\oplus R_9$	$R_2\oplus R_3\oplus R_4$	$[C,D,Q]\to a$

26 $Pmc2_1$

Z	G_{16}^8	$[\{\sigma_x\|000\},\{\sigma_y\|00\frac{1}{2}\}]$	$R_9\oplus R_9$	$R_1\oplus R_2\oplus R_3$	$[A,B,\Lambda]\to a$
U	G_{16}^8	$[\{\sigma_x\|000\},\{\sigma_y\|00\frac{1}{2}\}]$	$R_9\oplus R_9$	$R_1\oplus R_2\oplus R_3$	$[A,G,P]\to a$
T	G_{16}^8	$[\{\sigma_x\|000\},\{\sigma_y\|00\frac{1}{2}\}]$	$R_9\oplus R_9$	$R_1\oplus R_2\oplus R_3$	$[H,B,E]\to a$
R	G_{16}^8	$[\{\sigma_x\|000\},\{\sigma_y\|00\frac{1}{2}\}]$	$R_9\oplus R_9$	$R_1\oplus R_2\oplus R_3$	$[E,P,Q]\to a$

27 Pcc2

Z	G_{16}^8	$[\{C_{2z}\|000\},\{\sigma_x\|00\frac{1}{2}\}]$	$R_9\oplus R_9$	$R_1\oplus R_3\oplus R_4$	$\Lambda\to a,[A,B]\to b$
U	G_{16}^8	$[\{C_{2z}\|000\},\{\sigma_x\|00\frac{1}{2}\}]$	$R_9\oplus R_9$	$R_1\oplus R_3\oplus R_4$	$G\to a,[A,P]\to b$
T	G_{16}^8	$[\{C_{2z}\|000\},\{\sigma_x\|00\frac{1}{2}\}]$	$R_9\oplus R_9$	$R_1\oplus R_3\oplus R_4$	$E\to a,[H,B]\to b$
R	G_{16}^8	$[\{C_{2z}\|000\},\{\sigma_x\|00\frac{1}{2}\}]$	$R_9\oplus R_9$	$R_1\oplus R_3\oplus R_4$	$E\to a,[P,Q]\to b$

29 $Pca2_1$

Z	G_{16}^8	$[\{\sigma_x\|\frac{1}{2}00\},\{\sigma_y\|00\frac{1}{2}\}]$	$R_9\oplus R_9$	$R_1\oplus R_2\oplus R_3$	$[A,B,\Lambda]\to a$
U	G_{16}^8	$[\{\sigma_x\|\frac{1}{2}00\},\{\sigma_y\|00\frac{1}{2}\}]$	$R_9\oplus R_9$	$R_1\oplus R_2\oplus R_3$	$[A,G,P]\to a$

30 Pnc2

Z	G_{16}^8	$[\{C_{2z}\|\frac{1}{2}00\},\{\sigma_x\|\frac{1}{2}0\frac{1}{2}\}]$	$R_9\oplus R_9$	$R_1\oplus R_3\oplus R_4$	$[A,B,\Lambda]\to a$
U	G_{16}^8	$[\{C_{2z}\|\frac{1}{2}00\},\{\sigma_x\|\frac{1}{2}0\frac{1}{2}\}]$	$R_9\oplus R_9$	$R_1\oplus R_3\oplus R_4$	$[A,G,P]\to a$

Table 3.3: Symmetry protected Dirac points in the Orthorhombic Primitive Lattice

31 $Pmn2_1$					
Z	G_{16}^8	$[\{\sigma_y\|000\},\{C_{2z}\|\frac{1}{2}0\frac{1}{2}\}]$	$R_9 \oplus R_9$	$R_1 \oplus R_2 \oplus R_4$	$[A, B, \Lambda] \to a$
U	G_{16}^8	$[\{\sigma_y\|000\},\{C_{2z}\|\frac{1}{2}0\frac{1}{2}\}]$	$R_9 \oplus R_9$	$R_1 \oplus R_2 \oplus R_4$	$[A, G, P] \to a$
32 Pba2					
S	G_{16}^8	$[\{C_{2z}\|\frac{1}{2}\frac{1}{2}0\},\{\sigma_x\|\frac{1}{2}00\}]$	$R_9 \oplus R_9$	$R_1 \oplus R_3 \oplus R_4$	$[C, D, Q] \to a$
R	G_{16}^8	$[\{C_{2z}\|\frac{1}{2}\frac{1}{2}0\},\{\sigma_x\|\frac{1}{2}00\}]$	$R_9 \oplus R_9$	$R_1 \oplus R_3 \oplus R_4$	$[E, P, Q] \to a$
33 $Pna2_1$					
Z	G_{16}^8	$[\{\sigma_x\|\frac{1}{2}00\},\{\sigma_y\|0\frac{1}{2}\frac{1}{2}\}]$	$R_9 \oplus R_9$	$R_1 \oplus R_2 \oplus R_3$	$[A, B, \Lambda] \to a$
S	G_{16}^8	$[\{C_{2z}\|\frac{1}{2}\frac{1}{2}\frac{1}{2}\},\{\sigma_x\|\frac{1}{2}00\}]$	$R_9 \oplus R_9$	$R_1 \oplus R_3 \oplus R_4$	$[C, D, Q] \to a$
R	G_{16}^8	$[\{\sigma_y\|0\frac{1}{2}\frac{1}{2}\},\{C_{2z}\|\frac{1}{2}\frac{1}{2}\frac{1}{2}\}]$	$R_9 \oplus R_9$	$R_1 \oplus R_2 \oplus R_4$	$[E, P, Q] \to a$
34 Pnn2					
Z	G_{16}^8	$[\{C_{2z}\|\frac{1}{2}\frac{1}{2}0\},\{\sigma_x\|\frac{1}{2}0\frac{1}{2}\}]$	$R_9 \oplus R_9$	$R_1 \oplus R_3 \oplus R_4$	$[A, B, \Lambda] \to a$
S	G_{16}^8	$[\{C_{2z}\|\frac{1}{2}\frac{1}{2}0\},\{\sigma_x\|\frac{1}{2}0\frac{1}{2}\}]$	$R_9 \oplus R_9$	$R_1 \oplus R_3 \oplus R_4$	$[C, D, Q] \to a$
48 Pnnn					
Y	G_{32}^7	$[\{\sigma_z\|\frac{1}{2}\frac{1}{2}\frac{1}{2}\},\{\sigma_y\|\frac{1}{2}\frac{1}{2}\frac{1}{2}\},\{I\|\frac{1}{2}\frac{1}{2}\frac{1}{2}\}]$	$R_{13} \oplus R_{14}$	$R_2 \oplus R_4 \oplus R_6$	$[C, H, \Delta] \to a$
U	G_{32}^7	$[\{\sigma_z\|\frac{1}{2}\frac{1}{2}\frac{1}{2}\},\{\sigma_y\|\frac{1}{2}\frac{1}{2}\frac{1}{2}\},\{I\|\frac{1}{2}\frac{1}{2}\frac{1}{2}\}]$	$R_{13} \oplus R_{14}$	$R_2 \oplus R_4 \oplus R_6$	$[A, P, G] \to a$
X	G_{32}^7	$[\{\sigma_y\|\frac{1}{2}\frac{1}{2}\frac{1}{2}\},\{\sigma_x\|\frac{1}{2}\frac{1}{2}\frac{1}{2}\},\{I\|\frac{1}{2}\frac{1}{2}\frac{1}{2}\}]$	$R_{13} \oplus R_{14}$	$R_2 \oplus R_4 \oplus R_6$	$[G, D, \Sigma] \to a$
T	G_{32}^7	$[\{\sigma_y\|\frac{1}{2}\frac{1}{2}\frac{1}{2}\},\{\sigma_x\|\frac{1}{2}\frac{1}{2}\frac{1}{2}\},\{I\|\frac{1}{2}\frac{1}{2}\frac{1}{2}\}]$	$R_{13} \oplus R_{14}$	$R_2 \oplus R_4 \oplus R_6$	$[H, B, E] \to a$
Z	G_{32}^7	$[\{\sigma_x\|\frac{1}{2}\frac{1}{2}\frac{1}{2}\},\{\sigma_z\|\frac{1}{2}\frac{1}{2}\frac{1}{2}\},\{I\|\frac{1}{2}\frac{1}{2}\frac{1}{2}\}]$	$R_{13} \oplus R_{14}$	$R_2 \oplus R_4 \oplus R_6$	$[A, B, \Lambda] \to a$
S	G_{32}^7	$[\{\sigma_x\|\frac{1}{2}\frac{1}{2}\frac{1}{2}\},\{\sigma_z\|\frac{1}{2}\frac{1}{2}\frac{1}{2}\},\{I\|\frac{1}{2}\frac{1}{2}\frac{1}{2}\}]$	$R_{13} \oplus R_{14}$	$R_2 \oplus R_4 \oplus R_6$	$[C, D, Q] \to a$
49 Pccm					
U	G_{32}^7	$[\{\sigma_x\|00\frac{1}{2}\},\{\sigma_z\|00\frac{1}{2}\},\{I\|00\frac{1}{2}\}]$	$R_{13} \oplus R_{14}$	$R_2 \oplus R_4 \oplus R_6$	$[A, P, G] \to a$
T	G_{32}^7	$[\{\sigma_x\|00\frac{1}{2}\},\{\sigma_z\|00\frac{1}{2}\},\{I\|00\frac{1}{2}\}]$	$R_{13} \oplus R_{14}$	$R_2 \oplus R_4 \oplus R_6$	$[H, B, E] \to a$
Z	G_{32}^7	$[\{\sigma_x\|00\frac{1}{2}\},\{\sigma_z\|00\frac{1}{2}\},\{I\|00\frac{1}{2}\}]$	$R_{13} \oplus R_{14}$	$R_2 \oplus R_4 \oplus R_6$	$[A, B, \Lambda] \to a$
R	G_{32}^7	$[\{\sigma_x\|00\frac{1}{2}\},\{\sigma_z\|00\frac{1}{2}\},\{I\|00\frac{1}{2}\}]$	$R_{13} \oplus R_{14}$	$R_2 \oplus R_4 \oplus R_6$	$[E, P, Q] \to a$
50 Pmma					
Y	G_{32}^7	$[\{\sigma_z\|\frac{1}{2}\frac{1}{2}0\},\{\sigma_y\|\frac{1}{2}\frac{1}{2}0\},\{I\|\frac{1}{2}\frac{1}{2}0\}]$	$R_{13} \oplus R_{14}$	$R_2 \oplus R_4 \oplus R_6$	$[C, H, \Delta] \to a$
U	G_{32}^7	$[\{\sigma_z\|\frac{1}{2}\frac{1}{2}0\},\{\sigma_x\|\frac{1}{2}\frac{1}{2}0\},\{I\|\frac{1}{2}\frac{1}{2}0\}]$	$R_{13} \oplus R_{14}$	$R_2 \oplus R_4 \oplus R_6$	$[A, P, G] \to a$
X	G_{32}^7	$[\{\sigma_z\|\frac{1}{2}\frac{1}{2}0\},\{\sigma_x\|\frac{1}{2}\frac{1}{2}0\},\{I\|\frac{1}{2}\frac{1}{2}0\}]$	$R_{13} \oplus R_{14}$	$R_2 \oplus R_4 \oplus R_6$	$[G, D, \Sigma] \to a$
T	G_{32}^7	$[\{\sigma_z\|\frac{1}{2}\frac{1}{2}0\},\{\sigma_y\|\frac{1}{2}\frac{1}{2}0\},\{I\|\frac{1}{2}\frac{1}{2}0\}]$	$R_{13} \oplus R_{14}$	$R_2 \oplus R_4 \oplus R_6$	$[H, B, E] \to a$
R	G_{32}^7	$[\{\sigma_x\|\frac{1}{2}\frac{1}{2}0\},\{\sigma_z\|\frac{1}{2}\frac{1}{2}0\},\{I\|\frac{1}{2}\frac{1}{2}0\}]$	$R_{13} \oplus R_{14}$	$R_2 \oplus R_4 \oplus R_6$	$[E, P, Q] \to a$
S	G_{32}^7	$[\{\sigma_x\|\frac{1}{2}\frac{1}{2}0\},\{\sigma_z\|\frac{1}{2}\frac{1}{2}0\},\{I\|\frac{1}{2}\frac{1}{2}0\}]$	$R_{13} \oplus R_{14}$	$R_2 \oplus R_4 \oplus R_6$	$[C, D, Q] \to a$

Symmetry protected Dirac points in the Orthorhombic Primitive Lattice (ii) of (iii)

52 Pnna[1]

Y	G_{32}^7	$[\{\sigma_z\|\frac{1}{2}\frac{1}{2}\frac{1}{2}\}, \{\sigma_y\|\frac{1}{2}\frac{1}{2}0\}, \{I\|\frac{1}{2}\frac{1}{2}0\}]$	$R_{13} \oplus R_{14}$	$R_2 \oplus R_4 \oplus R_6$	$[C, H, \Delta] \to a$
X	G_{32}^7	$[\{\sigma_y\|\frac{1}{2}\frac{1}{2}0\}, \{\sigma_x\|\frac{1}{2}\frac{1}{2}\frac{1}{2}\}, \{I\|\frac{1}{2}\frac{1}{2}0\}]$	$R_{13} \oplus R_{14}$	$R_2 \oplus R_4 \oplus R_6$	$[G, D, \Sigma] \to a$
S	G_{32}^7	$[\{\sigma_x\|\frac{1}{2}\frac{1}{2}\frac{1}{2}\}, \{\sigma_z\|\frac{1}{2}\frac{1}{2}\frac{1}{2}\}, \{I\|\frac{1}{2}\frac{1}{2}0\}]$	$R_{13} \oplus R_{14}$	$R_2 \oplus R_4 \oplus R_6$	$[C, D, Q] \to a$

53 Pmna[2]

Y	G_{32}^7	$[\{\sigma_z\|\frac{1}{2}0\frac{1}{2}\}, \{\sigma_y\|\frac{1}{2}00\}, \{I\|\frac{1}{2}00\}]$	$R_{13} \oplus R_{14}$	$R_2 \oplus R_4 \oplus R_6$	$[C, H, \Delta] \to a$
S	G_{32}^7	$[\{\sigma_z\|\frac{1}{2}0\frac{1}{2}\}, \{\sigma_y\|\frac{1}{2}00\}, \{I\|\frac{1}{2}00\}]$	$R_{13} \oplus R_{14}$	$R_2 \oplus R_4 \oplus R_6$	$[C, D, Q] \to a$

54 Pcca[3]

X	G_{32}^7	$[\{\sigma_y\|0\frac{1}{2}0\}, \{\sigma_x\|0\frac{1}{2}\frac{1}{2}\}, \{I\|0\frac{1}{2}0\}]$	$R_{13} \oplus R_{14}$	$R_2 \oplus R_4 \oplus R_6$	$[G, D, \Sigma] \to a$
S	G_{32}^7	$[\{\sigma_y\|0\frac{1}{2}0\}, \{\sigma_x\|0\frac{1}{2}\frac{1}{2}\}, \{I\|0\frac{1}{2}0\}]$	$R_{13} \oplus R_{14}$	$R_2 \oplus R_4 \oplus R_6$	$[C, D, Q] \to a$

56 Pccn[4]

Z	G_{32}^7	$[\{\sigma_x\|00\frac{1}{2}\}, \{\sigma_z\|\frac{1}{2}\frac{1}{2}\frac{1}{2}\}, \{I\|\frac{1}{2}\frac{1}{2}\frac{1}{2}\}]$	$R_{13} \oplus R_{14}$	$R_2 \oplus R_4 \oplus R_6$	$[A, B, \Lambda] \to a$

58 Pnnm[5]

Z	G_{32}^7	$[\{\sigma_x\|\frac{1}{2}\frac{1}{2}\frac{1}{2}\}, \{\sigma_z\|00\frac{1}{2}\}, \{I\|00\frac{1}{2}\}]$	$R_{13} \oplus R_{14}$	$R_2 \oplus R_4 \oplus R_6$	$[A, B, \Lambda] \to a$

60 Pbcn[6]

Z	G_{32}^7	$[\{\sigma_x\|0\frac{1}{2}\frac{1}{2}\}, \{\sigma_z\|\frac{1}{2}0\frac{1}{2}\}, \{I\|\frac{1}{2}0\frac{1}{2}\}]$	$R_{13} \oplus R_{14}$	$R_2 \oplus R_4 \oplus R_6$	$[A, B, \Lambda] \to a$

Symmetry protected Dirac points in the Orthorhombic Primitive Lattice (iii) of (iii)

Orthorhombic Base-centered Lattice Γ_0^b

Real lattice vectors $\mathbf{t}_i$	$\{1/2(a,-b,0), 1/2(a,b,0), (0,0,c)\}$
	Type(1) a > b; (2) b > a
Reciprocal lattice vectors $\mathbf{g}_i$	$\{2\pi/ba(b,-a,0), 2\pi/ba(b,a,0), 2\pi/c(0,0,1)\}$
High symmetry points	Z = $(00\frac{1}{2})$, T(1) = $(\frac{1}{2}\frac{1}{2}\frac{1}{2})$, T(2) = $(\bar{\frac{1}{2}}\frac{1}{2}\frac{1}{2})$, R = $(0\frac{1}{2}\frac{1}{2})$, S = $(0\frac{1}{2}0)$
High symmetry lines	A = $(\alpha\alpha\frac{1}{2})$, B = $(\bar{\alpha}\alpha\frac{1}{2})$, Λ = (00α), G = $(\frac{1}{2}-\alpha, \frac{1}{2}+\alpha, \frac{1}{2})$, H = $(\frac{1}{2}\frac{1}{2}\alpha)$, E = $(-\frac{1}{2}+\alpha, \frac{1}{2}+\alpha, \frac{1}{2})$, D = $(0\frac{1}{2}\alpha)$

36 $Cmc2_1$					
Z	G_{16}^8	$[\{\sigma_y\|000\}, \{C_{2z}\|00\frac{1}{2}\}]$	$R_9 \oplus R_9$	$R_1 \oplus R_2 \oplus R_4$	$[A,B,\Lambda] \to a$
T(1)	G_{16}^8	$[\{\sigma_y\|000\}, \{C_{2z}\|00\frac{1}{2}\}]$	$R_9 \oplus R_9$	$R_1 \oplus R_2 \oplus R_4$	$[A,G,H] \to a$
T(2)	G_{16}^8	$[\{\sigma_y\|000\}, \{C_{2z}\|00\frac{1}{2}\}]$	$R_9 \oplus R_9$	$R_1 \oplus R_2 \oplus R_4$	$[B,E,H] \to a$
37 Ccc2					
Z	G_{16}^8	$[\{C_{2z}\|000\}, \{\sigma_x\|00\frac{1}{2}\}]$	$R_9 \oplus R_9$	$R_1 \oplus R_3 \oplus R_4$	$[A,B,\Lambda] \to a$
T(1)	G_{16}^8	$[\{C_{2z}\|000\}, \{\sigma_x\|00\frac{1}{2}\}]$	$R_9 \oplus R_9$	$R_1 \oplus R_3 \oplus R_4$	$[A,G,H] \to a$
T(2)	G_{16}^8	$[\{C_{2z}\|000\}, \{\sigma_x\|00\frac{1}{2}\}]$	$R_9 \oplus R_9$	$R_1 \oplus R_3 \oplus R_4$	$[B,E,H] \to a$
63 $Cmcm^7$					
R	G_{16}^{10}	$[\{C_{2z}\|00\frac{1}{2}\}, \{E\|001\}, \{I\|000\}]$	$R_9 \oplus R_9$	$R_2 \oplus R_2 \oplus R_4$	$D \to a$
64 $Cmca^8$					
S	G_{16}^{10}	$[\{\sigma_z\|\frac{1}{2}\frac{1}{2}\frac{1}{2}\}, \{E\|010\}, \{I\|\frac{1}{2}\frac{1}{2}0\}]$	$R_9 \oplus R_9$	$R_2 \oplus R_4 \oplus R_4$	$D \to a$
66 Cccm					
Z	G_{32}^7	$[\{\sigma_x\|00\frac{1}{2}\}, \{\sigma_z\|00\frac{1}{2}\}, \{I\|00\frac{1}{2}\}]$	$R_{13} \oplus R_{14}$	$R_2 \oplus R_4 \oplus R_6$	$[A,B,\Lambda] \to a$
T(1)	G_{32}^7	$[\{\sigma_x\|00\frac{1}{2}\}, \{\sigma_z\|00\frac{1}{2}\}, \{I\|00\frac{1}{2}\}]$	$R_{13} \oplus R_{14}$	$R_2 \oplus R_4 \oplus R_6$	$[A,G,H] \to a$
T(2)	G_{32}^7	$[\{\sigma_x\|00\frac{1}{2}\}, \{\sigma_z\|00\frac{1}{2}\}, \{I\|00\frac{1}{2}\}]$	$R_{13} \oplus R_{14}$	$R_2 \oplus R_4 \oplus R_6$	$[B,E,H] \to a$
67 Cmma					
S	G_{16}^{10}	$[\{\sigma_z\|\frac{1}{2}\frac{1}{2}0\}, \{E\|010\}, \{I\|\frac{1}{2}\frac{1}{2}0\}]$	$R_9 \oplus R_9$	$R_2 \oplus R_4 \oplus R_4$	$D \to a$
R	G_{16}^{10}	$[\{\sigma_z\|\frac{1}{2}\frac{1}{2}0\}, \{E\|010\}, \{I\|\frac{1}{2}\frac{1}{2}0\}]$	$R_9 \oplus R_9$	$R_2 \oplus R_4 \oplus R_4$	$D \to a$
68 Ccca					
Z	G_{32}^7	$[\{\sigma_x\|\frac{1}{2}\frac{1}{2}\frac{1}{2}\}, \{\sigma_z\|\frac{1}{2}\frac{1}{2}\frac{1}{2}\}, \{I\|\frac{1}{2}\frac{1}{2}\frac{1}{2}\}]$	$R_{13} \oplus R_{14}$	$R_2 \oplus R_4 \oplus R_6$	$[A,B,\Lambda] \to a$
T(1)	G_{32}^7	$[\{\sigma_x\|\frac{1}{2}\frac{1}{2}\frac{1}{2}\}, \{\sigma_z\|\frac{1}{2}\frac{1}{2}\frac{1}{2}\}, \{I\|\frac{1}{2}\frac{1}{2}\frac{1}{2}\}]$	$R_{13} \oplus R_{14}$	$R_2 \oplus R_4 \oplus R_6$	$[A,G,H] \to a$
T(2)	G_{32}^7	$[\{\sigma_x\|\frac{1}{2}\frac{1}{2}\frac{1}{2}\}, \{\sigma_z\|\frac{1}{2}\frac{1}{2}\frac{1}{2}\}, \{I\|\frac{1}{2}\frac{1}{2}\frac{1}{2}\}]$	$R_{13} \oplus R_{14}$	$R_2 \oplus R_4 \oplus R_6$	$[B,E,H] \to a$
S	G_{16}^{10}	$[\{\sigma_z\|\frac{1}{2}\frac{1}{2}\frac{1}{2}\}, \{E\|010\}, \{I\|\frac{1}{2}\frac{1}{2}\frac{1}{2}\}]$	$R_9 \oplus R_9$	$R_2 \oplus R_4 \oplus R_4$	$D \to a$
R	G_{16}^{10}	$[\{\sigma_z\|\frac{1}{2}\frac{1}{2}\frac{1}{2}\}, \{E\|010\}, \{I\|\frac{1}{2}\frac{1}{2}\frac{1}{2}\}]$	$R_9 \oplus R_9$	$R_2 \oplus R_4 \oplus R_4$	$D \to a$

Table 3.4: Symmetry protected Dirac points in the Orthorhombic Base-centered Lattice

Orthorhombic Body-centered Lattice Γ_0^v

Real lattice vectors $\mathbf{t}_i$	$\{1/2(a,b,c), 1/2(-a,-b,c), 1/2(a,-b,-c)\}$
Reciprocal lattice vectors $\mathbf{g}_i$	$\{2\pi/ca(c,0,a), 2\pi/cb(0,-c,b), 2\pi/ba(b,-a,0)\}$
High symmetry points	R = $(\frac{1}{2}00)$, S = $(\frac{1}{2}0\bar{\frac{1}{2}})$, W = $(\frac{3}{4}\bar{\frac{1}{4}}\bar{\frac{1}{4}})$, T = $(\frac{1}{2}\bar{\frac{1}{2}}0)$
High symmetry lines	Q = $(\frac{1}{2}+\alpha, -\alpha, -\alpha)$, D = $(\frac{1}{2}+\alpha, -\alpha, -\alpha+\frac{1}{2})$, P = $(\frac{1}{2}+\alpha, -\frac{1}{2}+\alpha, -\alpha)$

72 Ibam					
R	G_{16}^{10}	$[\{\sigma_y\|\frac{1}{2}\frac{1}{2}0\}, \{E\|100\}, \{I\|\frac{1}{2}\frac{1}{2}0\}]$	$R_9 \oplus R_9$	$R_2 \oplus R_4 \oplus R_4$	$Q \to a$
S	G_{16}^{10}	$[\{\sigma_x\|\frac{1}{2}\frac{1}{2}0\}, \{E\|100\}, \{I\|\frac{1}{2}\frac{1}{2}0\}]$	$R_9 \oplus R_9$	$R_2 \oplus R_4 \oplus R_4$	$D \to a$
W	$G_8^5 \otimes T_4$	$[\{C_{2z}\|000\}, \{C_{2y}\|000\}]$	$R_5 \oplus R_5$	$R_2 \oplus R_3 \oplus R_4$	$[P, D, Q] \to a$
73 Ibca					
R	G_{16}^{10}	$[\{\sigma_y\|\frac{1}{2}\frac{1}{2}0\}, \{E\|100\}, \{I\|000\}]$	$R_9 \oplus R_9$	$R_2 \oplus R_4 \oplus R_4$	$Q \to a$
S	G_{16}^{10}	$[\{\sigma_x\|0\frac{1}{2}\frac{1}{2}\}, \{E\|100\}, \{I\|000\}]$	$R_9 \oplus R_9$	$R_2 \oplus R_4 \oplus R_4$	$D \to a$
T	G_{16}^{10}	$[\{\sigma_z\|\frac{1}{2}0\frac{1}{2}\}, \{E\|100\}, \{I\|000\}]$	$R_9 \oplus R_9$	$R_2 \oplus R_4 \oplus R_4$	$P \to a$
74 Imma					
T	G_{16}^{10}	$[\{\sigma_z\|0\frac{1}{2}\frac{1}{2}\}, \{E\|100\}, \{I\|\frac{1}{2}\frac{1}{2}0\}]$	$R_9 \oplus R_9$	$R_2 \oplus R_4 \oplus R_4$	$P \to a$

Table 3.5: Symmetry protected Dirac points in the Orthorhombic Body-centered Lattice

Orthorhombic Face-centered Lattice Γ_0^f

Real lattice vectors $\mathbf{t}_i$	$\{1/2(a,0,c), 1/2(0,-b,c), 1/2(a,-b,0)\}$
Reciprocal lattice vectors $\mathbf{g}_i$	$\{2\pi(1/a,1/b,1/c), 2\pi(-1/a,-1/b,1/c), 2\pi(1/a,-1/b,-1/c)\}$
	Type (1) $1/a^2 < 1/b^2 + 1/c^2, 1/b^2 < 1/a^2 + 1/c^2, 1/c^2 < 1/a^2 + 1/b^2$; (2) $1/c^2 > 1/a^2 + 1/b^2$; (3) $1/b^2 > 1/a^2 + 1/c^2$; (4) $1/a^2 > 1/b^2 + 1/c^2$
High symmetry points	Z(1,3,4) = $(\frac{1}{2}\frac{1}{2}0)$, Z(2) = $(\frac{1}{2}\bar{\frac{1}{2}}0)$, X(1,2,3) = $(\frac{1}{2}0\frac{1}{2})$, X(4) = $(\frac{1}{2}0\bar{\frac{1}{2}})$, Y(1,2,4) = $(0\frac{1}{2}\frac{1}{2})$, Y(3) = $(0\frac{\bar{1}}{2}\frac{\bar{1}}{2})$
High symmetry lines	A = $(\frac{1}{2}+\alpha, \frac{1}{2}, \alpha)$, B = $(\frac{1}{2}, \frac{\bar{1}}{2}-\alpha, -\alpha)$, $\Lambda = (\alpha\alpha 0)$, Q = $(\frac{\bar{1}}{2}+\alpha, -\frac{1}{2}+\alpha, 0)$, C = $(\alpha, -\frac{1}{2}, -\frac{1}{2}+\alpha)$, D = $(\frac{1}{2}, -\alpha, \frac{1}{2}-\alpha)$, G = $(\frac{1}{2}+\alpha, \alpha, \frac{1}{2})$, $\Sigma = (\alpha 0 \alpha)$, H = $(\alpha, -\frac{1}{2}+\alpha, -\frac{1}{2})$, U = $(\frac{1}{2}+\alpha, 0, -\frac{1}{2}+\alpha)$, $\Delta = (0\bar{\alpha}\bar{\alpha})$, R = $(1, \frac{1}{2}-\alpha, \frac{1}{2}-\alpha)$

43 Fdd2					
Z(1,3,4)	G_{16}^8	$[\{C_{2z}\|00\frac{1}{2}\}, \sigma_x\|0\frac{1}{2}0\}]$	$R_9 \oplus R_9$	$R_1 \oplus R_3 \oplus R_4$	$[A,B,\Lambda] \to a$
Z(2)	G_{16}^8	$[\{C_{2z}\|00\frac{1}{2}\}, \{\sigma_x\|0\frac{1}{2}0\}]$	$R_9 \oplus R_9$	$R_1 \oplus R_3 \oplus R_4$	$[Q,C,D] \to a$
70 Fddd					
X(1,2,3)	G_{32}^7	$[\{\sigma_z\|\frac{1}{4}\frac{1}{4}\frac{1}{4}\}, \{\sigma_x\|\frac{1}{4}\frac{1}{4}\frac{1}{4}\}, \{I\|\frac{1}{4}\frac{1}{4}\frac{1}{4}\}]$	$R_{13} \oplus R_{14}$	$R_2 \oplus R_4 \oplus R_6$	$[G,\Sigma,D] \to a$
X(4)	G_{32}^7	$[\{\sigma_z\|\frac{1}{4}\frac{1}{4}\frac{1}{4}\}, \{\sigma_x\|\frac{1}{4}\frac{1}{4}\frac{1}{4}\}, \{I\|\frac{1}{4}\frac{1}{4}\frac{1}{4}\}]$	$R_{13} \oplus R_{14}$	$R_2 \oplus R_4 \oplus R_6$	$[H,U,B] \to a$
Y(1,2,4)	G_{32}^7	$[\{\sigma_x\|\frac{1}{4}\frac{1}{4}\frac{1}{4}\}, \{\sigma_y\|\frac{1}{4}\frac{1}{4}\frac{1}{4}\}, \{I\|\frac{1}{4}\frac{1}{4}\frac{1}{4}\}]$	$R_{13} \oplus R_{14}$	$R_2 \oplus R_4 \oplus R_6$	$[H,C,\Delta] \to a$
Y(3)	G_{32}^7	$[\{\sigma_x\|\frac{1}{4}\frac{1}{4}\frac{1}{4}\}, \{\sigma_y\|\frac{1}{4}\frac{1}{4}\frac{1}{4}\}, \{I\|\frac{1}{4}\frac{1}{4}\frac{1}{4}\}]$	$R_{13} \oplus R_{14}$	$R_2 \oplus R_4 \oplus R_6$	$[G,A,R] \to a$
Z(1,3,4)	G_{32}^7	$[\{\sigma_y\|\frac{1}{4}\frac{1}{4}\frac{1}{4}\}, \{\sigma_z\|\frac{1}{4}\frac{1}{4}\frac{1}{4}\}, \{I\|\frac{1}{4}\frac{1}{4}\frac{1}{4}\}]$	$R_{13} \oplus R_{14}$	$R_2 \oplus R_4 \oplus R_6$	$[A,B,\Lambda] \to a$
Z(2)	G_{32}^7	$[\{\sigma_y\|\frac{1}{4}\frac{1}{4}\frac{1}{4}\}, \{\sigma_z\|\frac{1}{4}\frac{1}{4}\frac{1}{4}\}, \{I\|\frac{1}{4}\frac{1}{4}\frac{1}{4}\}]$	$R_{13} \oplus R_{14}$	$R_2 \oplus R_4 \oplus R_6$	$[Q,C,D] \to a$

Table 3.6: Symmetry protected Dirac points in the Orthorhombic Face-centered Lattice

Tetragonal Primitive Lattice Γ_q

Real lattice vectors $\mathbf{t}_i$	$\{(a,0,0),(0,a,0),(0,0,c)\}$
Reciprocal lattice vectors $\mathbf{g}_i$	$\{2\pi/a(1,0,0),2\pi/a(0,1,0),2\pi/c(0,0,1)\}$
High symmetry points	Z = $(00\frac{1}{2})$, R = $(0\frac{1}{2}\frac{1}{2})$ M = $(\frac{1}{2}\frac{1}{2}0)$, A = $(\frac{1}{2}\frac{1}{2}\frac{1}{2})$, X = $(0\frac{1}{2}0)$
High symmetry lines	Λ = (00α), U = $(0\alpha\frac{1}{2})$, S = $(\alpha\alpha\frac{1}{2})$, T = $(\alpha\frac{1}{2}\frac{1}{2})$, V = $(\frac{1}{2}\frac{1}{2}\alpha)$, Σ = $(\alpha\alpha0)$, W = $(0\frac{1}{2}\alpha)$, Y = $(\alpha\frac{1}{2}0)$, Δ = $(0\alpha0)$

84 $P4_2/m$					
Z	G_{32}^{12}	$[\{C_{4z}^+\|00\frac{1}{2}\},\{E\|001\},\{I\|00\frac{1}{2}\}]$	$R_{19}\oplus R_{20}$	$R_4\oplus R_7\oplus R_8$	$[U,S,\Lambda]\to a$
A	G_{32}^{12}	$[\{C_{4z}^+\|00\frac{1}{2}\},\{E\|001\},\{I\|00\frac{1}{2}\}]$	$R_{19}\oplus R_{20}$	$R_4\oplus R_7\oplus R_8$	$[T,S,V]\to a$
85 P4/n					
M	G_{32}^{12}	$[\{C_{4z}^+\|\frac{1}{2}\frac{1}{2}0\},\{E\|010\},\{I\|\frac{1}{2}\frac{1}{2}0\}]$	$R_{19}\oplus R_{20}$	$R_4\oplus R_7\oplus R_8$	$[Y,V,\Sigma]\to a$
A	G_{32}^{12}	$[\{C_{4z}^+\|\frac{1}{2}\frac{1}{2}0\},\{E\|010\},\{I\|\frac{1}{2}\frac{1}{2}0\}]$	$R_{19}\oplus R_{20}$	$R_4\oplus R_7\oplus R_8$	$[T,S,V]\to a$
R	G_{16}^{10}	$[\{\sigma_z\|\frac{1}{2}\frac{1}{2}0\},\{E\|001\},\{I\|\frac{1}{2}\frac{1}{2}0\}]$	$R_9\oplus R_9$	$R_2\oplus R_4\oplus R_4$	$[T,U,W]\to a$
X	G_{16}^{10}	$[\{\sigma_z\|\frac{1}{2}\frac{1}{2}0\},\{E\|010\},\{I\|\frac{1}{2}\frac{1}{2}0\}]$	$R_9\oplus R_9$	$R_2\oplus R_4\oplus R_4$	$[Y,\Delta,W]\to a$
86 $P4_2/n$					
M	G_{32}^{12}	$[\{C_{4z}^+\|\frac{1}{2}\frac{1}{2}\frac{1}{2}\},\{E\|010\},\{I\|\frac{1}{2}\frac{1}{2}\frac{1}{2}\}]$	$R_{19}\oplus R_{20}$	$R_4\oplus R_7\oplus R_8$	$[Y,V,\Sigma]\to a$
Z	G_{32}^{12}	$[\{C_{4z}^+\|\frac{1}{2}\frac{1}{2}\frac{1}{2}\},\{E\|001\},\{I\|\frac{1}{2}\frac{1}{2}\frac{1}{2}\}]$	$R_{19}\oplus R_{20}$	$R_4\oplus R_7\oplus R_8$	$[U,S,\Lambda]\to a$
R	G_{16}^{10}	$[\{\sigma_z\|\frac{1}{2}\frac{1}{2}\frac{1}{2}\},\{E\|001\},\{I\|\frac{1}{2}\frac{1}{2}\frac{1}{2}\}]$	$R_9\oplus R_9$	$R_2\oplus R_4\oplus R_4$	$[T,U,W]\to a$
X	G_{16}^{10}	$[\{\sigma_z\|\frac{1}{2}\frac{1}{2}\frac{1}{2}\},\{E\|010\},\{I\|\frac{1}{2}\frac{1}{2}\frac{1}{2}\}]$	$R_9\oplus R_9$	$R_2\oplus R_4\oplus R_4$	$[Y,\Delta,W]\to a$
90 $P42_12$					
M	G_{32}^{11}	$[\{C_{4z}^+\|000\},\{C_{2x}\|\frac{1}{2}\frac{1}{2}0\}]$	$R_6\oplus R_7$	$R_2\oplus R_5$	$[Y,V,\Sigma]\to a$
A	G_{32}^{11}	$[\{C_{4z}^+\|000\},\{C_{2x}\|\frac{1}{2}\frac{1}{2}0\}]$	$R_6\oplus R_7$	$R_2\oplus R_5$	$[T,S,V]\to a$
92 $P4_12_12$					
M	G_{32}^{11}	$[\{C_{4z}^+\|00\frac{1}{4}\},\{C_{2x}\|\frac{1}{2}\frac{1}{2}0\}]$	$R_6\oplus R_7$	$R_2\oplus R_5$	$[Y,V,\Sigma]\to a$
A	G_{32}^{11}	$[\{C_{4z}^+\|00\frac{1}{4}\},\{C_{2b}\|\frac{1}{2}\frac{1}{2}\frac{3}{4}\}]$	$R_{12}\oplus R_{12}$	$R_2\oplus R_5$	$[T,S,V]\to a$
R	G_{16}^{8}	$[\{C_{2x}\|\frac{1}{2}\frac{1}{2}0\},\{C_{2y}\|\frac{1}{2}\frac{1}{2}\frac{1}{2}\}]$	$R_9\oplus R_9$	$R_2\oplus R_3\oplus R_4$	$[T,U,W]\to a$
94 $P4_22_12$					
M	G_{32}^{11}	$[\{C_{4z}^+\|00\frac{1}{2}\},\{C_{2x}\|\frac{1}{2}\frac{1}{2}0\}]$	$R_6\oplus R_7$	$R_2\oplus R_5$	$[Y,V,\Sigma]\to a$
A	G_{32}^{11}	$[\{C_{4z}^+\|00\frac{1}{2}\},\{C_{2x}\|\frac{1}{2}\frac{1}{2}0\}]$	$R_6\oplus R_7$	$R_2\oplus R_5$	$[T,S,V]\to a$

Table 3.7: Symmetry protected Dirac points in the Tetragonal Primitive Lattice

96 $P4_32_12$

M	G_{32}^{11}	$[\{C_{4z}^{+}\|00\frac{3}{4}\},\{C_{2x}\|\frac{1}{2}\frac{1}{2}0\}]$	$R_6 \oplus R_7$	$R_2 \oplus R_5$	$[Y, V, \Sigma] \to a$
A	G_{32}^{11}	$[\{C_{4z}^{+}\|00\frac{3}{4}\},\{C_{2b}\|\frac{1}{2}\frac{1}{2}\frac{1}{4}\}]$	$R_{12} \oplus R_{12}$	$R_2 \oplus R_5$	$[T, S, V] \to a$
R	G_{16}^{8}	$[\{C_{2x}\|\frac{1}{2}\frac{1}{2}0\},\{C_{2y}\|\frac{1}{2}\frac{1}{2}\frac{1}{2}\}]$	$R_9 \oplus R_9$	$R_2 \oplus R_3 \oplus R_4$	$[T, U, W] \to a$

100 P4bm

M	G_{32}^{11}	$[\{C_{4z}^{+}\|000\},\{\sigma_x\|\frac{1}{2}\frac{1}{2}0\}]$	$R_6 \oplus R_7$	$R_1 \oplus R_5$	$[Y, V, \Sigma] \to a$
A	G_{32}^{11}	$[\{C_{4z}^{+}\|000\},\{\sigma_x\|\frac{1}{2}\frac{1}{2}0\}]$	$R_6 \oplus R_7$	$R_1 \oplus R_5$	$[T, S, V] \to a$

101 $P4_2cm$

Z	G_{32}^{11}	$[\{C_{4z}^{+}\|00\frac{1}{2}\},\{\sigma_x\|00\frac{1}{2}\}]$	$R_6 \oplus R_7$	$R_1 \oplus R_5$	$[U, S, \Lambda] \to a$
A	G_{32}^{11}	$[\{C_{4z}^{+}\|00\frac{1}{2}\},\{\sigma_x\|00\frac{1}{2}\}]$	$R_6 \oplus R_7$	$R_1 \oplus R_5$	$[T, S, V] \to a$
R	G_{16}^{8}	$[\{C_{2z}\|000\},\{\sigma_x\|00\frac{1}{2}\}]$	$R_9 \oplus R_9$	$R_1 \oplus R_3 \oplus R_4$	$[T, U, W] \to a$

102 $P4_2nm$

M	G_{32}^{11}	$[\{C_{4z}^{+}\|00\frac{1}{2}\},\{\sigma_x\|\frac{1}{2}\frac{1}{2}\frac{1}{2}\}]$	$R_6 \oplus R_7$	$R_1 \oplus R_5$	$[Y, V, \Sigma] \to a$
Z	G_{32}^{11}	$[\{C_{4z}^{+}\|00\frac{1}{2}\},\{\sigma_x\|\frac{1}{2}\frac{1}{2}\frac{1}{2}\}]$	$R_6 \oplus R_7$	$R_1 \oplus R_5$	$[U, S, \Lambda] \to a$

103 P4cc

Z	G_{32}^{10}	$[\{C_{4z}^{+}\|000\},\{\sigma_{db}\|00\frac{1}{2}\}]$	$R_6 \oplus R_6$, $R_7 \oplus R_7$	$R_1 \oplus R_5$	$[U, S, \Lambda] \to a$
A	G_{32}^{10}	$[\{C_{4z}^{+}\|000\},\{\sigma_{db}\|00\frac{1}{2}\}]$	$R_6 \oplus R_6$, $R_7 \oplus R_7$	$R_1 \oplus R_5$	$[T, S, V] \to a$
R	G_{16}^{8}	$[\{C_{2z}\|000\},\{\sigma_x\|00\frac{1}{2}\}]$	$R_9 \oplus R_9$	$R_1 \oplus R_3 \oplus R_4$	$[T, U, W] \to a$

104 P4nc

M	G_{32}^{11}	$[\{C_{4z}^{+}\|000\},\{\sigma_x\|\frac{1}{2}\frac{1}{2}\frac{1}{2}\}]$	$R_6 \oplus R_7$	$R_1 \oplus R_5$	$[Y, V] \to a, \Sigma \to b$
Z	G_{32}^{10}	$[\{C_{4z}^{+}\|000\},\{\sigma_{db}\|\frac{1}{2}\frac{1}{2}\frac{1}{2}\}]$	$R_6 \oplus R_6$, $R_7 \oplus R_7$	$R_1 \oplus R_5$	$[U, S, \Lambda] \to a$
A	G_{32}^{11}	$[\{C_{4z}^{+}\|000\},\{\sigma_{db}\|\frac{1}{2}\frac{1}{2}\frac{1}{2}\}]$	$R_6 \oplus R_7$	$R_1 \oplus R_5$	$[S, V] \to a, T \to b$

105 $P4_2mc$

Z	G_{32}^{11}	$[\{C_{4z}^{+}\|00\frac{1}{2}\},\{\sigma_{db}\|00\frac{1}{2}\}]$	$R_6 \oplus R_7$	$R_1 \oplus R_5$	$[S, \Lambda] \to a, U \to b$
A	G_{32}^{11}	$[\{C_{4z}^{+}\|00\frac{1}{2}\},\{\sigma_{db}\|00\frac{1}{2}\}]$	$R_6 \oplus R_7$	$R_1 \oplus R_5$	$[S, V] \to a, T \to b$

106 $P4_2bc$

M	G_{32}^{11}	$[\{C_{4z}^{+}\|00\frac{1}{2}\},\{\sigma_x\|\frac{1}{2}\frac{1}{2}0\}]$	$R_6 \oplus R_7$	$R_1 \oplus R_5$	$[Y, V] \to a, \Sigma \to b$
Z	G_{32}^{11}	$[\{C_{4z}^{+}\|00\frac{1}{2}\},\{\sigma_{db}\|\frac{1}{2}\frac{1}{2}\frac{1}{2}\}]$	$R_6 \oplus R_7$	$R_1 \oplus R_5$	$[S, \Lambda] \to a, U \to b$
A	G_{32}^{10}	$[\{C_{4z}^{+}\|00\frac{1}{2}\},\{\sigma_{db}\|\frac{1}{2}\frac{1}{2}\frac{1}{2}\}]$	$R_6 \oplus R_6$, $R_7 \oplus R_7$	$R_1 \oplus R_5$	$[T, S, V] \to a$

Symmetry protected Dirac points in the Tetragonal Primitive Lattice (ii) of (vi)

112 $P\bar{4}2c$					
Z	G_{32}^{11}	$[\{S_{4z}^{+}\|000\}, \{\sigma_{db}\|00\frac{1}{2}\}]$	$R_6 \oplus R_7$	$R_3 \oplus R_5$	$[S, \Lambda] \to a, U \to b$
A	G_{32}^{11}	$[\{S_{4z}^{+}\|000\}, \{\sigma_{db}\|00\frac{1}{2}\}]$	$R_6 \oplus R_7$	$R_3 \oplus R_5$	$[S, V] \to a, T \to b$
114 $P\bar{4}2_1c$[9]					
Z	G_{32}^{11}	$[\{S_{4z}^{+}\|000\}, \{\sigma_{db}\|\frac{1}{2}\frac{1}{2}\frac{1}{2}\}]$	$R_6 \oplus R_7$	$R_3 \oplus R_5$	$[S, \Lambda] \to a, U \to b$
116 $P\bar{4}c2$					
Z	G_{32}^{11}	$[\{S_{4z}^{+}\|000\}, \{\sigma_{x}\|00\frac{1}{2}\}]$	$R_6 \oplus R_7$	$R_3 \oplus R_5$	$[U, \Lambda] \to a, S \to b$
A	G_{32}^{11}	$[\{S_{4z}^{+}\|000\}, \{\sigma_{x}\|00\frac{1}{2}\}]$	$R_6 \oplus R_7$	$R_3 \oplus R_5$	$[T, V] \to a, S \to b$
R	G_{16}^{8}	$[\{C_{2z}\|000\}, \{\sigma_{x}\|00\frac{1}{2}\}]$	$R_9 \oplus R_9$	$R_1 \oplus R_3 \oplus R_4$	$[T, U, W] \to a$
117 $P\bar{4}b2$					
M	G_{32}^{11}	$[\{S_{4z}^{+}\|000\}, \{\sigma_{x}\|\frac{1}{2}\frac{1}{2}0\}]$	$R_6 \oplus R_7$	$R_3 \oplus R_5$	$[Y, V] \to a, \Sigma \to b$
A	G_{32}^{11}	$[\{S_{4z}^{+}\|000\}, \{\sigma_{x}\|\frac{1}{2}\frac{1}{2}0\}]$	$R_6 \oplus R_7$	$R_3 \oplus R_5$	$[T, V] \to a, S \to b$
118 $P\bar{4}n2$					
M	G_{32}^{11}	$[\{S_{4z}^{+}\|000\}, \{\sigma_{x}\|\frac{1}{2}\frac{1}{2}\frac{1}{2}\}]$	$R_6 \oplus R_7$	$R_3 \oplus R_5$	$[Y, V] \to a, \Sigma \to b$
Z	G_{32}^{11}	$[\{S_{4z}^{+}\|000\}, \{\sigma_{x}\|\frac{1}{2}\frac{1}{2}\frac{1}{2}\}]$	$R_6 \oplus R_7$	$R_3 \oplus R_5$	$[U, \Lambda] \to a, S \to b$
124 P4/mcc					
Z	G_{64}^{1}	$[\{I\|00\frac{1}{2}\}, \{\sigma_{db}\|00\frac{1}{2}\}, \{C_{4z}^{+}\|000\}]$	$R_{19} \oplus R_{20}$, $R_{21} \oplus R_{22}$	$R_6 \oplus R_{14}$	$[U, S, \Lambda] \to a$
A	G_{64}^{1}	$[\{I\|00\frac{1}{2}\}, \{\sigma_{db}\|00\frac{1}{2}\}, \{C_{4z}^{+}\|000\}]$	$R_{19} \oplus R_{20}$, $R_{21} \oplus R_{22}$	$R_6 \oplus R_{14}$	$[T, S, V] \to a$
R	G_{32}^{7}	$[\{\sigma_{x}\|00\frac{1}{2}\}, \{\sigma_{z}\|00\frac{1}{2}\}, \{I\|00\frac{1}{2}\}]$	$R_{13} \oplus R_{14}$	$R_2 \oplus R_4 \oplus R_6$	$[T, U, W] \to a$

Symmetry protected Dirac points in the Tetragonal Primitive Lattice (iii) of (vi)

125 P4/nbm

M	G_{64}^{2}	$[\{C_{4z}^{+}\|\frac{1}{2}\frac{1}{2}0\}$, $\{\sigma_x\|\frac{1}{2}\frac{1}{2}0\}$, $\{C_{2x}\|000\}]$	R_{19}	$R_8 \oplus R_{13}$	$[Y, V, \Sigma] \to a$
A	G_{64}^{2}	$[\{C_{4z}^{+}\|\frac{1}{2}\frac{1}{2}0\}$, $\{\sigma_x\|\frac{1}{2}\frac{1}{2}0\}$, $\{C_{2x}\|000\}]$	R_{19}	$R_8 \oplus R_{13}$	$[T, S, V] \to a$
R	G_{32}^{7}	$[\{\sigma_x\|\frac{1}{2}\frac{1}{2}0\}, \{\sigma_y\|\frac{1}{2}\frac{1}{2}0\}$, $\{I\|\frac{1}{2}\frac{1}{2}0\}]$	$R_{13} \oplus R_{14}$	$R_2 \oplus R_4 \oplus R_6$	$[T, U, W] \to a$
X	G_{32}^{7}	$[\{\sigma_x\|\frac{1}{2}\frac{1}{2}0\}, \{\sigma_y\|\frac{1}{2}\frac{1}{2}0\}$, $\{I\|\frac{1}{2}\frac{1}{2}0\}]$	$R_{13} \oplus R_{14}$	$R_2 \oplus R_4 \oplus R_6$	$[Y, \Delta, W] \to a$

126 P4/nnc

M	G_{64}^{2}	$[\{C_{4z}^{+}\|\frac{1}{2}\frac{1}{2}0\}$, $\{\sigma_x\|\frac{1}{2}\frac{1}{2}\frac{1}{2}\}$, $\{C_{2x}\|000\}]$	R_{19}	$R_8 \oplus R_{13}$	$[Y, V, \Sigma] \to a$
A	G_{64}^{2}	$[\{C_{4z}^{+}\|\frac{1}{2}\frac{1}{2}0\}$, $\{\sigma_{db}\|00\frac{1}{2}\}$, $\{C_{2b}\|\frac{1}{2}\frac{1}{2}0\}]$	R_{19}	$R_8 \oplus R_{13}$	$[T, S, V] \to a$
Z	G_{64}^{1}	$[\{I\|\frac{1}{2}\frac{1}{2}\frac{1}{2}\}, \{\sigma_{db}\|00\frac{1}{2}\}$, $\{C_{4z}^{+}\|\frac{1}{2}\frac{1}{2}0\}]$	$R_{19} \oplus R_{20}$, $R_{21} \oplus R_{22}$	$R_6 \oplus R_{14}$	$[U, S, \Lambda] \to a$
R	G_{32}^{7}	$[\{\sigma_y\|\frac{1}{2}\frac{1}{2}\frac{1}{2}\}$, $\{\sigma_x\|\frac{1}{2}\frac{1}{2}\frac{1}{2}\}, \{I\|\frac{1}{2}\frac{1}{2}\frac{1}{2}\}]$	$R_{13} \oplus R_{14}$	$R_2 \oplus R_4 \oplus R_6$	$[T, U, W] \to a$
X	G_{32}^{7}	$[\{\sigma_x\|\frac{1}{2}\frac{1}{2}\frac{1}{2}\}$, $\{\sigma_y\|\frac{1}{2}\frac{1}{2}\frac{1}{2}\}, \{I\|\frac{1}{2}\frac{1}{2}\frac{1}{2}\}]$	$R_{13} \oplus R_{14}$	$R_2 \oplus R_4 \oplus R_6$	$[Y, \Delta, W] \to a$

128 P4/mnc[10]

Z	G_{64}^{1}	$[\{I\|00\frac{1}{2}\}, \{\sigma_{db}\|00\frac{1}{2}\}$, $\{C_{4z}^{+}\|\frac{1}{2}\frac{1}{2}0\}]$	$R_{19} \oplus R_{20}$, $R_{21} \oplus R_{22}$	$R_6 \oplus R_{14}$	$[U, S, \Lambda] \to a$

130 P4/ncc[11]

Z	G_{64}^{1}	$[\{I\|\frac{1}{2}\frac{1}{2}\frac{1}{2}\}, \{\sigma_{db}\|00\frac{1}{2}\}$, $\{C_{4z}^{+}\|000\}]$	$R_{19} \oplus R_{20}$, $R_{21} \oplus R_{22}$	$R_6 \oplus R_{14}$	$[U, S, \Lambda] \to a$

131 $P4_2/mmc$

Z	G_{64}^{2}	$[\{C_{4z}^{+}\|00\frac{1}{2}\}$, $\{\sigma_{db}\|00\frac{1}{2}\}$, $\{C_{2b}\|00\frac{1}{2}\}]$	R_{19}	$R_8 \oplus R_{13}$	$[U, S, \Lambda] \to a$
A	G_{64}^{2}	$[\{C_{4z}^{+}\|00\frac{1}{2}\}$, $\{\sigma_{db}\|00\frac{1}{2}\}$, $\{C_{2b}\|00\frac{1}{2}\}]$	R_{19}	$R_8 \oplus R_{13}$	$[T, S, V] \to a$

Symmetry protected Dirac points in the Tetragonal Primitive Lattice (iv) of (vi)

132 $P4_2/mcm$

Z	G_{64}^2	$[\{C_{4z}^+\|00\frac{1}{2}\}$, $\{\sigma_x\|00\frac{1}{2}\}$, $\{C_{2x}\|000\}]$	R_{19}	$R_8 \oplus R_{13}$	$[U, S, \Lambda] \to a$
A	G_{64}^2	$[\{C_{4z}^+\|00\frac{1}{2}\}$, $\{\sigma_x\|00\frac{1}{2}\}$, $\{C_{2x}\|000\}]$	R_{19}	$R_8 \oplus R_{13}$	$[T, S, V] \to a$
R	G_{32}^7	$[\{\sigma_x\|00\frac{1}{2}\}$, $\{\sigma_y\|00\frac{1}{2}\}$, $\{I\|00\frac{1}{2}\}]$	$R_{13} \oplus R_{14}$	$R_2 \oplus R_4 \oplus R_6$	$[T, U, W] \to a$

133 $P4_2/nbc$

M	G_{64}^2	$[\{C_{4z}^+\|\frac{1}{2}\frac{1}{2}\frac{1}{2}\}$, $\{\sigma_x\|\frac{1}{2}\frac{1}{2}0\}$, $\{C_{2x}\|000\}]$	R_{19}	$R_8 \oplus R_{13}$	$[Y, V, \Sigma] \to a$
Z	G_{64}^2	$[\{C_{4z}^+\|\frac{1}{2}\frac{1}{2}\frac{1}{2}\}$, $\{\sigma_{db}\|00\frac{1}{2}\}$, $\{C_{2b}\|\frac{1}{2}\frac{1}{2}\frac{1}{2}\}]$	R_{19}	$R_8 \oplus R_{13}$	$[U, S, \Lambda] \to a$
A	G_{64}^1	$[\{I\|\frac{1}{2}\frac{1}{2}0\}$, $\{\sigma_x\|\frac{1}{2}\frac{1}{2}0\}$, $\{C_{4z}^+\|\frac{1}{2}\frac{1}{2}\frac{1}{2}\}]$	$R_{19} \oplus R_{20}$, $R_{21} \oplus R_{22}$	$R_6 \oplus R_{14}$	$[T, S, V] \to a$
R	G_{32}^7	$[\{\sigma_x\|\frac{1}{2}\frac{1}{2}0\}$, $\{\sigma_y\|\frac{1}{2}\frac{1}{2}0\}$, $\{I\|\frac{1}{2}\frac{1}{2}0\}]$	$R_{13} \oplus R_{14}$	$R_2 \oplus R_4 \oplus R_6$	$[T, U, W] \to a$
X	G_{32}^7	$[\{\sigma_x\|\frac{1}{2}\frac{1}{2}0\}$, $\{\sigma_y\|\frac{1}{2}\frac{1}{2}0\}$, $\{I\|\frac{1}{2}\frac{1}{2}0\}]$	$R_{13} \oplus R_{14}$	$R_2 \oplus R_4 \oplus R_6$	$[Y, \Delta, W] \to a$

134 $P4_2/nnm$

M	G_{64}^2	$[\{C_{4z}^+\|\frac{1}{2}\frac{1}{2}\frac{1}{2}\}$, $\{\sigma_x\|\frac{1}{2}\frac{1}{2}\frac{1}{2}\}$, $\{C_{2x}\|000\}]$	R_{19}	$R_8 \oplus R_{13}$	$[Y, V, \Sigma] \to a$
Z	G_{64}^2	$[\{C_{4z}^+\|\frac{1}{2}\frac{1}{2}\frac{1}{2}\}$, $\{\sigma_x\|\frac{1}{2}\frac{1}{2}\frac{1}{2}\}$, $\{C_{2x}\|000\}]$	R_{19}	$R_8 \oplus R_{13}$	$[U, S, \Lambda] \to a$
R	G_{32}^7	$[\{\sigma_y\|\frac{1}{2}\frac{1}{2}\frac{1}{2}\}$, $\{\sigma_x\|\frac{1}{2}\frac{1}{2}\frac{1}{2}\}$, $\{I\|\frac{1}{2}\frac{1}{2}\frac{1}{2}\}]$	$R_{13} \oplus R_{14}$	$R_2 \oplus R_4 \oplus R_6$	$[T, U, W] \to a$
X	G_{32}^7	$[\{\sigma_x\|\frac{1}{2}\frac{1}{2}\frac{1}{2}\}$, $\{\sigma_y\|\frac{1}{2}\frac{1}{2}\frac{1}{2}\}$, $\{I\|\frac{1}{2}\frac{1}{2}\frac{1}{2}\}]$	$R_{13} \oplus R_{14}$	$R_2 \oplus R_4 \oplus R_6$	$[Y, \Delta, W] \to a$

135 $P4_2/mbc$[12]

Z	G_{64}^2	$[\{C_{4z}^+\|\frac{1}{2}\frac{1}{2}\frac{1}{2}\}$, $\{\sigma_{db}\|00\frac{1}{2}\}$, $\{C_{2b}\|00\frac{1}{2}\}]$	R_{19}	$R_8 \oplus R_{13}$	$[U, S, \Lambda] \to a$

Symmetry protected Dirac points in the Tetragonal Primitive Lattice (v) of (vi)

136 $P4_2/mnm^{13}$

Z	G_{64}^2	$[\{C_{4z}^+\|\frac{1}{2}\frac{1}{2}\frac{1}{2}\}, \{\sigma_x\|\frac{1}{2}\frac{1}{2}\frac{1}{2}\}, \{C_{2x}\|\frac{1}{2}\frac{1}{2}0\}]$	R_{19}	$R_8 \oplus R_{13}$	$[U, S, \Lambda] \to a$

137 $P4_2/nmc^{14}$

Z	G_{64}^2	$[\{C_{4z}^+\|00\frac{1}{2}\}, \{\sigma_{db}\|00\frac{1}{2}\}, \{C_{2b}\|\frac{1}{2}\frac{1}{2}\frac{1}{2}\}]$	R_{19}	$R_8 \oplus R_{13}$	$[U, S, \Lambda] \to a$

138 $P4_2/ncm^{15}$

Z	G_{64}^2	$[\{C_{4z}^+\|00\frac{1}{2}\}, \{\sigma_x\|00\frac{1}{2}\}, \{C_{2x}\|\frac{1}{2}\frac{1}{2}0\}]$	R_{19}	$R_8 \oplus R_{13}$	$[U, S, \Lambda] \to a$

Symmetry protected Dirac points in the Tetragonal Primitive Lattice (vi) of (vi)

Tetragonal Body-centered Lattice Γ_q^v

Real lattice vectors $\mathbf{t}_i$	$\{1/2(-a,a,c), 1/2(a,-a,c), 1/2(a,a,-c)\}$ Type(1) a > c; (2) c > a
Reciprocal lattice vectors $\mathbf{g}_i$	$\{2\pi/ca(0,c,a), 2\pi/ca(c,0,a), 2\pi/a(1,1,0)\}$
High symmetry points	X = $(00\frac{1}{2})$, Z(1) = $(\bar{\frac{1}{2}}\frac{1}{2}\frac{1}{2})$ Z(2) = $(\frac{1}{2}\frac{1}{2}\frac{1}{2})$, P = $(\frac{1}{4}\frac{1}{4}\frac{1}{4})$, N = $(0\frac{1}{2}0)$, X = $(00\frac{1}{2})$
High symmetry lines	Δ = (00α), W = $(\alpha,\alpha,\frac{1}{2}-\alpha)$, Y = $(\bar{\alpha}\alpha\frac{1}{2})$, Σ = $(\bar{\alpha}\alpha\alpha)$, V = $(-\frac{1}{2}+\alpha,\frac{1}{2}+\alpha,\frac{1}{2}-\alpha)$, Λ = $(\alpha\alpha\bar{\alpha})$, U = $(\frac{1}{2},\frac{1}{2},-\frac{1}{2}+\alpha)$, F = $(\frac{1}{2}-\alpha,\frac{1}{2}+\alpha,-\frac{1}{2}+\alpha)$, Q = $(\alpha,\frac{1}{2}-\alpha,\alpha)$

88 $I4_1/a$					
X	G_{16}^{10}	$[\{\sigma_z\|\frac{3}{4}\frac{1}{4}\frac{1}{2}\}, \{E\|001\}, \{I\|\frac{3}{4}\frac{1}{4}\frac{1}{2}\}]$	$R_9 \oplus R_9$	$R_2 \oplus R_4 \oplus R_4$	$[\Delta, W, Y] \to a$
Z(1)	G_{32}^{12}	$[\{C_{4z}^+\|\frac{3}{4}\frac{1}{4}\frac{1}{2}\}, \{E\|001\}, \{I\|\frac{3}{4}\frac{1}{4}\frac{1}{2}\}]$	$R_{19} \oplus R_{20}$	$R_4 \oplus R_7 \oplus R_8$	$[\Sigma, V, Y] \to a$
Z(2)	G_{32}^{12}	$[\{C_{4z}^+\|\frac{3}{4}\frac{1}{4}\frac{1}{2}\}, \{E\|001\}, \{I\|\frac{3}{4}\frac{1}{4}\frac{1}{2}\}]$	$R_{19} \oplus R_{20}$	$R_4 \oplus R_7 \oplus R_8$	$[\Lambda, U, F] \to a$
108 I4cm					
P	$G_8^5 \otimes T_4$	$[\{C_{2z}\|000\}, \{\sigma_{db}\|\frac{3}{2}\frac{1}{2}0\}]$	$R_5 \oplus R_5$	$R_1 \oplus R_3 \oplus R_4$	$[Q, W] \to a$
109 $I4_1md$					
Z(1)	G_{32}^{11}	$[\{C_{4z}^+\|\frac{3}{4}\frac{1}{4}\frac{1}{2}\}, \{\sigma_{db}\|\frac{3}{4}\frac{1}{4}\frac{1}{2}\}]$	$R_6 \oplus R_7$	$R_1 \oplus R_5$	$[V, Y] \to a, \Sigma \to b$
Z(2)	G_{32}^{11}	$[\{C_{4z}^+\|\frac{3}{4}\frac{1}{4}\frac{1}{2}\}, \{\sigma_{db}\|\frac{3}{4}\frac{1}{4}\frac{1}{2}\}]$	$R_6 \oplus R_7$	$R_1 \oplus R_5$	$[\Lambda, U] \to a, F \to b$
110 $I4_1cd$					
Z(1)	G_{32}^{11}	$[\{C_{4z}^+\|\frac{3}{4}\frac{1}{4}\frac{1}{2}\}, \{\sigma_{db}\|\frac{1}{4}\frac{3}{4}\frac{1}{2}\}]$	$R_6 \oplus R_7$	$R_1 \oplus R_5$	$[V, Y] \to a, \Sigma \to b$
Z(2)	G_{32}^{11}	$[\{C_{4z}^+\|\frac{3}{4}\frac{1}{4}\frac{1}{2}\}, \{\sigma_{db}\|\frac{1}{4}\frac{3}{4}\frac{1}{2}\}]$	$R_6 \oplus R_7$	$R_1 \oplus R_5$	$[\Lambda, U] \to a, F \to b$
122 $I\bar{4}2d$					
Z(1)	G_{32}^{11}	$[\{S_{4z}^+\|000\}, \{\sigma_{db}\|\frac{1}{4}\frac{3}{4}\frac{1}{2}\}]$	$R_6 \oplus R_7$	$R_3 \oplus R_5$	$[V, Y] \to a, \Sigma \to b$
Z(2)	G_{32}^{11}	$[\{S_{4z}^+\|000\}, \{\sigma_{db}\|\frac{1}{4}\frac{3}{4}\frac{1}{2}\}]$	$R_6 \oplus R_7$	$R_3 \oplus R_5$	$[\Lambda, U] \to a, F \to b$

Table 3.8: Symmetry protected Dirac points in the Tetragonal Body-centered Lattice

140 I4/mcm					
N	G_{16}^{10}	$[\{\sigma_y\|\frac{1}{2}\frac{1}{2}0\}$, $\{E\|010\}$, $\{I\|\frac{1}{2}\frac{1}{2}0\}]$	$R_9 \oplus R_9$	$R_2 \oplus R_4 \oplus R_4$	$Q \to a$
P	$G_{16}^{14} \otimes T_4$	$[\{S_{4z}^+\|000\}$, $\{C_{2x}\|000\}]$	$R_6 \oplus R_7$	$R_4 \oplus R_5$	$[Q, W] \to a$
141 $I4_1$amd					
X	G_{32}^7	$[\{\sigma_{db}\|00\frac{1}{2}\}$, $\{\sigma_{da}\|0\frac{1}{2}0\}$, $\{I\|\frac{1}{2}\frac{1}{2}0\}]$	$R_{13} \oplus R_{14}$	$R_2 \oplus R_4 \oplus R_6$	$[\Delta, W, Y] \to a$
Z(1)	G_{64}^2	$[\{C_{4z}^+\|0\frac{1}{2}0\}$, $\{\sigma_{db}\|00\frac{1}{2}\}$, $\{C_{2b}\|\frac{1}{2}\frac{1}{2}\frac{1}{2}\}]$	R_{19}	$R_8 \oplus R_{13}$	$[V, Y, \Sigma] \to a$
Z(2)	G_{64}^2	$[\{C_{4z}^+\|0\frac{1}{2}0\}$, $\{\sigma_{db}\|00\frac{1}{2}\}$, $\{C_{2b}\|\frac{1}{2}\frac{1}{2}\frac{1}{2}\}]$	R_{19}	$R_8 \oplus R_{13}$	$[\Lambda, U, F] \to a$
142 $I4_1$acd					
N	G_{16}^{10}	$[\{C_{2y}\|0\frac{1}{2}\frac{1}{2}\}$, $\{E\|010\}, \{I\|000\}]$	$R_{10} \oplus R_{10}$	$R_2 \oplus R_2 \oplus R_4$	$Q \to a$
X	G_{32}^7	$[\{\sigma_z\|\frac{1}{2}0\frac{1}{2}\}$, $\{\sigma_{da}\|0\frac{1}{2}0\}$, $\{I\|000\}]$	$R_{13} \oplus R_{14}$	$R_2 \oplus R_4 \oplus R_6$	$[\Delta, W, Y] \to a$
Z(1)	G_{64}^2	$[\{C_{4z}^+\|\frac{1}{2}00\}$, $\{\sigma_{db}\|00\frac{1}{2}\}$, $\{C_{2b}\|00\frac{1}{2}\}]$	R_{19}	$R_8 \oplus R_{13}$	$[V, Y, \Sigma] \to a$
Z(2)	G_{64}^2	$[\{C_{4z}^+\|\frac{1}{2}00\}$, $\{\sigma_{db}\|00\frac{1}{2}\}$, $\{C_{2b}\|00\frac{1}{2}\}]$	R_{19}	$R_8 \oplus R_{13}$	$[\Lambda, U, F] \to a$
P	G_{64}^3	$[\{S_{4z}^+\|\frac{1}{2}\frac{1}{2}\frac{1}{2}\}$, $\{\sigma_{db}\|10\frac{1}{2}\}]$	$R_{19} \oplus R_{19}$	$R_6 \oplus R_{17}$	$[Q, W] \to a$

Symmetry protected Dirac points in the Tetragonal Body-centered Lattice (ii) of (ii)

Trigonal Primitive Lattice Γ_{rh}

Real lattice vectors $\mathbf{t}_i$	$\{(0,-a,c), 1/2(a\sqrt{3},a,2c), 1/2(-a\sqrt{3},a,2c)\}$
Reciprocal lattice vectors $\mathbf{g}_i$	$\{2\pi(0,-2/3a,1/3c), 2\pi(1/\sqrt{3}a,1/3a,1/3c),$ $2\pi(-1/\sqrt{3}a,1/3a,1/3c)\}$
High symmetry points	$\mathrm{L} = (0\frac{1}{2}0)$
High symmetry lines	$\mathrm{Y} = (\alpha\frac{1}{2}\bar{\alpha})$

167 $\mathrm{R}\bar{3}\mathrm{c}^{16}$

L	G_{16}^{10}	$[\{\mathrm{C}'_{22}\|\frac{1}{2}\frac{1}{2}\frac{1}{2}\}, \{\mathrm{E}\|010\}, \{\mathrm{I}\|000\}]$	$\mathrm{R}_{10} \oplus \mathrm{R}_{10}$	$\mathrm{R}_2 \oplus \mathrm{R}_2 \oplus \mathrm{R}_4$	$\mathrm{Y} \to \mathrm{a}$

Table 3.9: Symmetry protected Dirac points in the Trigonal Primitive Lattice

Hexagonal Primitive Lattice Γ_h

Real lattice vectors $\mathbf{t}_i$	$\{(0,-a,0), 1/2(a\sqrt{3},a,0), (0,0,c)\}$
Reciprocal lattice vectors $\mathbf{g}_i$	$\{2\pi/a(1/\sqrt{3},-1,0), 2\pi/a(2/\sqrt{3},0,0), 2\pi/c(0,0,1)\}$
High symmetry points	L $= (0\frac{1}{2}\frac{1}{2})$, H $= (\frac{\bar{1}}{3}\frac{2}{3}\frac{1}{2})$
High symmetry lines	U $= (0\frac{1}{2}\alpha)$, S $= (2\bar{\alpha}, \frac{1}{2}+\alpha, \frac{1}{2})$, R $= (0\alpha\frac{1}{2})$], P $= (\frac{\bar{1}}{3}\frac{2}{3}\alpha)$, S $= (\bar{\alpha}, 2\alpha, \frac{1}{2})$

163 $P\bar{3}1c^{17}$					
L	G_{16}^{10}	$[\{C'_{21}\|00\frac{1}{2}\}, \{E\|001\}, \{I\|000\}]$	$R_{10}\oplus R_{10}$	$R_2\oplus R_2\oplus R_4$	$[U,S',R]\to a$
165 $P\bar{3}c1^{18}$					
L	G_{16}^{10}	$[\{C''_{21}\|00\frac{1}{2}\}, \{E\|001\}, \{I\|000\}]$	$R_{10}\oplus R_{10}$	$R_2\oplus R_2\oplus R_4$	$[U,S',R]\to a$
H	$G_{12}^{4}\otimes T_3\otimes T_2$	$[\{C_3^+\|000\}, \{C''_{21}\|00\frac{1}{2}\}]$	$R_6\oplus R_6$	$R_2\oplus R_5$	$[P,S',S]\to a$
176 $P6_3m^{19}$					
L	G_{16}^{10}	$[\{\sigma_h\|000\}, \{E\|001\}, \{I\|00\frac{1}{2}\}]$	$R_{10}\oplus R_{10}$	$R_2\oplus R_4\oplus R_4$	$[U,S',R]\to a$
184 $P6cc^{20}$					
L	G_{16}^{8}	$[\{C_2\|000\}, \{\sigma_{v1}\|00\frac{1}{2}\}]$	$R_9\oplus R_9$	$R_1\oplus R_3\oplus R_4$	$[U,S',R]\to a$
H	$G_{12}^{4}\otimes T_3\otimes T_2$	$[\{C_3^+\|001\}, \{\sigma_{d1}\|00\frac{1}{2}\}]$	$R_5\oplus R_5$	$R_1\oplus R_5$	$[S',S]\to a, P\to d$
185 $P6_3cm^{21}$					
L	G_{16}^{8}	$[\{\sigma_{d1}\|000\}, \{\sigma_{v1}\|00\frac{1}{2}\}]$	$R_9\oplus R_9$	$R_1\oplus R_2\oplus R_3$	$[U,S',R]\to a$
H	$G_{12}^{4}\otimes T_3\otimes T_2$	$[\{C_3^+\|000\}, \{\sigma_{d1}\|000\}]$	$R_6\oplus R_6$	$R_1\oplus R_5$	$[S',S]\to a, P\to d$
186 $P6_3mc^{22}$					
L	G_{16}^{8}	$[\{\sigma_{v1}\|000\}, \{\sigma_{d1}\|00\frac{1}{2}\}]$	$R_9\oplus R_9$	$R_1\oplus R_2\oplus R_3$	$[U,S',R]\to a$
192 $P6/mcc^{23}$					
L	G_{32}^{7}	$[\{\sigma_{d1}\|00\frac{1}{2}\}, \{\sigma_h\|000\}, \{I\|000\}]$	$R_{13}\oplus R_{14}$	$R_2\oplus R_4\oplus R_6$	$[U,S',R]\to a$
H	$G_{48}^{14}\otimes T_3$	$[\{\sigma_{d1}\|00\frac{1}{2}\}, \{C_3^+\|000\}, \{\sigma_h\|000\}]$	$R_{11}\oplus R_{12}$	$R_3\oplus R_9$	$[S',S,P]\to a$

Table 3.10: Symmetry protected Dirac points in the Hexagonal Primitive Lattice

Cubic Primitive Lattice Γ_c

Real lattice vectors $\mathbf{t}_i$	$\{(a,0,0),(0,a,0),(0,0,a)\}$
Reciprocal lattice vectors $\mathbf{g}_i$	$\{2\pi/a(1,0,0),2\pi/a(0,1,0),2\pi/a(0,0,1)\}$
High symmetry points	M $=(\frac{1}{2}\frac{1}{2}0)$, X $=(0\frac{1}{2}0)$
High symmetry lines	Z $=(\alpha\frac{1}{2}0)$, T $=(\frac{1}{2}\frac{1}{2}\alpha)$, $\Sigma=(\alpha\alpha0)$, S $=(\alpha\frac{1}{2}\alpha)$, $\Delta=(0\alpha0)$

198 $P2_13^{24}$					
M	G_{16}^{8}	$[\{C_{2z}\|\frac{1}{2}0\frac{1}{2}\},\{C_{2x}\|\frac{1}{2}\frac{1}{2}0\}]$	$R_9\oplus R_9$	$R_2\oplus R_3\oplus R_4$	[Z, T] $\to$ a, $\Sigma\to$ b
201 $Pn3^{25}$					
X	G_{32}^{7}	$[\{\sigma_z\|\frac{1}{2}\frac{1}{2}\frac{1}{2}\},\{\sigma_y\|\frac{1}{2}\frac{1}{2}\frac{1}{2}\},\{I\|\frac{1}{2}\frac{1}{2}\frac{1}{2}\}]$	$R_{13}\oplus R_{14}$	$R_2\oplus R_4\oplus R_6$	[Z, S, Δ] $\to$ a
M	G_{32}^{7}	$[\{\sigma_x\|\frac{1}{2}\frac{1}{2}\frac{1}{2}\},\{\sigma_z\|\frac{1}{2}\frac{1}{2}\frac{1}{2}\},\{I\|\frac{1}{2}\frac{1}{2}\frac{1}{2}\}]$	$R_{13}\oplus R_{14}$	$R_2\oplus R_4\oplus R_6$	[Z, T, Σ] $\to$ a
212 $P4_332^{26}$					
M	G_{32}^{11}	$[\{C_{4z}^{-}\|\frac{3}{4}\frac{3}{4}\frac{1}{4}\},\{C_{2x}\|\frac{1}{2}\frac{1}{2}0\}]$	$R_6\oplus R_7$	$R_2\oplus R_5$	[Z, T] $\to$ a, $\Sigma\to$ b
213 $P4_132^{27}$					
M	G_{32}^{11}	$[\{C_{4z}^{-}\|\frac{1}{4}\frac{1}{4}\frac{3}{4}\},\{C_{2x}\|\frac{1}{2}\frac{1}{2}0\}]$	$R_6\oplus R_7$	$R_2\oplus R_5$	[Z, T] $\to$ a, $\Sigma\to$ b
222 $Pn3n^{28}$					
X	G_{64}^{1}	$[\{I\|\frac{1}{2}\frac{1}{2}\frac{1}{2}\},\{\sigma_x\|\frac{1}{2}\frac{1}{2}\frac{1}{2}\},\{C_{4y}^{-}\|000\}]$	$R_{19}\oplus R_{20}$, $R_{21}\oplus R_{22}$	$R_6\oplus R_{14}$	[Z, S, Δ] $\to$ a
M	G_{64}^{2}	$[\{C_{4z}^{-}\|000\},\{\sigma_x\|\frac{1}{2}\frac{1}{2}\frac{1}{2}\},\{C_{2x}\|000\}]$	R_{19}	$R_8\oplus R_{13}$	[Z, T, Σ] $\to$ a
223 $Pm3n^{29}$					
X	G_{64}^{2}	$[\{C_{4y}^{+}\|\frac{1}{2}\frac{1}{2}\frac{1}{2}\},\{\sigma_{de}\|\frac{1}{2}\frac{1}{2}\frac{1}{2}\},\{C_{2e}\|\frac{1}{2}\frac{1}{2}\frac{1}{2}\}]$	R_{19}	$R_8\oplus R_{13}$	[Z, S, Δ] $\to$ a
224 $Pn3m^{30}$					
X	G_{64}^{2}	$[\{C_{4y}^{+}\|\frac{1}{2}\frac{1}{2}\frac{1}{2}\},\{\sigma_x\|\frac{1}{2}\frac{1}{2}\frac{1}{2}\},\{C_{2x}\|000\}]$	R_{19}	$R_8\oplus R_{13}$	[Z, S, Δ] $\to$ a
M	G_{64}^{2}	$[\{C_{4z}^{-}\|\frac{1}{2}\frac{1}{2}\frac{1}{2}\},\{\sigma_x\|\frac{1}{2}\frac{1}{2}\frac{1}{2}\},\{C_{2x}\|000\}]$	R_{19}	$R_8\oplus R_{13}$	[Z, T, Σ] $\to$ a

Table 3.11: Symmetry protected Dirac points in the Cubic Primitive Lattice

Cubic Face-centered Lattice Γ_c^f

Real lattice vectors $\mathbf{t}_i$	$\{1/2(0,a,a), 1/2(a,0,a), 1/2(a,a,0)\}$
Reciprocal lattice vectors $\mathbf{g}_i$	$\{2\pi/a(-1,1,1), 2\pi/a(1,-1,1), 2\pi/a(1,1,-1)\}$
High symmetry points	X $= (\frac{1}{2}0\frac{1}{2})$, W $= (\frac{1}{2}\frac{1}{4}\frac{3}{4})$
High symmetry lines	Z $= (\frac{1}{2}, \alpha, \frac{1}{2}+\alpha)$, S $= (\frac{1}{2}+\alpha, 2\alpha, \frac{1}{2}+\alpha)$, $\Delta = (\alpha 0 \alpha)$, Q $= (\frac{1}{2}, \frac{1}{2}-\alpha, \frac{1}{2}+\alpha)$, $K \equiv S$

203 $Fd3^{31}$					
X	G_{32}^7	$[\{\sigma_z\|\frac{1}{4}\frac{1}{4}\frac{1}{4}\}$, $\{\sigma_y\|\frac{1}{4}\frac{1}{4}\frac{1}{4}\}$, $\{I\|\frac{1}{4}\frac{1}{4}\frac{1}{4}\}]$	$R_{13} \oplus R_{14}$	$R_2 \oplus R_4 \oplus R_6$	$[Z, S, \Delta] \to a$
226 $Fm3c^{32}$					
W	$G_{16}^{14} \otimes T_4$	$[\{S_{4x}^-\|\frac{1}{2}\frac{3}{2}\frac{1}{2}\}$, $\{C_{2f}\|000\}]$	$R_6 \oplus R_7$	$R_4 \oplus R_5$	$[Z, Q, K] \to a$
227 $Fd3m^{33}$					
X	G_{64}^2	$[\{C_{4y}^+\|\frac{1}{4}\frac{1}{4}\frac{1}{4}\}$, $\{\sigma_x\|\frac{1}{4}\frac{1}{4}\frac{1}{4}\}$, $\{C_{2x}\|000\}]$	R_{19}	$R_8 \oplus R_{13}$	$[Z, S, \Delta] \to a$
228 $Fd3c^{34}$					
X	G_{64}^2	$[\{C_{4y}^+\|\frac{1}{4}\frac{1}{4}\frac{1}{4}\}$, $\{\sigma_x\|\frac{3}{4}\frac{3}{4}\frac{3}{4}\}$, $\{C_{2x}\|000\}]$	R_{19}	$R_8 \oplus R_{13}$	$[Z, S, \Delta] \to a$
W	G_{64}^3	$[\{S_{4x}^+\|\frac{1}{2}\frac{1}{2}\frac{1}{2}\}$, $\{\sigma_z\|\frac{3}{4}\frac{3}{4}\frac{3}{4}\}]$	$R_{20} \oplus R_{20}$	$R_6 \oplus R_{17}$	$[Z, Q, K] \to a$

Table 3.12: Symmetry protected Dirac points in the Cubic Face-centered Lattice

Cubic Body-centered Lattice Γ_c^v

Real lattice vectors $\mathbf{t}_i$	$\{1/2(-a,a,a), 1/2(a,-a,a), 1/2(a,a,-a)\}$
Reciprocal lattice vectors $\mathbf{g}_i$	$\{2\pi/a(0,1,1), 2\pi/a(1,0,1), 2\pi/a(1,1,0)\}$
High symmetry points	P = $(\frac{1}{4}\frac{1}{4}\frac{1}{4})$, N = $(00\frac{1}{2})$
High symmetry lines	D = $(\alpha,\alpha,\frac{1}{2}-\alpha)$, F = $(\frac{1}{4}+\alpha,\frac{1}{4}-3\alpha,\frac{1}{4}+\alpha)$, Λ = $(\alpha\alpha\alpha)$, $\Sigma = (00\alpha)$, G = $(\alpha\bar{\alpha}\frac{1}{2})$

204 $Im3^{35}$					
P	$G_{24}^9 \otimes T_4$	$[\{C_{31}^-\|000\}, \{C_{2x}\|000\}, \{\bar{C}_{2y}\|000\}]$	$R_5 \oplus R_6$	R_7	$[D,F,\Lambda] \to a$
206 $Ia3^{36}$					
N	$G_{16}^{10} \otimes T_4$	$[\{C_{2z}\|\frac{1}{2}0\frac{1}{2}\}, \{E\|001\}, \{I\|000\}]$	$R_{10} \oplus R_{10}$	$R_2 \oplus R_2 \oplus R_4$	$[\Sigma,G,D] \to a$
217 $I\bar{4}3m^{37}$					
P	$G_{48}^{10} \otimes T_4$	$[\{S_{4x}^-\|000\}, \{\bar{C}_{31}^-\|000\}, \{\sigma_{db}\|000\}]$	R_8	R_7	$D \to a, [F,\Lambda] \to d$
229 $Im3m^{38}$					
P	$G_{48}^{10} \otimes T_4$	$[\{S_{4x}^+\|000\}, \{\bar{C}_{31}^-\|000\}, \{\sigma_{db}\|000\}]$	R_8	R_7	$[D,F,\Lambda] \to a$
230 $Ia3d^{39}$					
N	G_{32}^7	$[\{\sigma_{db}\|\frac{1}{2}\frac{1}{2}\frac{1}{2}\}, \{\sigma_{da}\|\frac{1}{2}00\}, \{I\|000\}]$	$R_{13} \oplus R_{14}$	$R_2 \oplus R_4 \oplus R_6$	$[\Sigma,G,D] \to a$

Table 3.13: Symmetry protected Dirac points in the Cubic Body-centered Lattice

3.2. Notes to Tables of Symmetry Protected Dirac Points

1. 52 Pnna has FDIRs at Z, U, and R, which do not split along the lines ZU, and UR.

2. 53 Pmna has FDIRs at Z and U, which do not split along the line ZU.

3. 54 Pcca has FDIRs at Z, U, R, and T, which do not split along the lines ZU, UR, and TR.

4. 56 Pccn has FDIRs at U, R, T, Y, S, and X, which do not split along the lines UR, TR, TY, RS, and UX.

5. 58 Pnnm has FDIRs at X, Y, S, and R, which do not split along the lines XS, SY, and RS.

6. 60 Pbcn has FDIRs at X, Y, T, R,and S, which do not split along the lines XS, TR, and TY.

7. 63 Cmcm has FDIRs at Z and T, which do not split along ZB and TG (Type 1) and along ZT (Type 2).

8. 64 Cmca has FDIRs at Z and T, which do not split along ZB and TG (Type 1) and along ZT (Type 2).

9. 114 $P\bar{4}2_1c$ has FDIRs at the points M and A which do not split along the line MA.

10. 128 P4/mnc has FDIRs at the points M, A, and X, which do not split along the lines MA and AX.

11. 130 P4/ncc has FDIRs at the points M, A, X, and R, which do not split along

the lines MA, RX, and AR.

12. 135 $P4_2/mbc$ has FDIRs at points M, A, X, and R, which do not split along the lines MA, XM, and AR.

13. 136 $P4_2/mnm$ has FDIRs at points M, A, and X, which do not split along the lines MA and XM.

14. 137 $P4_2/nmc$ has FDIRs at points M, A, X, and R, which do not split along the lines MA and XR.

15. 138 $P4_2/ncm$ has FDIRs at points M, A, X, and R, which do not split along the lines MA, XR, and AR.

16. 167 $R\bar{3}c$ has an FDIR at Z but the little group G_Z contains a threefold rotation symmetry.

17. 163 $P\bar{3}1c$ has an FDIR at A but the little group G_A contains a threefold rotation symmetry.

18. 165 $P\bar{3}c1$ has an FDIR at A but the little group G_A contains a threefold rotation symmetry.

19. 176 $P6_3m$ has an FDIR at A but the little group G_A contains a sixfold rotation symmetry.

20. 184 P6cc has an FDIR at A but the little group G_A contains a sixfold rotation symmetry.

21. 185 $P6_3cm$ has an FDIR at A but the little group G_A contains a threefold rotation symmetry.

22. 186 $P6_3mc$ has an FDIR at A but the little group G_A contains a threefold rotation symmetry.

23. 192 P6/mcc has an FDIR at A but the little group G_A contains a threefold rotation symmetry.

24. 198 $P2_13$ has a FDIR at Γ and a six dimensional irreducible representation at R. The little groups G_Γ and G_R contain threefold rotation symmetries.

25. 201 Pn3 has FDIRs at Γ and R, but the little groups G_Γ and G_R contain threefold rotation symmetries.

26. 212 $P4_332$ has a FDIR at Γ, and a six dimensional irreducible representation at R. The little groups G_Γ and G_R contain threefold rotation symmetries.

27. 213 $P4_132$ has a FDIR at Γ, and a six dimensional irreducible representation at R. The little groups G_Γ and G_R contain threefold rotation symmetries.

28. 222 Pn3n has a FDIR at Γ and and an eight dimensional irreducible representation at R, but the little groups G_Γ and G_R contain threefold rotation symmetries.

29. 223 Pm3n has a FDIR at Γ and and an eight dimensional irreducible representation at R, but the little groups G_Γ and G_R contain threefold rotation symmetries.

30. 224 Pn3m has FDIRs at Γ and R, but the little groups G_Γ and G_R contain threefold rotation symmetries.

31. 203 Fd3 has a FDIR at Γ but the little group G_Γ contains a threefold rotation symmetry.

32. 226 Fm3c has FDIRs at Γ and L but the little groups G_Γ and G_L contain threefold rotation symmetries.

33. 227 Fd3m has a FDIR at Γ but the little group G_Γ contains a threefold rotation symmetry.

34. 228 Fd3c has FDIRs at Γ and L, but the little groups G_Γ and G_L contain threefold rotation symmetries.

35. 204 Im3 has FDIRs at Γ and H, but the little groups G_Γ and G_H contain threefold rotation symmetries.

36. 206 Ia3 has FDIRs at Γ and H, and a six dimensional irreducible representation at P. The little groups G_Γ and G_H contain threefold rotation symmetries.

37. 217 $I\bar{4}3m$ has FDIRs at Γ and H, but the little groups G_Γ and G_H contain threefold rotation symmetries.

38. 229 Im3m has FDIRs at Γ and H, but the little groups G_Γ and G_H contain threefold rotation symmetries.

39. 230 Ia3d has a FDIR at Γ, a six dimensional irreducible representation at P, and an eight dimensional irreducible representation at H. The little groups G_Γ, G_H, and G_P contain threefold rotation symmetries.

Chapter 4

Material realizations of Dirac semimetals

The previous Chapters have focused on describing the symmetry criteria necessary for the existence of symmetry protected Dirac points at specific points in the BZ. But our goal is to find realistic materials that satisfy the symmetry criteria and exhibit the Dirac point at the Fermi surface. Furthermore, the symmetry criteria, if satisfied, does not preclude the existence of additional Fermi surface besides the Dirac point. Although the diminishing effects of additional Fermi surface on the phenomenology resulting from Dirac points have not yet been made precise, we can safely assume that such effects will be significant given that the density of states at the Dirac point vanishes as the Fermi level approaches the Dirac point while additional Fermi surface pockets inevitably continue to have available states. Although, information about candidate BZ momenta for Dirac points in a spacegroup is useful, designing Dirac materials remains a major challenge that requires empirical reasoning based on chemical considerations.

To that end, we have made use of significant computing resources employing density functional theory methods and studied a number of candidate materials in the diamond, spinel, zincblende, laves, and tetragonal lattices. So far, we have identified six candidate Dirac semimetals; BiO_2, SbO_2 in the diamond lattice (spacegroup 227) (Young et al., 2012); and $BiZnSiO_4, BiMgSiO_4, BiCaSiO_4$ and$BiAlInO_4$ in the distorted spinels lattice (spacegroup 74) (Steinberg et al., 2014). We performed *ab initio* calculations using the plane wave density functional theory package QUANTUM ESPRESSO (Giannozzi et al., 2009), and designed non-local pseudopo-

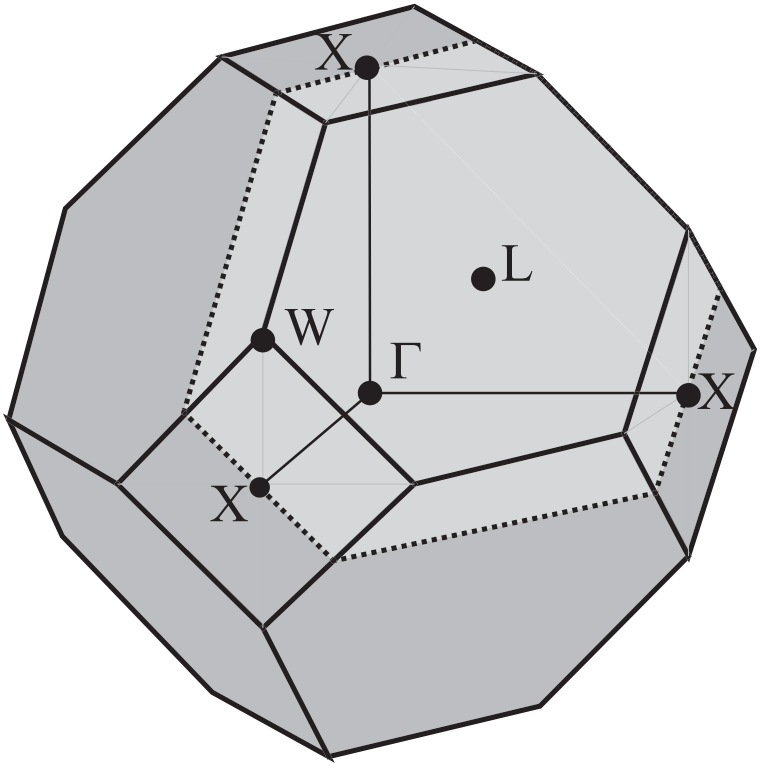

Figure 4.1: Brillouin zone (BZ) of the FCC lattice. The plane highlighted in gray joins the three symmetry related X points. Other high symmetry points are also indicated.

tentials (Rappe et al., 1990; Ramer and Rappe, 1999) with spin-orbit interaction generated by OPIUM. For all calculations an energy cutoff of 50Ry and k-point grids of $8 \times 8 \times 8$ were used for the primitive cell.

A rule of thumb in the search for Dirac semimetals is to look for materials where the states near the Fermi energy are dominated by single unpaired s, p, d, f orbitals. The presence of an unpaired electron is required by symmetry considerations. Consider a generic Dirac point: the fourfold degeneracy requires four distinct quantum numbers, two of which are provided by the electron spin since time reversal is assumed to be preserved, while the other two arise from a sublattice or chiral symmetry which is always present in nonsymmorphic spacegroups. There is no room for any extra orbital

degree of freedom. We can hence conclude that symmetry protected Dirac semimetals require a prevalence of unpaired s, p, d, f orbital states near the Fermi energy. In other words, there must be an odd number of electrons per formula unit to guarantee that the Fermi energy bisects the Dirac point. This signifies that the physics at the Dirac point is driven by unpaired electrons delocalized across the crystal lattice.

In this Chapter, we describe the band structure of some realistic Dirac semimetals, and show how representations of the Dirac point can be used to construct an effective $\mathbf{k} \cdot \mathbf{p}$ theory of the Fermi surface. The $\mathbf{k} \cdot \mathbf{p}$ theory is useful for understanding the effects of symmetry breaking perturbations on the Dirac point. Indeed, we discover that Dirac points have access to a rich number of exotic insulating and semimetallic phases; strong and weak topological insulators, weyl semimetals with nodal points, rings and surfaces etc. In Section 4.3, we construct a tight binding theory of p-orbitals on the distorted spinels lattice and show that the Dirac point in that lattice can be interpreted as a three dimensional version of the undimerized Su-Schrieffer-Heeger (SSH) model (Su et al., 1979). The three dimensional Dirac point, unlike the one dimensional Dirac point in the SSH model, remains undimerized in the ground state presenting evidence for the lack of Peierls instability in three dimensions.

4.1. Dirac points in the diamond lattice

The diamond lattice (spacegroup 227) exhibits a Dirac point at the high symmetry point X as shown in Table 3.12. States at the Dirac point span the four dimensional representation R_{19} of the abstract group G^2_{64} which is isomorphic to the central extension group of the isogonal point group at X. The symmetry group at X is generated by spacegroup elements $[\{\mathrm{C}^+_{4\mathrm{y}}|\frac{1}{4}\frac{1}{4}\frac{1}{4}\}, \{\sigma_{\mathrm{x}}|\frac{1}{4}\frac{1}{4}\frac{1}{4}\}, \{\mathrm{C}_{2\mathrm{x}}|000\}]$. Thus, the Dirac point at X is protected by fourfold rotation symmetry, mirror symmetry and the sublattice

symmetry of the diamond lattice. The diamond lattice has the symmetry of a cube because it consists of two interpenetrating FCC lattices. As shown in Figure 4.1, the point X lies on the BZ surface and does not have threefold symmetry, but there exist three equivalent X points related by the threefold symmetry that exchanges the BZ faces. Therefore the diamond lattice exhibits three Dirac points at X all occurring at the same energy. The Dirac point splits into twofold degenerate bands along the high symmetry lines Z, S and Δ away from X as shown in Table 3.12.

The existence of a Dirac point in the diamond lattice was first demonstrated using a tight-binding model of s-orbitals (Fu et al., 2007). The diamond lattice has an additional FDIR at the point Γ but the presence of inversion symmetry prohibits the bands from dispersing linearly. Since X and Γ are not related by symmetry, the two FDIRs do not necessarily have to appear at the same energy.

In the model described by Fu et al. (2007), the Dirac point appears at the Fermi energy. However, in known materials on a diamond lattice s-states appear below the Fermi energy. In realistic systems, additional orbitals hybridize with these s-states and bands cross the Fermi level at other points besides X. The problem is especially severe in spacegroup 227: without spin, the line Z from X to W is twofold degenerate. With spin-orbit coupling, this line splits weakly for lighter atoms so the bands dispersing along this line can hybridize and introduce additional Fermi surface. Forcing species with s^1 valence states on the diamond lattice would fail to realize the model of Fu et al. (2007). Indeed, *ab initio* calculations with group I elements and gold show that the splitting along Z is insufficient to overcome this dispersion. In some cases, additional bands cross the Fermi level.

We consider derivatives of the diamond lattice that remain in spacegroup 227. We place additional atoms in the lattice such that the configuration of added species

allows its valence orbitals to either belong to the FDIR of interest, or appear away from the Fermi energy of the final structure. If the new species can split the nearby p states of the existing atoms away from the s levels, band crossing at the Fermi level can be avoided.

One such structure is β-cristobalite SiO_2 (Fig. 4.3), which consists of silicon atoms on a diamond lattice with oxygen atoms placed midway along each silicon-silicon bond (Calvert and Villars, 1991). Oxygen atoms have two consequences: part of the O p-shell strongly hybridizes with the Si p-states, moving them away from the Si s-states, while the remaining O p-states span the same representation as the Si s-states. A Dirac point can be realized by Si $s-$O p bonding/anti-bonding set of states. Figure 4.2 shows that the Si $s-$O p bands are present and take a configuration similar to the valence and conduction bands in Fu et al. (2007), but appear well below the Fermi energy. Additionally, the bands are nearly degenerate along the line Z from X to W due to weak spin-orbit coupling.

Heavier atoms substituting Si both widen this gap and bring the FDIR of interest at X to the Fermi level. Figures 4.4, 4.5, and 4.6 show the band structures of compounds β-cristobalite XO_2 where X = As/Sb/Bi respectively. The change in chemical identity promotes the X $s-$O p four-fold degeneracy at X to the Fermi level, and stronger spin-orbit coupling widens the gap along V. BiO_2 (Fig. 4.6) bears striking similarity to the s-orbitals model (Fu et al., 2007) (Fig. 4.7), with linearly dispersing bands in a large energy range around a Dirac point at the Fermi level. Our calculations show that the phonon frequencies for β-cristobalite BiO_2 at Γ are positive, so it is a metastable structure. Further calculations reveal that it becomes unstable under uniform compression exceeding 2GPa, which represents a stability barrier of approximately 0.025eV per atom. On this basis, the possibility of synthesis ap-

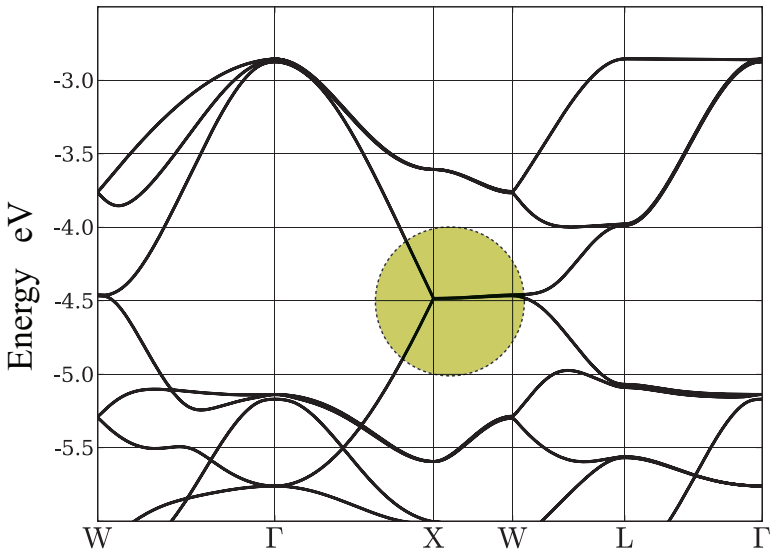

Figure 4.2: Band structure of β-cristobalite SiO_2. Energy bands are plotted relative to the Fermi level. Each band is two-fold degenerate due to inversion symmetry. The (highlighted) FDIR at -4.5 eV is split into two linearly dispersing bands between X and Γ while the two degenerate bands along X and W are weakly split. This FDIR is buried deep below the Fermi level.

pears promising. However, Bi_2O_4 is also likely to take the cervantite structure (after Sb_2O_4, which has similar stoichiometry (Thornton, 1977)) which is 0.5 eV per atom lower in energy as compared to β-cristobalite and 60% smaller in volume. Therefore we conclude that β-cristobalite BiO_2 would be metastable if synthesized, although preventing it from directly forming the cervantite structure would be challenging.

The band structures of BiO_2 and SbO_2 in Figures 4.6 and 4.5 respectively demonstrate the existence of a pointlike Fermi surface at X with linearly dispersing bands in the vicinity of X. Thus, we have provided an existence proof of a Dirac semimetal in β-cristobalite BiO_2 and SbO_2 due to real atomic potentials at the DFT level.

The $\mathbf{k}\cdot\mathbf{p}$ theory at the Dirac point can be derived from the tight binding Hamiltonian of s orbitals in Fu et al. (2007). We perform the same calculation using the representation R_{19} of the abstract group G_{64}^2 to demonstrate the use of group theoretic

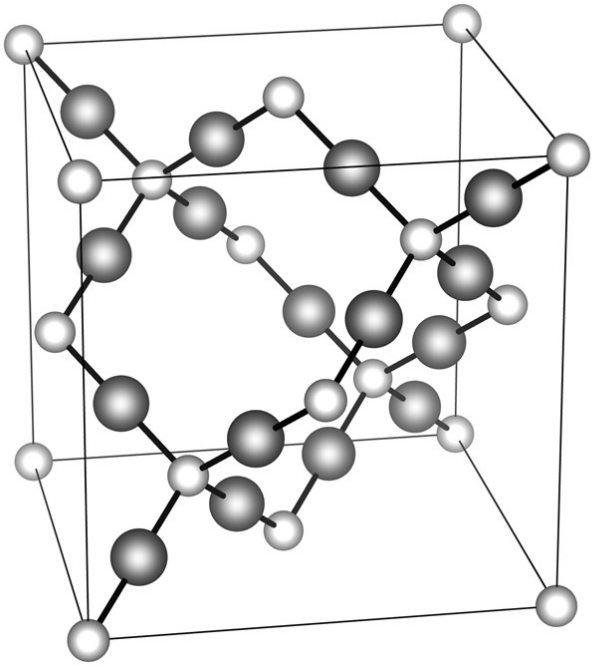

Figure 4.3: The β-cristobalite structure of SiO_2 (BiO_2). Silicon (bismuth) atoms (light gray) are arranged on a diamond lattice, with oxygen atoms (dark gray) sitting midway between pairs of silicon (bismuth).

information to calculate effective Hamiltonians. In the FDIR R_{19} of the symmetry group G_{64}^2 at X, the generators can be represented as, $\left\{C_{4y}^+|\frac{1}{4}\frac{1}{4}\frac{1}{4}\right\} = \frac{1}{\sqrt{2}}\tau_3\left(i\sigma_1 - 1\right)$, $\left\{\sigma_x|\frac{1}{4}\frac{1}{4}\frac{1}{4}\right\} = \tau_1\sigma_2$, $\{C_{2x}|000\} = i\sigma_3$ (Bradley and Cracknell, 1976). The time reversal operator in this basis takes the form $\Theta = i\tau_3\sigma_2\mathrm{K}$. The point X is symmetric under time reversal, so all the matrices appearing in the Dirac Hamiltonian $\mathcal{H}(\mathbf{k})$ anticommute with Θ. Therefore, the set of possible Dirac matrices that can appear at X is,

$$\left\{\sigma_1, \sigma_2, \sigma_3, \tau_3\sigma_1, \tau_3\sigma_2, \tau_3\sigma_3, \tau_1, \tau_2\sigma_1, \tau_2\sigma_2, \tau_2\sigma_3\right\}.$$

Following the discussion in Section 2.3, the symmetry group G_{64}^2 at X imposes the

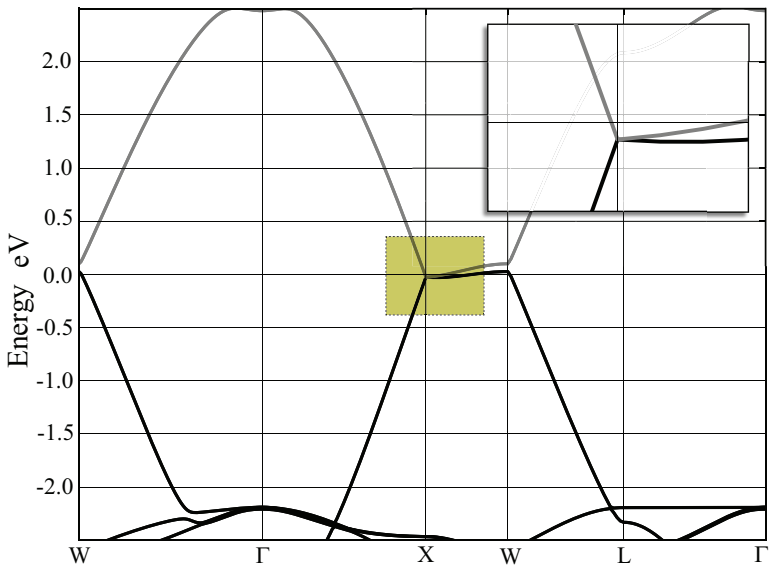

Figure 4.4: Band structure of β-cristobalite AsO_2. Energy bands are plotted relative to the Fermi level. Each band is two-fold degenerate due to inversion symmetry. Inset: with increasing atomic number of the cation, spin-orbit coupling widens the gap along the line Z from X to W. In AsO_2 the spin-orbit coupling is not sufficient to remove the degeneracy sufficiently enough to remove Fermi pockets along the line Z.

following constraints on the Dirac Hamiltonian $\mathcal{H}(\mathbf{k})$,

$$\sum_{i=x,y,z} \alpha_i k_i \left\{ C_{4y}^{+} | \frac{1}{4}\frac{1}{4}\frac{1}{4} \right\} \gamma_i \left\{ C_{4y}^{+} | \frac{1}{4}\frac{1}{4}\frac{1}{4} \right\}^{\dagger} = -\alpha_x k_z \gamma_x + \alpha_y k_y \gamma_y + \alpha_z k_x \gamma_z \quad (4.1)$$

$$\sum_{i=x,y,z} \alpha_i k_i \left\{ \sigma_x | \frac{1}{4}\frac{1}{4}\frac{1}{4} \right\} \gamma_i \left\{ \sigma_x | \frac{1}{4}\frac{1}{4}\frac{1}{4} \right\}^{\dagger} = -\alpha_x k_x \gamma_x + \alpha_y k_y \gamma_y + \alpha_z k_z \gamma_z \quad (4.2)$$

$$\sum_{i=x,y,z} \alpha_i k_i \left\{ C_{2x} | 000 \right\} \gamma_i \left\{ C_{2x} | 000 \right\}^{\dagger} = \alpha_x k_x \gamma_x - \alpha_y k_y \gamma_y - \alpha_z k_z \gamma_z. \quad (4.3)$$

Imposing the above constraints, the Hamiltonian at $X = (\frac{1}{2}0\frac{1}{2}) = \frac{2\pi}{a}(010)$ is uniquely identified to be,

$$\mathcal{H}(\mathbf{k}) = \alpha(k_x\sigma_3 - k_z\sigma_2) + \alpha_y k_y \tau_3 \sigma_1, \quad (4.4)$$

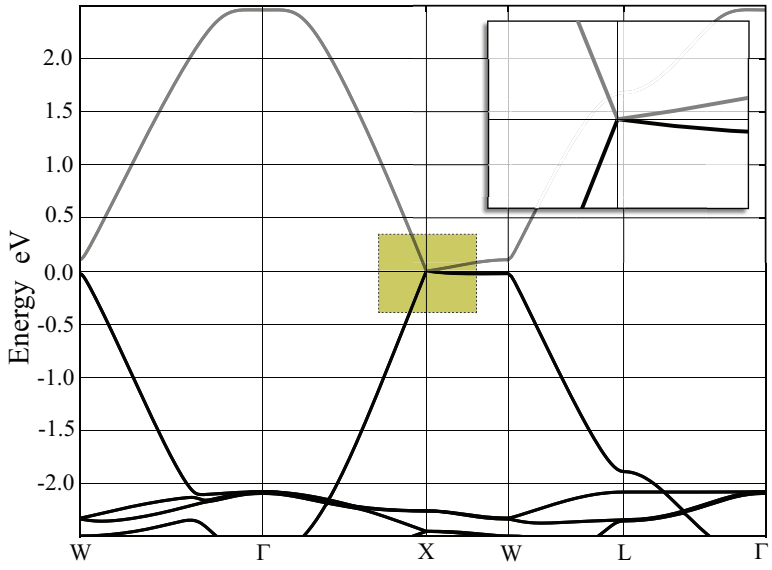

Figure 4.5: Band structure of β-cristobalite SbO_2. Each band is two-fold degenerate due to inversion symmetry. Inset: with increasing atomic number of the cation, spin-orbit coupling widens the gap along the line Z from X to W. In SbO_2, the dispersion around the X point is linear in all directions indicating the existence of Dirac points at X. SbO_2 is a Dirac semimetal because its Fermi surface consists entirely of Dirac points.

where the parameters α and α_y are Fermi velocities and need not be identical. Indeed, the Dirac point in BiO_2 is anisotropic as can be seen in Figure 4.6.

4.2. Dirac points in distorted spinels

The distorted spinels lattice (spacegroup 74) exhibits a Dirac point at the high symmetry point T as shown in Table 3.5. States at the Dirac point span the four dimensional representation $R_9 \oplus R_9$ where R_9 is a two dimensional representation of the abstract group G_{16}^{10}. The degeneracy of representation R_9 with itself is a consequence of time reversal symmetry. The group G_{16}^{10} is isomorphic to the central extension group of the isogonal point group at T. The symmetry group at T is generated by spacegroup elements $[\{\sigma_z|0\frac{1}{2}\frac{1}{2}\}, \{E|100\}, \{I|\frac{1}{2}\frac{1}{2}0\}]$. Thus, the Dirac point at T is protected by time reversal symmetry, mirror symmetry, and sublattice symmetry.

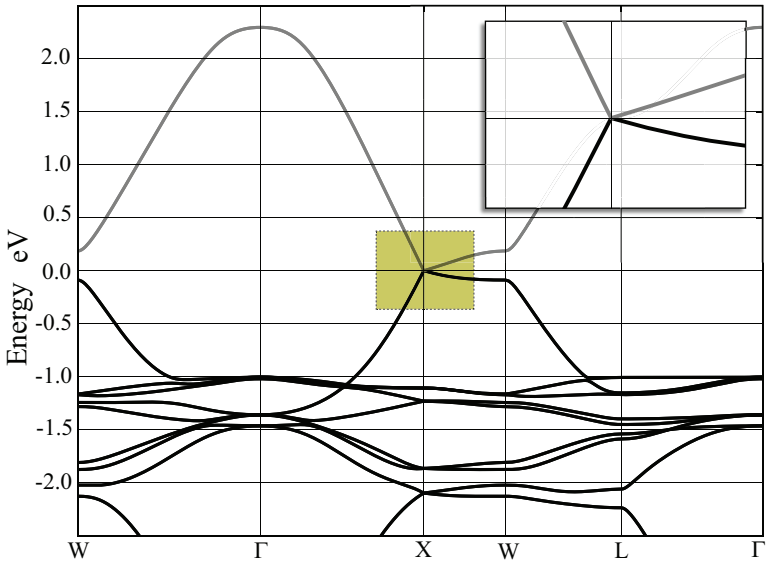

Figure 4.6: Band structure of β-cristobalite BiO_2. Each band is two-fold degenerate due to inversion symmetry. Inset: with increasing atomic number of the cation, spin-orbit coupling widens the gap along the line Z from X to W. In BiO_2, the dispersion around the X point is linear in all directions indicating the existence of Dirac points at X. BiO_2 is a Dirac semimetal because its Fermi surface consists entirely of Dirac points.

The distorted spinels lattice belongs to the body-centered orthorhombic crystal system where the unit cell takes the shape of a distorted cube with unequal sides at right angles to each other. The lattice consists of two interpenetrating simple orthorhombic lattices. Thus the spacegroup 74 is a child symmetry group of spacegroup 227 with broken threefold and fourfold rotation symmetries. This can be seen by comparing the Brillouin zone of spacegroup 74 (Fig. 4.8) with that of the FCC lattice (Fig. 4.1).

The diamond lattice has three Dirac points at the three BZ faces related by threefold symmetry. As the diamond lattice is distorted by breaking the threefold symmetry and the fourfold symmetry, two of the three Dirac points are gapped. The point where the Dirac point survives is labeled T in spacegroup 74. This is indeed confirmed by group theoretic methods as shown in Table 3.5. The Dirac point at T splits into

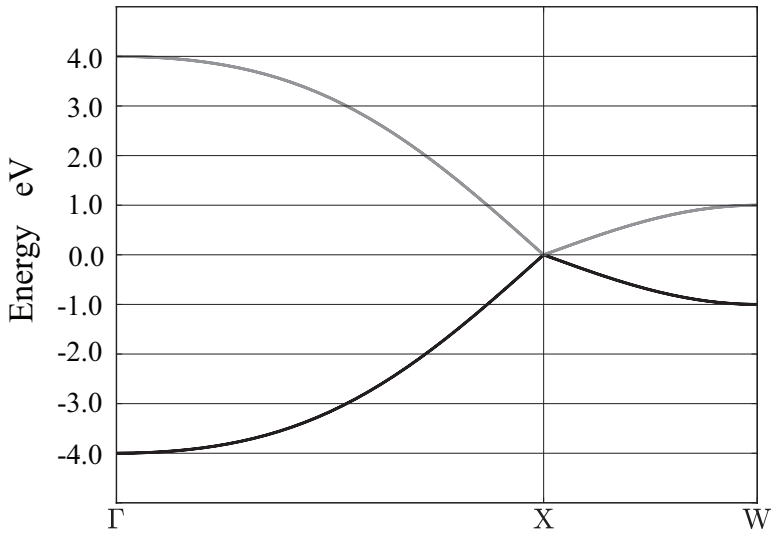

Figure 4.7: Band structure of an s-state model on the diamond lattice from Fu et al. (2007). Energy bands are plotted relative to the Fermi level. Each band is two-fold degenerate due to inversion symmetry.

twofold degenerate bands along the high symmetry line P away from T, and in other directions due to the presence of both sublattice and time reversal symmetry.

The spinel family of materials is a lower symmetry derivative of the β-cristobalite structure. The spinel structure hosts a family of chalcogenides with the general formula AB_2X_4. A and B are cations coordinated by anions of species X, which may be O, S, Se, or Te. The A sites are tetrahedarally coordinated in a diamond lattice, with the octahedrally coordinated B sites in the interstices (Burdett et al., 1982). Most known spinels are insulators with band gaps of a few eV; thus if a spinel can assume the symmetry of a spacegroup that exhibits a Dirac point, the likelihood of additional Fermi pockets is minimal. Hence, spinels are good candidates for Dirac semimetals. In contrast, the Laves structure contains the requisite symmetry for a Dirac point, but materials in the Laves structure tend to be metallic and our attempts to engineer Dirac semimetals were plagued by additional band crossings at the Fermi level.

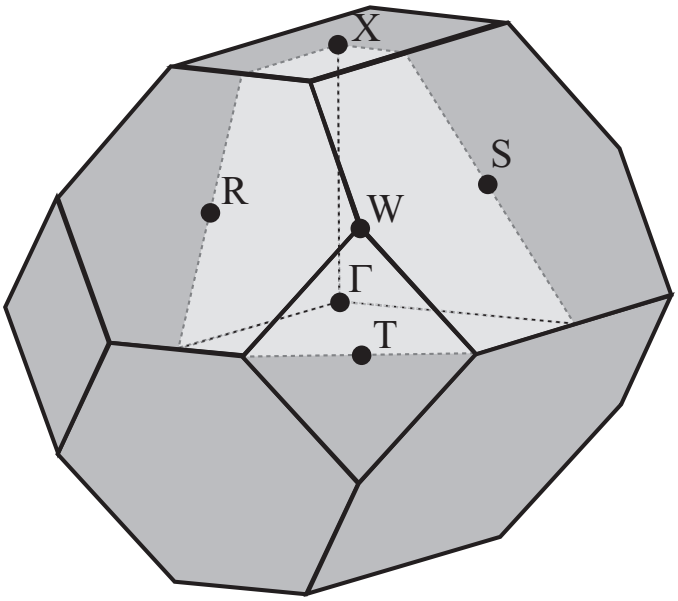

Figure 4.8: Brillouin zone (BZ) of the distorted spinels lattice. The BZ face containing the point T retains its diamond shape as in Figure 4.1, while other faces are strained due to broken threefold and fourfold rotation symmetries of the diamond lattice. This BZ is a distorted version of the FCC lattice BZ (Fig. 4.1). Other high symmetry points are also indicated.

$BiAl_2O_4$ and $BiSc_2O_4$ in the spinel structure (spacegroup 227) exhibit Dirac points at X in the BZ but these materials are not stable and spontaneously break the symmetry required to sustain the Dirac degeneracy. Fortunately, the symmetry distortion in some cases is such that the lattice assumes the symmetry of spacegroup 74 which according to Table 3.5 should host a Dirac point at T. The cubic unit cell (Fig. 4.9) distorts to an orthorhombic cell and the Bismuth atoms shift from their previous locations along one of the twofold rotation axes (Fig. 4.10). This symmetry breaking allows a distinction between the two B atoms in the formula unit, which we label as B′ and B″ (Figs. 4.10 and 4.11), so the composition is $BiB'B''O_4$. This we refer to as the distorted spinel group.

We conducted first principles DFT calculations for various choices of B′ and B″ species and determined that $BiZnSiO_4$ (Fig. 4.13), $BiMgSiO_4$ (Fig. 4.14), $BiCaSiO_4$

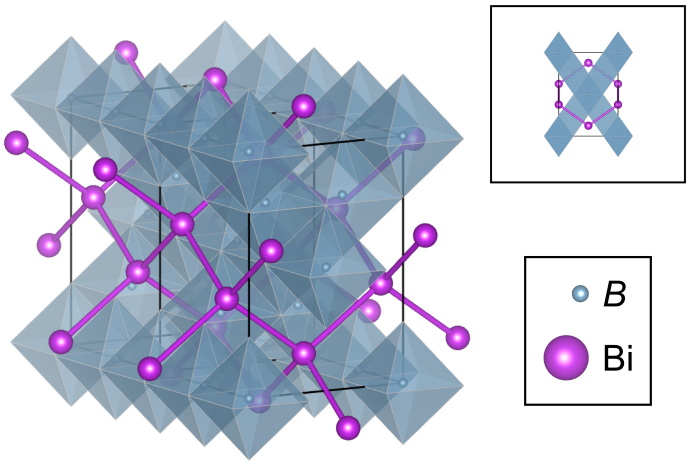

Figure 4.9: The spinel lattice structure. Conventionally, the high-symmetry spinel unit cell is cubic; here we have chosen a reduced supercell allowing for direct comparison with the distorted structure. The A sites, populated by Bi, are surrounded by a tetrahedral oxygen cage (not shown for clarity) and the B sites are surrounded by octahedral oxygen cages. In the high-symmetry spinel all Bi neighbors are equidistant, and the Bi atoms form a diamond lattice.

(Fig. 4.15) and $BiAlInO_4$ (Fig. 4.16) exhibit a Dirac point at T without additional Fermi pockets. We have also calculated phonon energies and found these materials to be metastable. The band structures of these Dirac semimetals are qualitatively identical. States near the Dirac point are dominated by p-orbitals located on the Bi atoms unlike β-cristobalite BiO_2 where the states at the Dirac point were s-like and centered on the Bi atoms as well. The splitting of states along the line P between T and W is controlled by the strength of the spin-orbit coupling due to Bi.

The $\mathbf{k} \cdot \mathbf{p}$ theory at the Dirac point can be derived from a tight binding model of p-orbitals on the Bi sites discussed in Section 4.3. Here, we perform the same calculation using the four dimensional representation $\mathrm{R}_9 \oplus \mathrm{R}_9$ of the symmetry group G_{16}^{10} at T. Symmetry operators that generate G_{16}^{10} are $[\{\sigma_z|0\frac{1}{2}\frac{1}{2}\}, \{\mathrm{E}|100\}, \{\mathrm{I}|\frac{1}{2}\frac{1}{2}0\}]$, however, only the mirror operator and the sublattice operator affect the Dirac point in k-

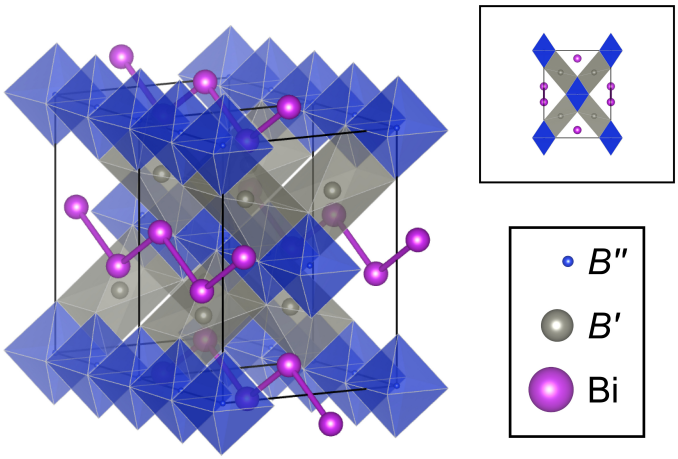

Figure 4.10: The distorted spinel lattice structure. The A sites, populated by Bi, are surrounded by a tetrahedral oxygen cage (not shown for clarity) and the B sites are surrounded by octahedral oxygen cages. In the high-symmetry spinel all Bi neighbors are equidistant, and the Bi atoms form a diamond lattice. Upon distortion, bonds lying in the $(0, 1, 0)$ plane elongate, and the structure can be described as coupled, close-packed, corrugated chains running parallel to $[0, 1, 0]$.

space. These can be represented as $\{\sigma_z|0\frac{1}{2}\frac{1}{2}\} = \sigma_1$ and $\{\mathrm{I}|\frac{1}{2}\frac{1}{2}0\} = \sigma_3$ whereas the time reversal operator $\Theta = i\tau_2\mathrm{K}$. In these coordinates, the k_z-axis points along the line from T to Γ (Bradley and Cracknell, 1976). The Dirac Hamiltonian $\mathcal{H}(\mathbf{k})$ takes the form,

$$\mathcal{H}(\mathbf{k}) = \alpha_x k_x \tau_1 \sigma_3 + \alpha_y k_k \left(\cos\theta \tau_1 \sigma_1 + \sin\theta \tau_1 \sigma_2\right) + \alpha_z k_z \tau_2, \tag{4.5}$$

where α_i are the Fermi velocities and θ is an arbitrary real parameter that ranges within $[0, 2\pi)$. The parameters α_i and θ depend on microscopic features and cannot be determined by symmetry considerations alone.

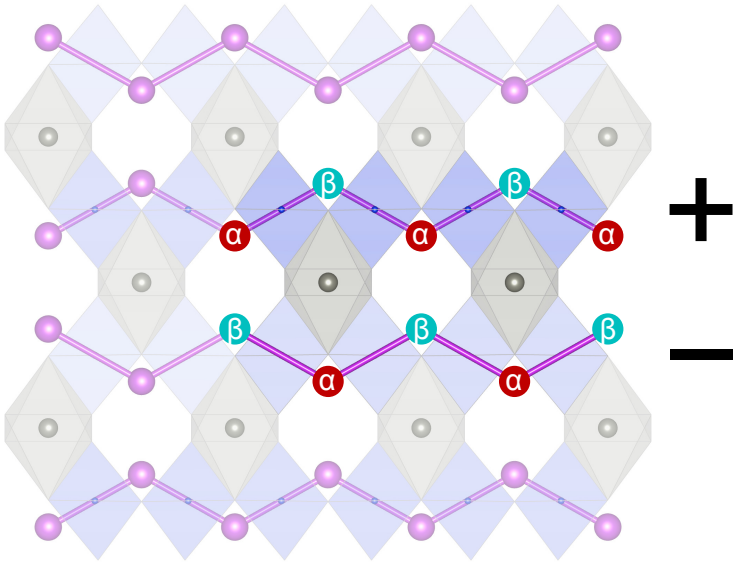

Figure 4.11: Bi chains parallel to the y-axis in the distorted spinel structure. B'' cages are blue, B' cages are gray, and the Bi atoms are in purple. The chains are composed of Bi atoms with alternating bond directions, labeled α and β, forming chains with distinct orientations from their nearest neighbors, signified by $+$ and $-$. Running parallel to $[0, 1, 0]$, the alternatingly oriented chains form their own chain like structure in the $[1, 0, 1]$ direction, so that each chain is now an object coupling to its neighbors in 1D.

4.3. Chain model of 3D Dirac points

In distorted spinels, for example $BiZnSiO_4$, states near the Fermi surface are dominated by p-orbitals originating from Bi atoms. This can verified by the angular-momentum-projected density of states shown in Figure. 4.17. Since Bi has 5 electrons in its outermost shell (Bi is $6s^26p^3$), this suggests that each Bi in $BiZnSiO_4$ possesses a pair of $2s$-electrons and an unpaired p-electron. Thus the Dirac point in this material contrasts with its counterpart BiO_2 where the dominant state at the Fermi level is an unpaired s-orbital on the Bi sites. Therefore we model the low energy theory of distorted spinels in terms of a tight-binding model of p states on the Bi atoms. The two Bi atoms in the unit cell each have p_x, p_y, and p_z orbitals. We distinguish between the two Bi sites (and associated sublattices) with labels A and B. The four nearest neigh-

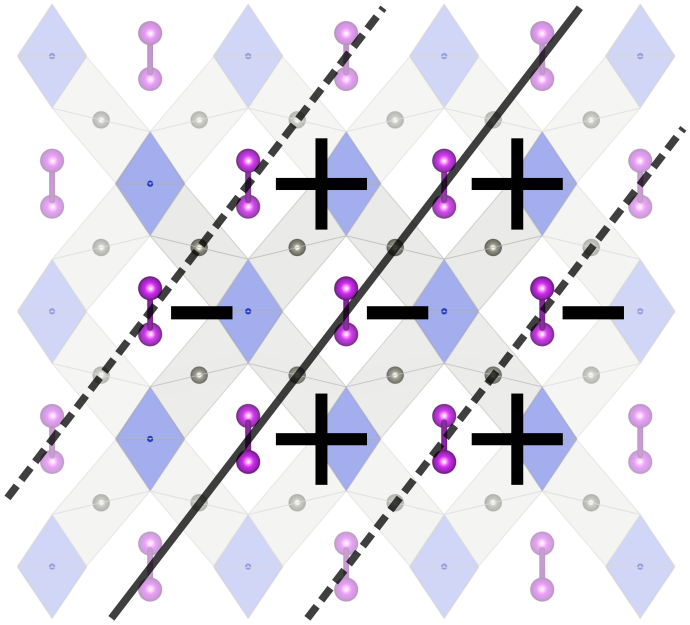

Figure 4.12: The distorted spinel structure with the Bi network annotated. B'' cages are blue, B' cages are gray, and the Bi atoms are in purple. Running parallel to $[0,1,0]$, the alternatingly oriented chains form their own chain like structure in the $[1,0,1]$ direction, so that each chain is now an object coupling to its neighbors in 1D. The resulting parallel planes of alternating sense (denoted by solid and dashed lines), constructed from the sheets of coupled chains, themselves couple with one another in the $[1,0,-1]$ direction. Thus, at each level of structure the elements (atoms, chains, and planes) alternate in orientation along a particular direction, resulting in a fourfold representation for a point on the BZ surface corresponding to one half of a reciprocal lattice vector for each of those directions, and a Dirac point at the Fermi level for half-filling.

bor bonds of each site are, $\mathbf{d}^{1\pm} = (\pm a/2, 0, [1-2\gamma]c)$ and $\mathbf{d}^{2\pm} = (0, \pm b/2, 2\gamma c)$ where a, b, and c are lattice parameters of the orthorhombic crystal system and γ describes an internal distortion; when $a = b = c/\sqrt{2}$ and $\gamma = 1/8$, the lattice assumes the symmetry of diamond. Including spin-orbit coupling (next-nearest-neighbor interaction to preserve sublattice symmetry) , the tight binding Hamiltonian becomes,

$$\mathcal{H}_{tb} = \sum_{\langle ij \rangle} c^{\dagger}_{i,\alpha} c_{j,\beta} \left[(t_\sigma - t_\pi)\,(\alpha \cdot \mathbf{d}_{ij})(\beta \cdot \mathbf{d}_{ij}) + t_\pi (\alpha \cdot \beta) \right] + \sum_{<<ij>>,ss',\alpha\beta} i\lambda_{i\alpha j\beta} \mathbf{d}^1_{ij} \times \mathbf{d}^2_{ij} \cdot \vec{\sigma}_{ss'} c^{\dagger}_{i,\alpha,s} c_{j,\beta,s'}. \tag{4.6}$$

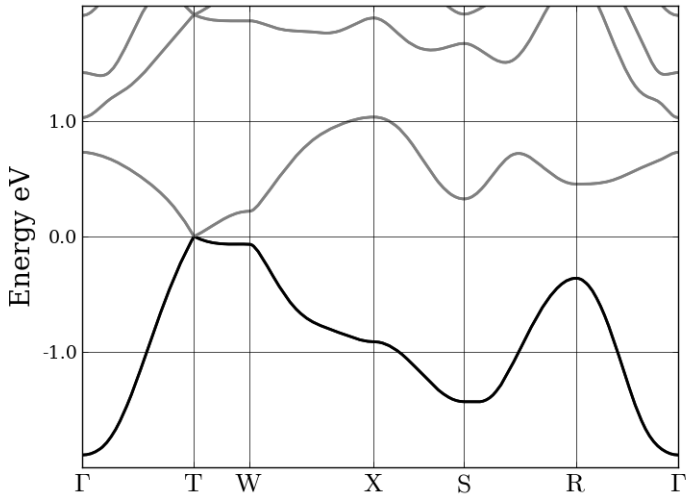

Figure 4.13: The bandstructure of $BiZnSiO_4$ in the distorted spinel structure contains a Dirac point at T that is completely split along the line in the Brillouin zone from T to W due to the spin orbit interaction between the bismuth sites in the lattice.

The Bi sites are indexed by i and j, and the set of p-orbital orientations for site i are labeled by α whereas those for site j are labeled by β. α and β can be unit vectors $\hat{x}$, $\hat{y}$ and $\hat{z}$. t_σ and t_π are phenomenological coupling parameters for the σ and π character of the $p-p$ bonds, and $\mathbf{d}_{ij}$ is one of the aforementioned bond vectors that connect sites i and j. The parameter $\lambda_{i\alpha j\beta}$ controls the spin-orbit coupling strength whereas $\mathbf{d}^1_{ij}$ and $\mathbf{d}^2_{ij}$ are bond vectors 1 and 2 which connect next-nearest-neighbor sites i and j ($\mathbf{d}^1_{ij}$ connects i to k and $\mathbf{d}^2_{ij}$ connects k to j).

The first term in the Hamiltonian produces three pairs of bands separated by $|t_\sigma - t_\pi|$ with each pair corresponding to a single p-orbital. The p-orbital degeneracy is broken by the crystal field because spacegroup 74 does not have threefold symmetry. Within each pair, the bands can be distinguished based on the sublattice. Each pair, however, is degenerate along the line P from T to W. The second spin-orbit term introduces the spin degree of freedom, splits the degeneracy along P, and creates level repulsion

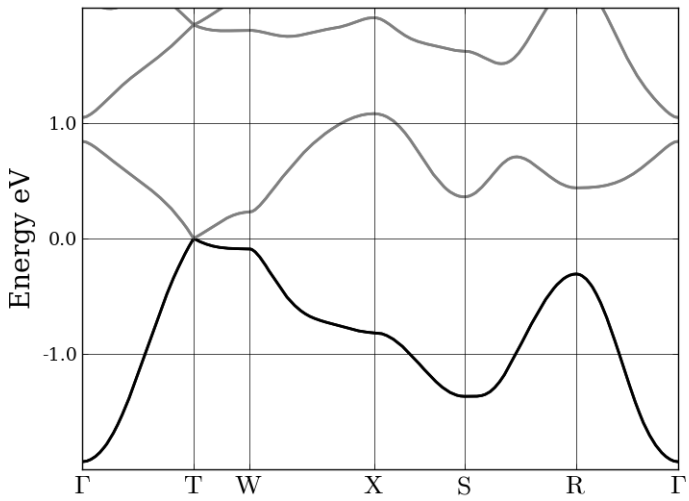

Figure 4.14: The bandstructure of $BiMgSiO_4$ in the distorted spinel structure contains a Dirac point at T that is completely split along the line in the Brillouin zone from T to W due to the spin orbit interaction between the bismuth sites in the lattice.

between the original pairs of bands of order $|t_\sigma - t_\pi| + \lambda$. If we remove the distortion in the lattice and set lattice parameters to $a = b = c/\sqrt{2}$ and $\gamma = 1/8$, we recover the three Dirac points originally at X in diamond. Thus, high symmetry diamond exists as a critical point between the single Dirac point phases allowed by the three ways in which the symmetry of diamond may be reduced to spacegroup 74. Thus we conclude that the Dirac point in diamond is connected to the Dirac point in spacegroup 74.

We make this point more precise by analyzing states proximal to the Fermi energy in $BiZnSiO_4$, which we take as representative of the four spacegroup 74 Dirac semimetals. In Figure 4.18 the Bloch states (excluding the spin degree of freedom) of the Dirac point degeneracy are shown, with a cartoon representation in Figure 4.19 added for clarity. The character of these states confirms that the unpaired p electrons give rise to the observed Dirac point physics: the two states are related by the symmetry between the two Bi sublattices. Existence of the Dirac point in the ground state implies that

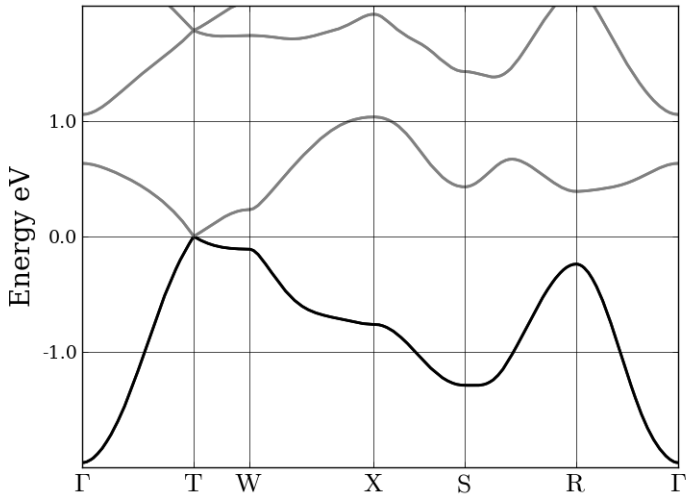

Figure 4.15: The bandstructure of $BiCaSiO_4$ in the distorted spinel structure contains a Dirac point at T that is completely split along the line in the Brillouin zone from T to W due to the spin orbit interaction between the bismuth sites in the lattice.

the system lies at a critical point between the two configurations where Bi atoms pair into dimers. In a one dimensional analog, the Bi atoms dimerize into one of the two possible configurations in the ground state due to Peierls instability (Su et al., 1979). In the 3D case, the sublattice symmetry combined with the mirror symmetry prevents such a dimerization to occur in any direction and the Dirac point remains stable. This symmetry which prevents unpaired p electrons from forming any bonds only exists in the little group at T; elsewhere it is absent and the degeneracy is lifted.

Figures 4.11 and 4.12 show an annotated structure of a distorted spinel. Bi atoms form a chainlike structure going into the plane, and adjacent chains have a different ordering of the two types of Bi atoms. Figure 4.11 illustrates chains of α- and β-type Bi atoms along the y-axis, while Figure 4.12 illustrates that adjacent atoms along the x and z axes form an additional chain-like structure. This suggests that individual chains of Bi sites behave like coupled one dimensional wires running through an otherwise

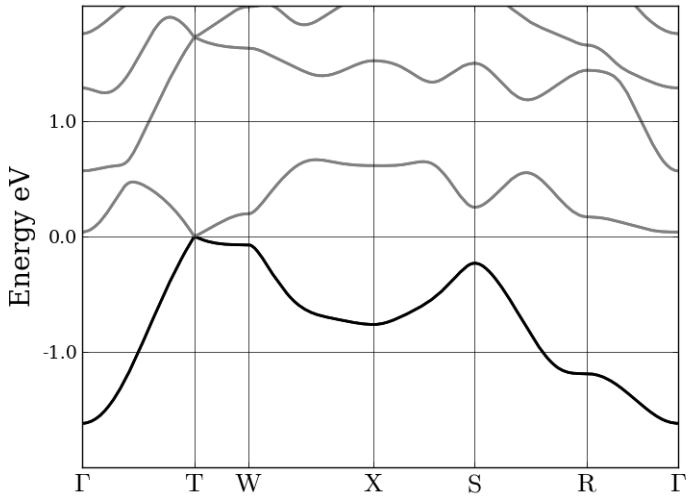

Figure 4.16: The bandstructure of $BiAlInO_4$ in the distorted spinel structure contains a Dirac point at T that is completely split along the line in the Brillouin zone from T to W due to the spin orbit interaction between the bismuth sites in the lattice.

insulating structure. As the one dimensional chains are coupled in a 3D pattern with the symmetry of spacegroup 74, Peierls instability disappears because it is more favorable energetically for the lattice to remain in a higher symmetry state. The protection against dimerization can also be understood in terms of the unfavorable oxidation state +2 that Bi would have to assume if the chains dimerized (Bismuth typically oxidizes as +3 or +5). Furthermore, the other cations are small, encouraging a more closely packed lattice and increasing the favorability of delocalized carriers at the Dirac point and the ensuing metallic character. Thus the critical point, where the oxidation state of Bi is formally undefined and the unpaired electrons remain delocalized, is locally stable. Therefore, the Dirac point at T can be understood as a specific manifestation of the coupling between three levels of chain-like structures. If the chains are arranged in a highly symmetric fashion so that the underlying symmetry group is spacegroup 227, we would find three symmetry related Dirac points of the diamond lattice.

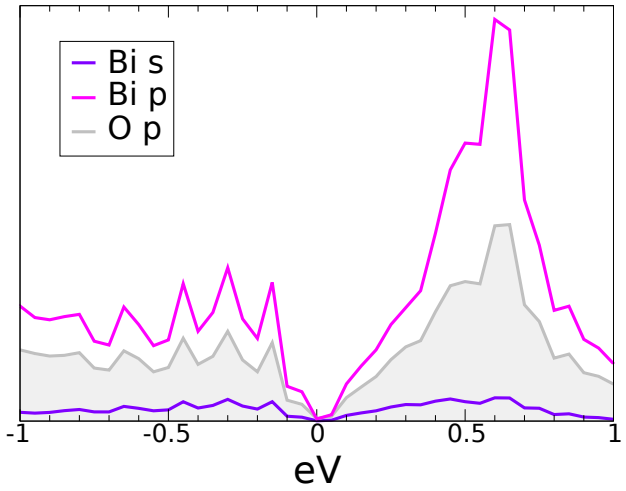

Figure 4.17: Projected density of states near the Dirac point in the $ZnBiSiO_4$ structure. States near the Dirac point are primarily Bi p-states, with a vanishing density at the Fermi energy.

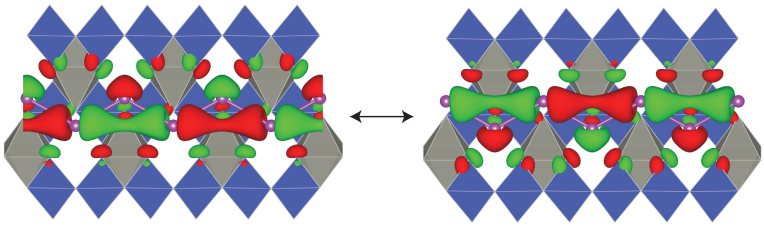

Figure 4.18: The angular portion of the wavefunctions (i.e. without the spin degree of freedom) of the $BiZnSiO_4$ structure at T. Wavefunctions at the Dirac point are a superposition of the states depicted above (spin degree of freedom is removed for clarity). This emphasizes the p-orbital character of the states at the Dirac point.

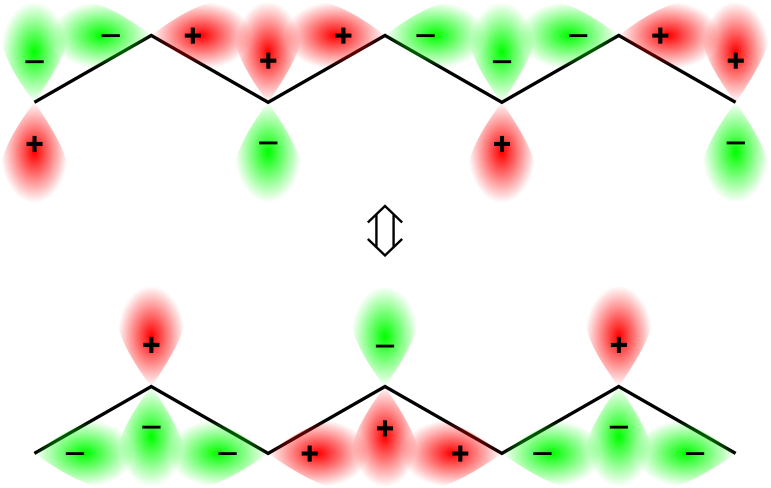

Figure 4.19: Depiction of the p-orbital nature of the wavefunctions of $BiZnSiO_4$ at T. Neighboring Bi sites interact in a way that can be depicted as chains of Bi p-orbitals running through an insulating structure, in which individual chains are analogous to polyacetylene; nonsymmorphic operation of "inversion followed by translation between A sites" results in an equivalent but different state, creating a twofold degeneracy at the Dirac point, which then becomes fourfold due to the spin degree of freedom. Breaking inversion symmetry in this structure is analogous to having inequivalent coupling constants between Bi sites and single and double bonds in polyacetylene, and will lift the degeneracy, gapping the system.

Chapter 5

Fermi surface of tensile-strained zincblende lattice

The zincblende lattice is a lower symmetry analog of the diamond lattice. Diamond consists of identical atoms on interpenetrating FCC lattices, whereas zincblende consists of distinct atoms on the two FCC lattices. HgTe and CdTe are well known examples of materials which take the zincblende structure. HgTe is a zero band-gap zincblende semiconductor with an inverted ordering of states at Γ (Madelung et al., 2010), where the band gap and inversion can be controlled by alloying with CdTe. HgTe and CdTe are both zincblende materials, with the crucial difference that the stronger spin-orbit coupling of Hg causes the states at Γ to invert relative to each other. Therefore HgTe/CdTe quantum wells exhibit the quantum spin Hall effect (Bernevig et al., 2006).

The electronic properties of alloys of HgTe have been studied extensively for many decades. HgTe is relevant to a discussion of Dirac semimetals because it is 'almost' a Dirac semimetal. The elsewhere gapped band structure of HgTe exhibits a point-like fourfold degeneracy at Γ between conduction and valence bands (Fig. 5.1). The bands disperse linearly in two directions away from Γ and quadratically in the third (Madelung et al., 2010; Dresselhaus, 1955; Zaheer et al., 2013). Thus, HgTe cannot be described by a three dimensional Dirac Hamiltonian at the Fermi level. In this Chapter, we address three questions. First, given that HgTe is almost a Dirac semimetal, is it possible to write down a small perturbation to the Hamiltonian that

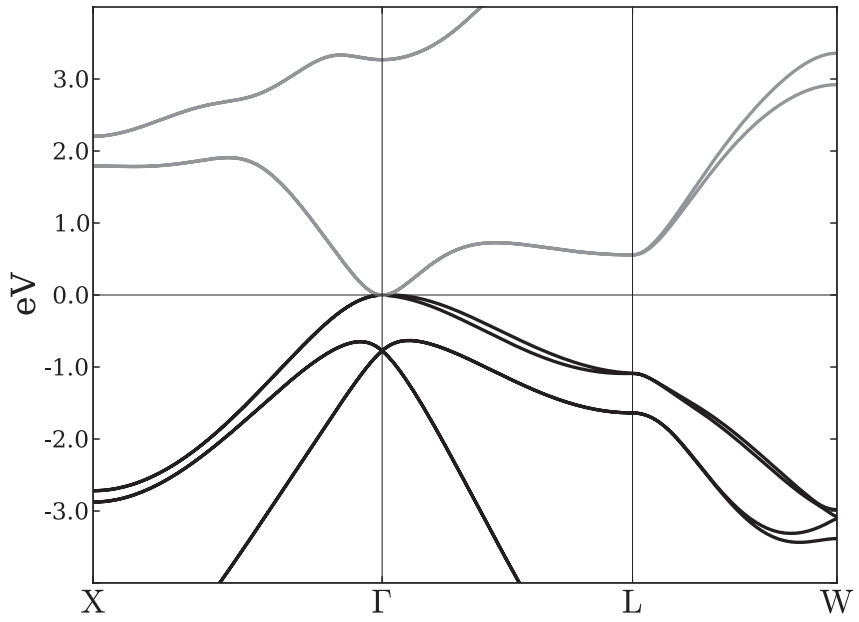

Figure 5.1: Band structure of HgTe as a function of crystal momentum across the entire Brillouin zone. The valence and conduction bands are gapped everywhere except near Γ.

might turn the fourfold degeneracy at Γ into a Dirac point? Second, what consequences can symmetry breaking perturbations have on the Fermi surface of HgTe? and third, what is the nature of states on the Fermi surface?

5.1. Representations of the zincblende lattice

We apply the symmetry criteria developed in Chapter 2 to the representations of spacegroup 216 (zincblende). Zincblende exhibits a FDIR R_8 of the abstract group G_{48}^{10} at Γ, which carries the largest symmetry within the BZ of the FCC lattice system to which zincblende belongs. The symmetry group at Γ is T_d, the tetrahedral group with mirror planes. The double cover of T_d is generated by $\{S_{4x}^{-}|000\}, \{\bar{C}_{31}^{-}|000\}$, and $\{\sigma_{db}|000\}$ where S_{4x}^{-} is a fourfold rotation reflection about the x-axis, $\bar{C}_{31}^{-}$ is a

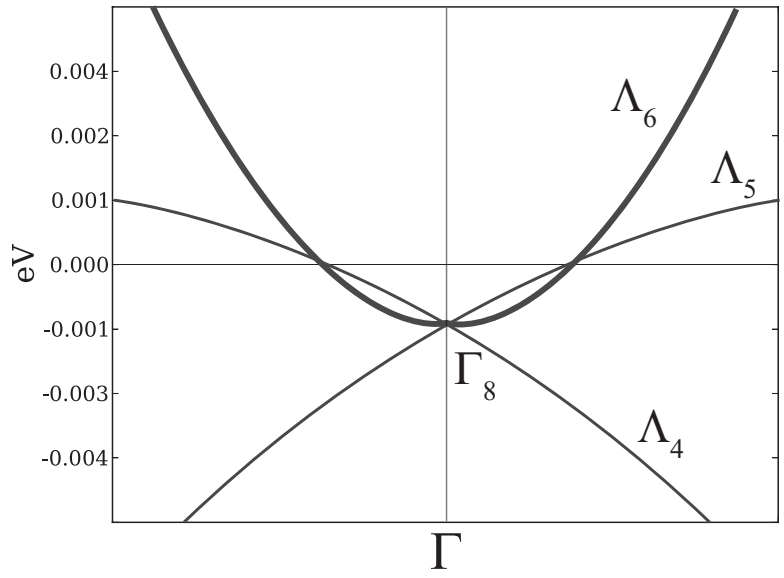

Figure 5.2: Energy bands near the Fermi level as a function of momentum along the (111) axis. At Γ the four degenerate states span the irreducible representation Γ_8 of the group T_d. $\Lambda_{4,5,6}$ are irreducible representations of the group C_{3v}. The twofold degenerate (solid) band labeled Λ_6 disperses quadratically to lowest order, whereas the nondegenerate bands Λ_4 and Λ_5 disperse linearly. There are threefold accidental degeneracies at $\mathbf{k} = \pm 0.004(1,1,1)$ because the bands Λ_4 and Λ_5 have negative mass, whereas Λ_6 has positive mass.

threefold rotation about one of the four axes of a regular tetrahedron, and $\sigma_{\rm db}$ is a mirror symmetry about one of the six edges of a regular tetrahedron.

We have shown explicitly in Section 2.3 that the point group T_d combined with time reversal symmetry places too many constraints on the Dirac matrices to allow a term in the Hamiltonian proportional to $\mathbf{k}$ in all three directions. The Chern number test described in Section 2.1 also prohibits the existence of a Dirac point with zero Chern number in the presence of time reversal symmetry. Finally, since Γ lies inside the BZ and zincblende is a symmorphic lattice, there is no perturbative way to turn HgTe into a Dirac semimetal. Although tuning a phenomenological parameter continuously can move the degeneracy at Γ to the surface of the BZ, there is not enough symmetry in the interior of the BZ to guarantee that the fourfold degeneracy will remain intact.

Furthermore, the only way to maintain a fourfold degeneracy at the zone face is to introduce sublattice symmetry which requires making both sublattices identical. This can be achieved by replacing Hg atoms with Te or vice versa. Neither changes are perturbative. Therefore, we conclude that zincblende cannot be a Dirac semimetal.

The band structure of HgTe has another unique feature around the fourfold degeneracy. The FDIR R_8 at Γ combined with the vector representation of T_d passes the Kronecker product test discussed in Section 2.4. However, time reversal and mirror symmetry guarantee that the FDIR split in a way depicted in Fig. 2.3(c) to linear order in $\mathbf{k}$ along the axis of threefold symmetry that lies in a mirror plane. Figure 5.2 shows the band structure of HgTe around Γ along a threefold axis ((111)-axis in this case). The bands labeled Λ_5 and Λ_4 disperse linearly to leading order in $\mathbf{k}$ along the (111) axis whereas the twofold degenerate band Λ_6 disperses quadratically. Microscopic features dictate that the bands Λ_4 and Λ_5 have negative mass while Λ_6 have positive mass. Consequently, in addition to the fourfold $p_{3/2}$ quadruplet at Γ, we find threefold degenerate *accidental* band crossings between Λ_6, Λ_4, and Λ_5 away from Γ. These crossings occur extremely close to Γ at $\mathbf{k} = \pm 0.004(1, 1, 1)$ in units of π/a where a is the lattice constant, so the Fermi surface is effectively point-like.

5.2. Symmetry breaking in zincblende and Fermi surface

We consider the effects of symmetry breaking perturbations on the accidental degeneracies in HgTe. Fu and Kane (2007) predicted that compressive strain along the (111) axis will gap HgTe into a topological insulator since the states at Γ are already inverted (Fig. 5.3). The inverted ordering of bands at Γ is a direct consequence of spin-orbit coupling. To understand how it comes about, we compare the ordering of states in HgTe with and without spin (Fig. 5.5). At the Fermi level in spinless

HgTe, the valence states span a p-type representation Γ_4 of space group 216. Slightly above Γ_4 in energy, there exists an s-type band which belongs to the symmetric representation Γ_1. When spin-orbit coupling is introduced, the representation Γ_4 splits into a $p_{3/2}$-type representation Γ_8 and a $p_{1/2}$-type representation Γ_7, whereas Γ_1 turns into an $s_{1/2}$-type representation Γ_6. Since Hg is a heavy atom, its contribution to the spin-orbit coupling is strong enough to push the $s_{1/2}$-type band Γ_6 below Γ_8, resulting in an inverted band structure. This is in contrast with a normal ordered zincblende semiconductor (e.g. CdTe), where Γ_6 appears above Γ_8 in energy. Therefore, if Γ_8 is split and the inversion of Γ_6 relative to the split band Γ_8 is controlled by a "mass" parameter, the insulating phases that ensue have a non-trivial $\mathbb{Z}_2$ index $+1$ in the inverted regime, versus a trivial index 0 in the normal regime (Bernevig et al., 2006). The splitting of Γ_8 was achieved in a HgTe/CdTe quantum well structure, where the tuning of Γ_6 above or below the split representation Γ_8 was controlled by the well thickness, leading to the first experimental observation of the quantum spin Hall effect (Konig et al., 2007).

While compressive strain along the (111) axis gaps the system entirely (Fig. 5.3), tensile strain along the same axis shifts the accidental degeneracies further along the (111) axis after splitting Γ_8 (Fig. 5.4). Tensile strained HgTe remains a semimetal where the dispersion of bands around the accidental degeneracies is linear in all directions (Fig. 5.6). But there is a caveat. Each accidental degeneracy involves *three* states so it is neither a Dirac point nor a Weyl point. As discussed earlier, this is due to the presence of mirror symmetry about a plane that contains the (111) axis. If we could break the mirror symmetry, the twofold degenerate band in Figure 5.2 would split and the system will develop two Weyl points (Fig. 5.7).

A Weyl point carries a nonzero Chern number (charge) ± 1 and cannot be annihilated

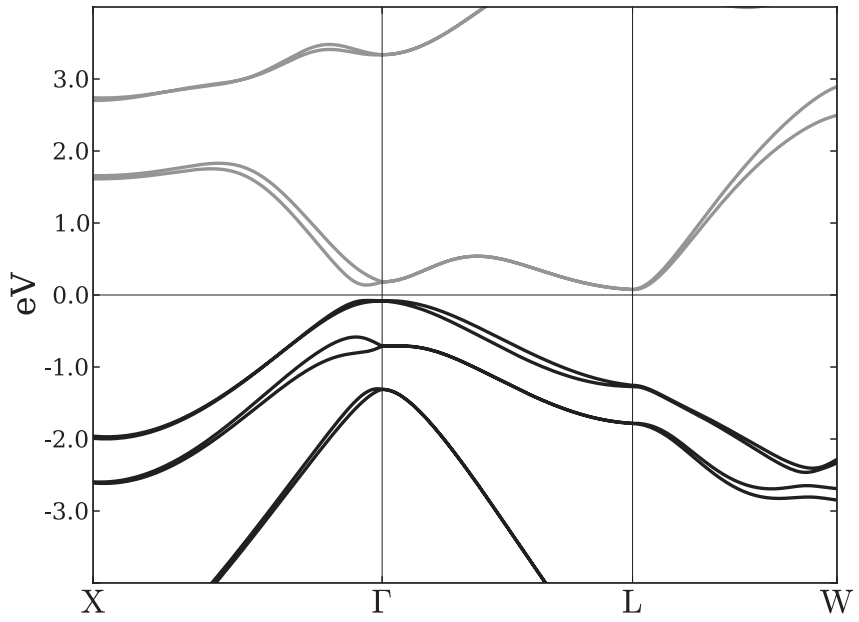

Figure 5.3: Band structure of HgTe under compressive strain along the (111) axis. The fourfold degenerate representation Γ_8 is split, and the material becomes a topological insulator (Fu and Kane, 2007).

unless brought in contact with another Weyl point of opposite charge. In other words, the spin texture of valence states around a Weyl point has nonzero divergence; if interpreted as a magnetic field, the spin texture would correspond to a magnetic monopole with charge ± 1. Mirror symmetry prohibits the existence of Weyl points on the mirror plane because the integral of the normal component of spins on a closed surface that encloses points on a mirror plane must be zero.

This has important implications for the Fermi surface of tensile strained HgTe (Fig. 5.6). The two Fermi ellipsoids contact at a point due to mirror symmetry. They can be separated only if mirror symmetry is broken. Consequently their corresponding spin textures will develop a nonzero divergence. We ask the following: what is the nature of the spin texture on the ellipsoidal Fermi surface *before* mirror symmetry is broken.

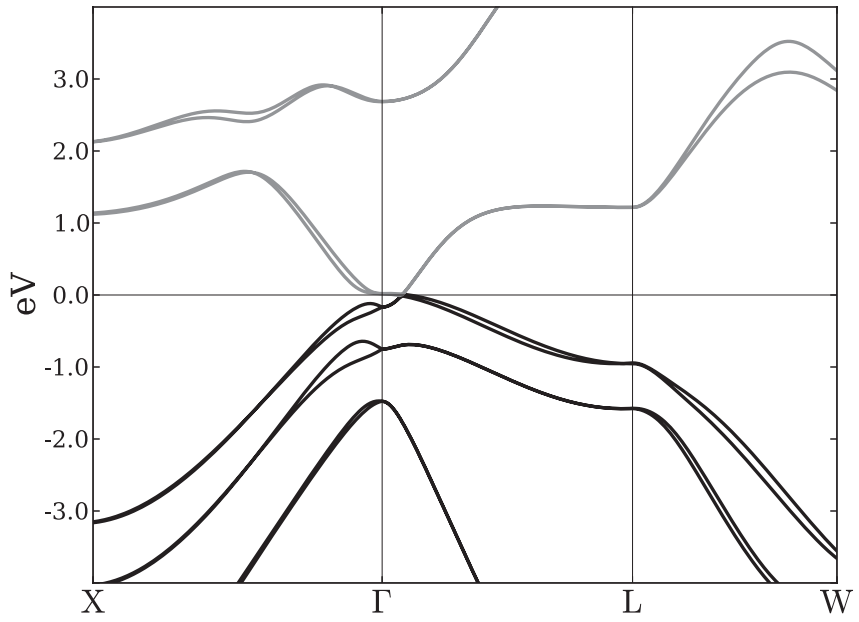

Figure 5.4: Band structure of HgTe under tensile strain along the (111) axis. Although Γ_8 splits under tensile strain as well, the accidental degeneracy along the (111) axis shifts away from Γ and the material remains semimetallic.

It turns out that spin texture on both ellipsoids is locked in a plane perpendicular to the (111) axis and exhibits a nonzero winding number around that axis. Furthermore the winding number changes as one sweeps across the Fermi ellipsoids from one end to the other and inevitably exhibits spin singularities on the Fermi surface where the winding number must change (Fig. 5.8). We make this point more precise by developing an effective $\mathbf{k} \cdot \mathbf{p}$ theory around the threefold accidental degeneracies and calculating the spin texture explicitly. Our analysis is supported by identical results on a microscopic level based on density functional theory calculations of the band structure and Fermi surface spin texture of $Hg_{0.5}Zn_{0.5}Te$. This material is designed by alloying HgTe and ZnTe to achieve the requisite tensile strain.

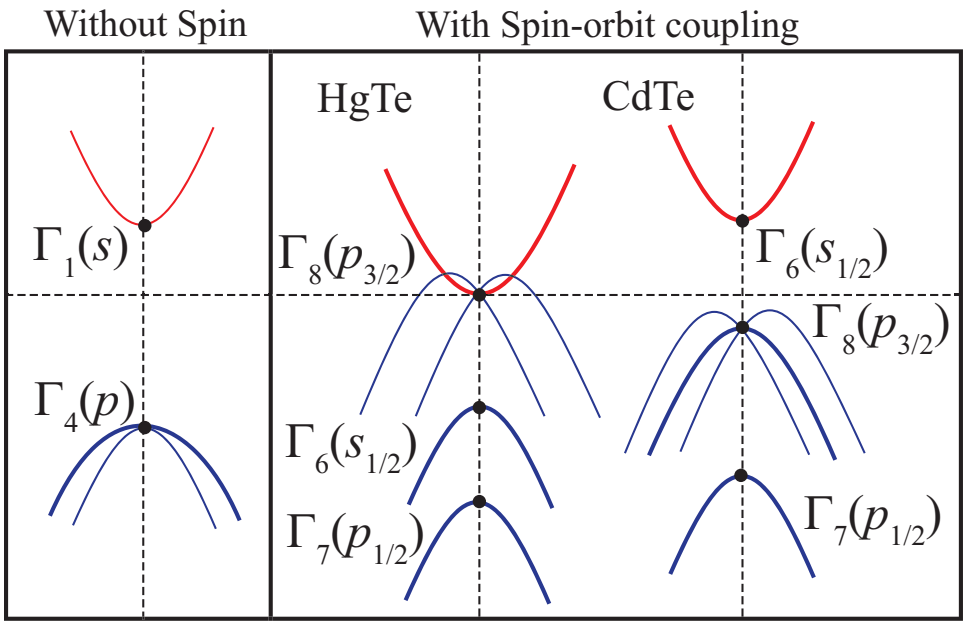

Figure 5.5: Band inversion due to spin-orbit coupling in HgTe.

5.2.1. Spin texture from $\mathbf{k}\cdot\mathbf{p}$ *theory*

We describe the states that span the representations Λ_4, Λ_5 and Λ_6 along the (111) axis in terms of a four band $\mathbf{k}\cdot\mathbf{p}$ theory around the accidental degeneracies. The states $|p, \pm\frac{3}{2}\rangle$ span the band Λ_6 whereas $|p, \pm\frac{1}{2}\rangle$ states span Λ_4 and Λ_5. The symmetry group C_{3v} along the (111)-axis is generated by $\{\mathrm{C}_{31}^{+}, \sigma_{\mathrm{db}}\}$ where C_{31}^{+} represents threefold rotation about the (111)-axis while σ_{db} represents mirror reflections about a plane containing the (111)-axis. Points where the accidental degeneracies occur are related by time reversal symmetry. The time reversal operator Θ maps the $\mathbf{k}\cdot\mathbf{p}$ Hamiltonian around $\mathbf{k}_0$ to its time reversed partner around $-\mathbf{k}_0$.

We choose an angular momentum basis for the $\mathbf{k}\cdot\mathbf{p}$ theory. The generators $\vec{J}$ of rotations for $p_{3/2}$ quadruplets were derived in Section 2.3. If we orient the k_z-axis along the (111) axis, the symmetry operators take the form $\mathrm{C}_{31}^{+} = \exp(\mathrm{iJ_z}2\pi/3)$ and $\sigma_{db} = i\tau_2\sigma_1$. We model the broken inversion symmetry in zincblende by adding a term

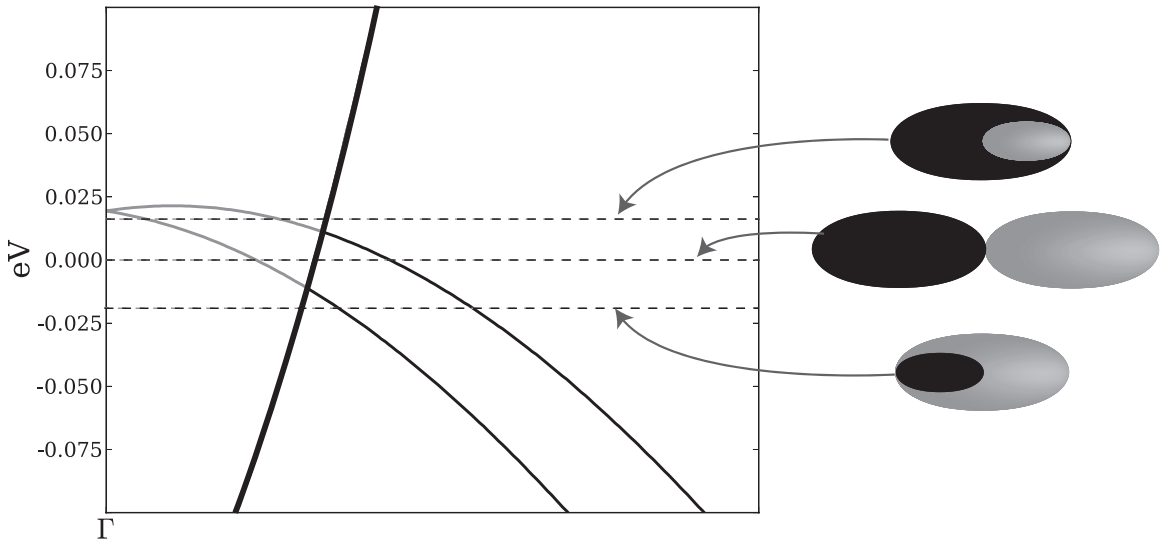

Figure 5.6: Band dispersion in tensile strained HgTe at the Fermi level as a function of momentum along the (111) axis. The twofold degenerate band (drawn as a thick line) is accidentally degenerate with both the nondegenerate bands (drawn as thin lines) within a very small energy range. Band dispersion around the accidental degeneracies is linear to leading order in the (111) direction. Right: Schematic illustration of the Fermi surface. The Fermi surface for various choices of Fermi energy (drawn in dashed lines) near the accidental degeneracies consists of two ellipsoids which contact at a point. This indicates that the bands disperse linearly in transverse directions as well around the accidental degeneracies.

κ to the Hamiltonian which does not commute with the local antiunitary operator operator $\mathcal{P}\Theta$ where $\mathcal{P}$ represents inversion symmetry. $\mathcal{P}\Theta$ is local because both $\mathcal{P}$ and Θ send $\mathbf{k}$ to $-\mathbf{k}$. In the angular momentum basis, it can be written as $\mathcal{P}\Theta = i\tau_x\sigma_y\mathrm{K}$, where K is the complex conjugation operator.

A Hamiltonian linear in $\mathbf{k}$ which respects the symmetries of the (111) axis is,

$$\mathcal{H}(\mathbf{k}) = k_x\tau_x + k_y\tau_y + k_z\tau_z\sigma_z + \kappa \tag{5.1}$$

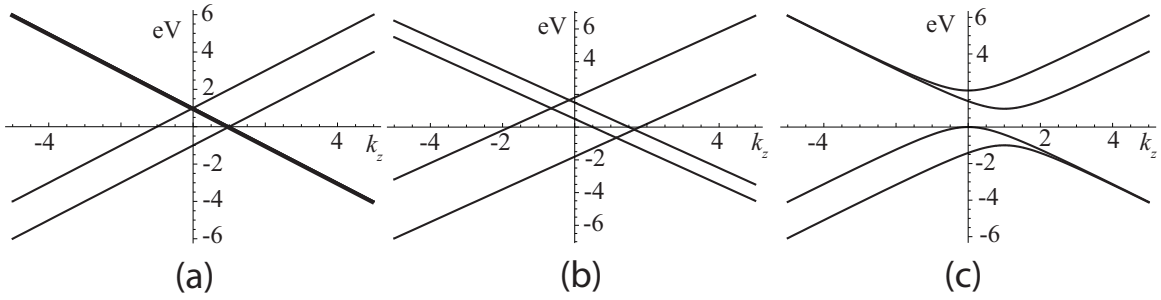

Figure 5.7: (a) Energy bands plotted as a function of momentum in the k_z direction in the $\mathbf{k} \cdot \mathbf{p}$ theory. There is a twofold degenerate band (thick line) intersecting two nondegenerate bands (thin lines) analogous to Figure 5.6. (b) Mirror and time reversal symmetry breaking perturbation proportional to J_z splits the twofold degenerate band into two nondegenerate bands, giving rise to four Weyl points. (c) Rotation and mirror symmetry breaking perturbation proportional to $\tau_z \sigma_x$ gaps the system entirely.

where

$$\kappa = \begin{pmatrix} 0 & 0 & 0 & -i \\ 0 & 1 & 0 & 0 \\ 0 & 0 & 1 & 0 \\ i & 0 & 0 & 0 \end{pmatrix}.$$

With this choice of κ, time reversal symmetry is preserved while inversion is broken if we require that $\Theta \mathcal{H}(\mathbf{k}) \Theta^{-1} = \tau_x k_x + \tau_y k_y + \tau_z \sigma_z k_z + \kappa^T$ is the effective $\mathbf{k} \cdot \mathbf{p}$ Hamiltonian around the time reversed location of the accidental degeneracies. Such a constraint is allowed because the $\mathbf{k} \cdot \mathbf{p}$ theory is localized around a Brillouin zone momentum $\mathbf{k}_0 \neq 0$ along the (111) axis.

Figure 5.7 shows the energy spectrum of the Hamiltonian in Eq. (5.1) along the k_z axis. The degenerate band Λ_6 splits to give four Weyl points under a mirror and time reversal symmetry breaking Zeeman term proportional to σ_z or J_z where J_z is the angular momentum operator of $p_{3/2}$ states. Figure 5.7(b) shows the splitting of Λ_6 to

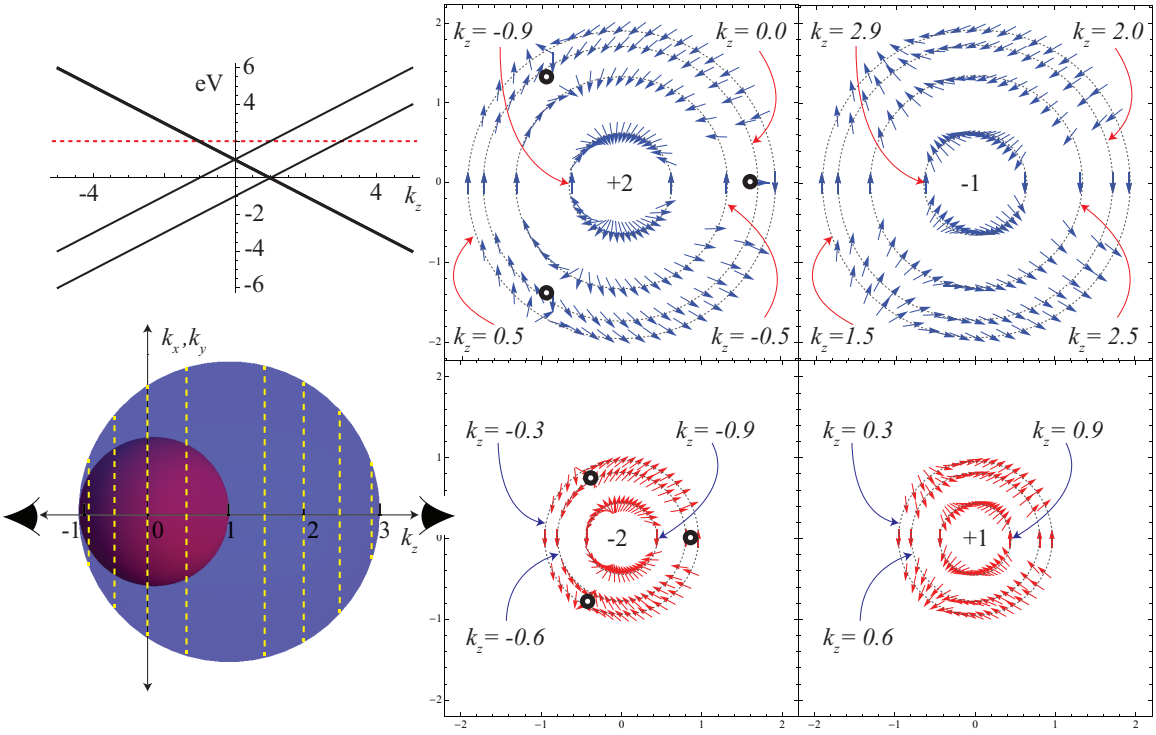

Figure 5.8: Spin texture on the Fermi surface of tensile strained HgTe as predicted by the $\mathbf{k}\cdot\mathbf{p}$ theory of Eq. (5.1). Top Left: Band dispersion in the $\mathbf{k}\cdot\mathbf{p}$ theory as a function of momentum along the (111) axis. The Fermi level $\mathcal{E}_F$(dashed line) is set to be 2 eV in the units of Eq. (5.1). Bottom Left: The Fermi surface for $\mathcal{E}_F = 2$ eV at the $\mathbf{k}\cdot\mathbf{p}$ level consists of two spherical shells which touch at the point $k_z = -1$. Top Right: The spin texture of valence states on the blue Fermi spherical shell as a function of momentum in the k_x, k_y plane. Each circle corresponds to a constant k_z (indicated by dashed yellow lines cutting through the Fermi surface on the left). Bottom Right: The spin texture of valence states on the red Fermi spherical shell as a function of momentum in the k_x, k_y plane. The spins are locked in the k_x, k_y plane for both Fermi shells. The winding number of spins on each Fermi shell changes as one moves from one end along k_z to the other. There are three points indicated in yellow where the spin texture vanishes. The spin winding number flips from ± 2 to ∓ 1 at these spin singular points.

give four Weyl points due to a perturbation proportional to J_z. A rotation and mirror symmetry breaking perturbation such as $\tau_z\sigma_x$ gaps the system entirely [Fig. 5.7(c)].

It is possible to split Λ_6 into two parallel bands as in Figure 5.7(b) by a mirror preserving term $\tau_y\sigma_x$ which breaks time reversal and rotation symmetry. This, however, does not lead to Weyl points; even though the degeneracies involve two states, the bands develop a quadratic dispersion in one direction. Mirror symmetry about a plane constrains all points $\mathbf{k}$ on the plane to have zero Chern number. This is explained as follows: The Chern number of a certain point $\mathbf{k}$ in the Brillouin zone is given by an integer $n = 1/(2\pi i)\oint_S \mathrm{Tr}\vec{\mathcal{F}}\cdot\hat{n}$ where $\vec{\mathcal{F}}_{ij} = \nabla_{\mathbf{k}} \times \langle\psi_i|\nabla_{\mathbf{k}}|\psi_j\rangle$ is the Berry curvature, $\hat{n}$ is a unit vector normal to the surface S that contains $\mathbf{k}$, and the trace includes only valence states $|\psi_i\rangle, i = 1, ..N$. A mirror symmetry about a plane that contains $\mathbf{k}$ reverses the orientation of the surface S while the integrand is the same for opposing points on S. Hence the Chern number of all points on a mirror plane must be zero. Therefore, as long as mirror symmetry is present, tensile strained HgTe cannot host Weyl points along the (111) axis.

The Fermi surface consists of two spheres in $\mathbf{k}$ space parametrized as, $S_1 : \ \mathcal{E}^2 = k_x^2 + k_y^2 + (1 - k_z)^2$ and $S_2 : \ (\mathcal{E} - 1)^2 = k_x^2 + k_y^2 + k_z^2$ where $\mathcal{E}$ is the Fermi energy. The average spin field is given by $\langle\psi_i|\hat{\mathbf{S}}|\psi_i\rangle$ where $|\psi_i\rangle$ is a valence state on one of the Fermi ellipsoids parametrized by $\mathcal{E}$ and $\hat{\mathbf{S}}$ is the spin operator for the $p_{3/2}$ states. In the $\mathbf{k}\cdot\mathbf{p}$ theory, this evaluates to,

$$\langle\hat{\mathbf{S}}\rangle_i = \alpha_i(\mathcal{E}, k_z)\left[\sin(\theta)\,\hat{\mathbf{i}} + \cos(\theta)\,\hat{\mathbf{j}}\right] + \beta_i(\mathcal{E}, k_z)\left[\sin(2\theta)\,\hat{\mathbf{i}} - \cos(2\theta)\,\hat{\mathbf{j}}\right] \tag{5.2}$$

where the subscript $i = 1, 2$ identifies one of the Fermi ellipsoids S_i and θ is the azimuthal angle in the k_xk_y plane that parametrizes the ellipsoids. The coefficients

α_i, β_i are,

$$\alpha_1(\mathcal{E}, k_z) = -\sqrt{\frac{4(\mathcal{E}+1-k_z)}{3(\mathcal{E}-1+k_z)}}\ , \beta_1(\mathcal{E}, k_z) = -\frac{\alpha_1(\mathcal{E}, k_z)^2}{2}$$
$$\alpha_2(\mathcal{E}, k_z) = \sqrt{\frac{4(\mathcal{E}-1-k_z)}{3(\mathcal{E}-1+k_z)}}\ , \beta_2(\mathcal{E}, k_z) = \frac{\alpha_2(\mathcal{E}, k_z)^2}{2}$$

The three mirror planes of the group C_{3v}, all of which contain the k_z axis, lock the spin expectation values in the $k_x k_y$ plane. Figure 5.8 shows how the spin texture evolves as a function of k_z around the Fermi ellipsoids. For fixed $\mathcal{E}$, k_z ranges between $1-|\mathcal{E}|$ and $1+|\mathcal{E}|$ on S_1 and between $-|1-\mathcal{E}|$ and $|1-\mathcal{E}|$ on S_2. When k_z is close to $1-\mathcal{E}$ on either ellipsoid, the term with the coefficient β_i dominates and the spin winding number is -2, whereas when k_z is close to $\mathcal{E}+1$ on S_1 or $\mathcal{E}-1$ on S_2 the term with the coefficent α_i dominates, and the spin winding number is $+1$. Therefore, the spin winding number must change abruptly from one end of the Fermi ellipsoids to the other, since the spins cannot develop a component in the k_z direction due to mirror symmetry. Hence, there must exist singular points on the Fermi ellipsoids where the spin expectation values vanish. Figure 5.8 shows the points on the Fermi ellipsoids where the spin expectation value goes to zero. There are three such singular points which are related by threefold symmetry, and their exact location on the Fermi surface can be calculated in $\mathbf{k}\cdot\mathbf{p}$ theory. Note that although the α_i diverge in the limit $k_z \to 1-\mathcal{E}$, the points where $k_z = 1-\mathcal{E}$ correspond to the degenerate band Λ_6, and since α_1, β_1 and α_2, β_2 have opposite signs, the total spin $\langle\hat{\mathbf{S}}\rangle_1 + \langle\hat{\mathbf{S}}\rangle_2 = 0$ for states in Λ_6.

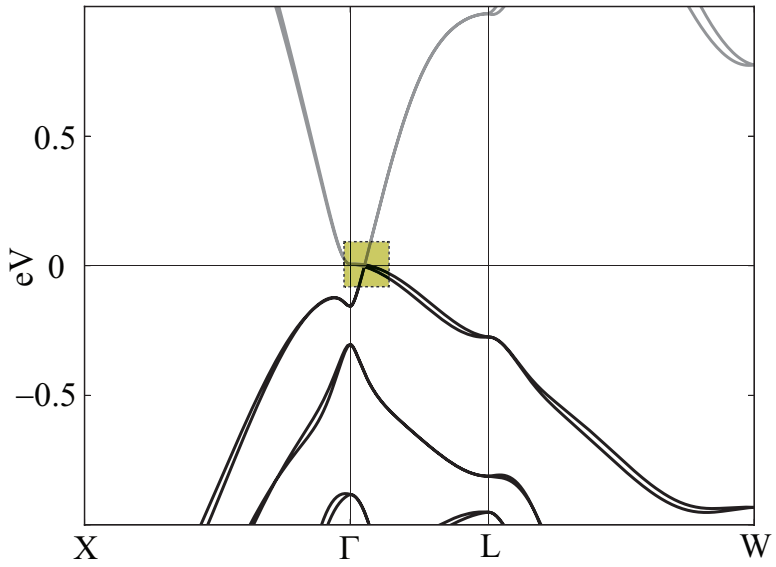

Figure 5.9: Band structure of $Hg_{0.5}Zn_{0.5}Te$ is the same as tensile strained HgTe (Fig. 5.4) except the shape and size of the Fermi surface and the Fermi velocities in the two materials.

5.2.2. Spin texture at the microscopic level

Figure 5.6 shows the band structure along the (111) direction for 8% tensile strain in HgTe. The set of momenta corresponding to a fixed energy form two ellipsoidal surfaces that contact at a point. This implies that the bands Λ_4, Λ_5 and Λ_6 disperse linearly in all directions around the accidental degeneracies. Therefore, under tensile strain the Fermi surface of HgTe grows from a point to a set of four ellipsoids, in two sets of Kramers paired momenta in the Brillouin zone. The two ellipsoids on one side of Γ are connected to each other at the point $\mathbf{k}$ along the (111) axis where the Fermi level crosses the band Λ_6.

We note that 8% tensile strain corresponds to 4% strain in-plane, which is relatively large. This effect ensues as soon as a perturbation breaking the fourfold symmetry of zincblende turns on; there is no critical value of strain below which the unusual spin texture of the Fermi surface would disappear. While 8% tensile strain, which

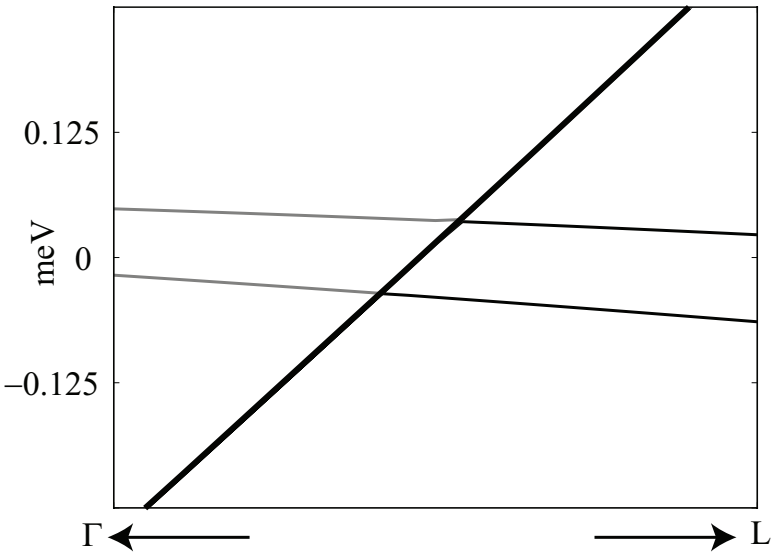

Figure 5.10: Band dispersion at the Fermi level near the accidental degeneracies along the (111) axis. There is a twofold degenerate band (thick line) intersecting two non-degenerate bands (thin lines), essentially identical to tensile strained HgTe (Fig. 5.6).

corresponds to 4% strain in-plane, is quite high, the ellipsoidal Fermi surfaces ought to be observable at reduced strains; at 2% tensile strain the energy difference between the threefold degeneracies is still 18meV, down from 25meV. Even so, very high strains may be achievable through epitaxial growth of HgTe on an appropriate substrate (Faurie et al., 1986).

Alternatively, strain can be introduced chemically. Alloying HgTe with ZnTe introduces a size mismatch between Hg and Zn, causing both Zn and Hg atoms to move off center toward a Te atom; if all the Zn atoms move in the same direction, the symmetry breaking is the same as that created by tensile strain. A similar effect has also been reported in $Cd_xZn_{1-x}Te$ (Weil et al., 1989), which shows rhombohedral distortions and Zn off-centering for a wide range of Zn concentration. Figures 5.9 and 5.10 show the band structure of ordered $Hg_{0.5}Zn_{0.5}Te$, which is qualitatively identical to strained HgTe. The difference lies in the shape and size of the Fermi surface and the Fermi velocities in the two materials.

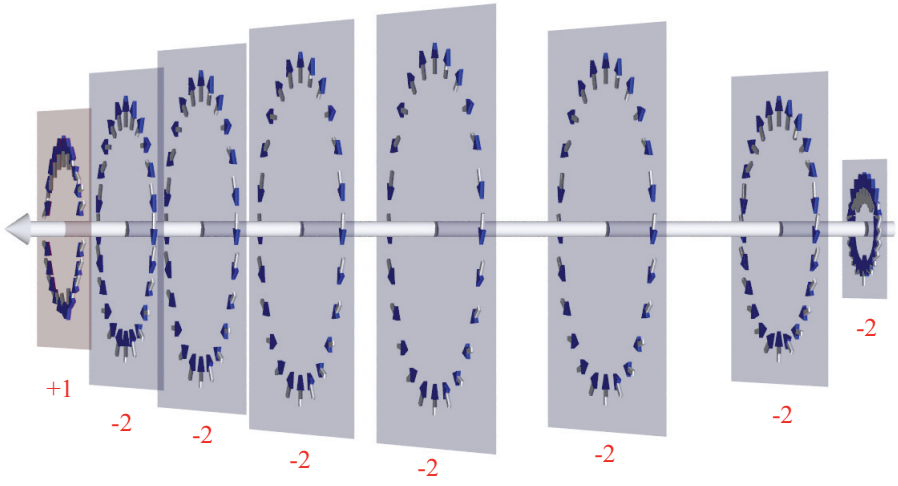

Figure 5.11: Spin texture on the Fermi surface of $Hg_{0.5}Zn_{0.5}Te$ at the *ab initio* DFT level. Spins on a Fermi surface ellipsoid of $Hg_{0.5}Zn_{0.5}Te$ are locked in the plane perpendicular to the (111) axis. The spin winding number around the (111) axis changes from +1 to -2 from the left end of the ellipsoid to the right end.

Ab initio calculations indicate that the spin texture on the Fermi surface of $Hg_xZn_{1-x}Te$ ($x = 0.5$) is locked in a two dimensional plane and exhibits spin singular points identical to tensile strained HgTe (Figs. 5.11 and 5.12). For visual clarity, the magnitude of all vectors is normalized in Figure 5.11, while in Figure 5.12 the size of each vector is set to equal the square root of its magnitude. However it is likely that Density Functional Theory (DFT) overestimates (Svane et al., 2011) the amount of band inversion for $x = 0.5$ given that $Hg_xCd_{1-x}Te$ is a band insulator for $x < 0.8$ (Scott, 1969), and $Hg_{0.5}Zn_{0.5}Te$ is likely to be gapped. However, calculations for $Hg_{0.75}Zn_{0.25}Te$ suggest that significant symmetry-breaking distortion persists for lower Zn concentration, consistent with the observations of similar behavior in $Cd_xZn_{1-x}Te$ (Weil et al., 1989). Nonetheless, for small enough concentrations of Zn, this symmetry protected spin texture may indeed by realized physically. It is difficult to span the full range

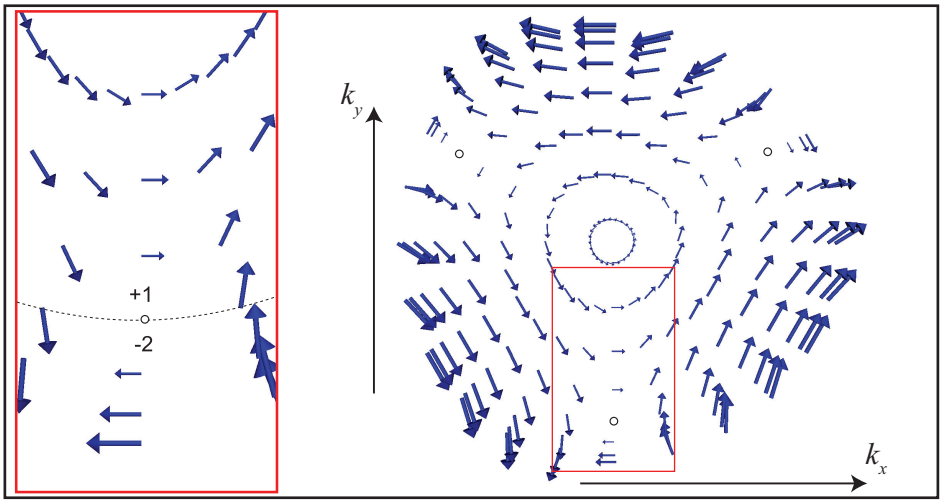

Figure 5.12: Spin texture in the two dimensional plane transverse to the (111) direction. Each concentric loop of spins corresponds to a fixed value of momentum along the (111) axis. The spin winding number around the (111) axis changes from the inner circles to the outer circles on the Fermi ellipsoid. Since spins are locked on the transverse plane, their winding number changes as they vanish at three rotation symmetry related singular points (drawn as white circles outlined in black). Left: A higher resolution image showing the change in the spin winding number from +1 to -2 as we move from the inner radii to the outer radii on the right.

of intermediate compositions within DFT to make a prediction of the composition where the inversion occurs. While some experimental studies have been performed on $Hg_{1-x}Zn_xTe$, it is difficult to draw any direct conclusions without more detailed structural characterization of the samples (Sher et al., 1986; Berding et al., 1987). We performed a phonon analysis of tensile strained HgTe and $Hg_{0.5}Zn_{0.5}Te$ and found no structural instability. Therefore, if some ordered compound $Hg_xZn_{1-x}Te$ exists with x such that distortion due to Zn substitution sufficiently splits the degeneracy at the Fermi level while still allowing band inversion, then it would possess an experimentally observable ellipsoidal Fermi surface. We assert that a time reversal and mirror symmetry breaking Zeeman field would split the degenerate band Λ_6 and turn $Hg_xZn_{1-x}Te$ into a Weyl semimetal. This is also confirmed by the $\mathbf{k}\cdot\mathbf{p}$ theory in Section 5.2.1.

Chapter 6

Conclusions and Outlook

We have studied the possibility of symmetry protected Dirac points in three dimensional solids on the basis of representations of spacegroups, and provided examples of realistic materials on the basis of microscopic calculations that exhibit Dirac points on the Fermi surface. Interest in the study of three dimensional Dirac points arises primarily from the exotic nature of the two dimensional Dirac points in graphene. Questions such as access to a variety of topological band insulators, high charge carrier mobility, nature of the magneto-electric and thermo-electric response functions, stability of Dirac points in the presence of lattice defects, impurities, and electron interactions are only but a few among a long list concerning the physics of Dirac points. Whereas this dissertation has focused on describing the underlying theory behind the existence of Dirac points, a number of authors have already reported significant progress on the various phenomenological questions relating to three dimensional Dirac semimetals. In this Chapter, we summarize their efforts and speculate about possible developments in the future.

Before discussing the phenomenology of Dirac semimetals, it is critical from an observational point of view to establish a clear experimental signature of bulk Dirac points. In general, bulk properties are inferred from surface effects, since it is much easier to observe the surface in a laboratory setting. Unlike topological systems, symmetry protected Dirac semimetals do not exhibit any topologically protected surface states (as described in Chapter 1). The absence of signature surface states makes symmetry protected bulk Dirac points hard to detect. Indirect tests consisting primarily of

tuning the Dirac point into a topological phase and then measuring the properties of the ensuing phase have been proposed. Even so, a direct experimental signature of bulk Dirac points is as yet unknown.

Experimental discovery of the topological Dirac semimetal Cd_3As_2 involved measurements of the in-plane energy dispersion on a particular cleaved surface using angle-resolved photoemission spectroscopy (ARPES) while the out-of-plane energy dispersion was resolved by varying incident photon energies (Neupane et al., 2014). The band velocity of the bulk Dirac spectrum was measured to be as high as 10eVÅ which appears to account for the high carrier mobility previously observed in Cd_3As_2 (Jay-Gerin et al., 1977; Zdanowicz et al., 1983). Photon-energy-dependent ARPES measurement techniques were also used to demonstrate the existence of a bulk three dimensional Dirac cone in Na_3Bi (Liu et al., 2014b) and independently in Cd_3As_2 (Borisenko et al., 2013). We speculate that symmetry protected Dirac points might also be observed using similar techniques.

Weyl semimetals exhibit topologically protected states on the surface which look like arcs in momentum space that originate from the surface projection of one Weyl point to that of its partner with opposite charge. Potter et al. (2014) have shown that the exposure of a Weyl semimetal to a magnetic field creates a chiral state that propagates electrons through the bulk into the surface and along the surface Fermi arcs. Thus, the magnetic field gives rise to closed magnetic orbits involving Fermi arc surface states and can be observed in quantum oscillations experiments. A Dirac point splits into pairs of Weyl points upon exposition to a magnetic field. Therefore, the nature of the propagating magnetic orbits can provide an indirect signature for detecting Dirac semimetals.

The dynamical conductivity of three dimensional Dirac semimetals is not disorder-

independent to leading order in the disorder strength as it is in graphene. Therefore, the usual mathematical difficulties in unambiguously resolving the role of disorder as the Fermi level approaches the Dirac point remain. Since the density of states at the Dirac point vanishes quadratically, it has been argued that weak disorder is perturbatively irrelevant for transport in Dirac/Weyl semimetals (Hosur et al., 2012; Abrikosov et al., 1965). On the other hand, a nonperturbative calculation for weak disorder shows that conductivity at the Dirac point might be dominated by electrons tunneling into rare regions of disorder (Nandkishore et al., 2014) and hence a nonvanishing density of states. This has led to speculation that there is no Dirac semimetal phase in the presence of weak disorder.

The stability of Dirac points in the presence of defects is another interesting question. Line defects can be modeled as magnetic flux vortices, so many results derived for bulk magnetic fields apply. Calculations performed by this author and others indicate the existence of a chiral state along the line defect (vortex) for a single Weyl point. We speculate that in the case of a Dirac point, there might be two counter-propagating chiral states because of the lack of directionality of a line defect as well as the fact that the Dirac point has zero Chern number. The counter-propagating chiral states could hybridize leading to a band gap along the defect line. This question is also yet to be addressed completely.

However, scanning tunneling microscopy measurements in the presence of strong magnetic fields on the topological Dirac semimetal Cd_3As_2 at sub-Kelvin temperatures have shown that lattice defects mostly influence the valence band (Jeon et al., 2014). This appears to provide an explanation for the existence of high mobility carriers in the conduction band of Cd_3As_2. We speculate that symmetry protected Dirac semimetals might also exhibit similar high mobility charge carriers and have techno-

logical applications. Jeon et al. (2014) report that the bulk Dirac point in Cd_3As_2 was observed indirectly by combining Landau level spectroscopy and quasiparticle interference to distinguish the splitting of the conduction band in terms of spin in the presence of a magnetic field and observing extended features of the Landau level spectrum due to the Dirac-like features of the bulk energy spectrum. These measurements also provide proof for the existence of Weyl points along the direction of a magnetic field as pointed out in Chapter 1.

As always in condensed matter physics, the introduction of electron-electron and electron-phonon interactions presents the possibility of a number of interesting phenomena. First, whether weak interactions have any other ramifications besides renormalizing the Fermi level, and second, to what extent does the Dirac point survive in the presence of strong interactions. Weyl semimetals have been shown to be unstable in the presence of strong short range interactions; for example, strong spin-orbit coupling has been shown to give rise to a chiral excitonic insulator in Weyl semimetals (Wei et al., 2012) which has a ferromagnetic order parameter whose phase determines the direction of the induced magnetic moment; general short range interactions give rise to a multitude of spin density waves in the ground state (Maciejko and Nandkishore, 2014); a mean field treatment for strong electron correlations and spin-orbit coupling has been shown to spontaneously break inversion and time reversal symmetries and give rise to a Weyl semimetal phase for a finite range of interaction parameters (Sekine and Nomura, 2013). On the other hand, long range Coulomb interactions have been found to preserve the Dirac semimetal phase when out-of-plane Fermi velocity anisotropy is weak, while for strong anisotropy the Dirac semimetal state turns into a Mott insulator (Sekine and Nomura, 2014).

Phonon interactions between Weyl points located at distinct momenta in the Brillouin

zone have been considered and shown to give rise to axion strings (Wang and Zhang, 2013) which can be understood as screw or edge dislocations along emergent charge density waves between the Weyl nodes. The axion strings carry a chiral mode that propagates from one Weyl point to the other in an otherwise gapped structure. The instability and coupling of Dirac points separated in momentum space (as in diamond) in the presence of phonons is not yet completely understood to our knowledge.

And finally, symmetry protected Dirac semimetals have yet to be observed experimentally. To that end, there is a need to study and design more realistic Dirac semimetals that can be synthesized in laboratory using existing techniques. We close this Chapter with the hope that future work will shed light on the various questions raised here and explore as yet unknown features of Dirac semimetals.

APPENDIX

Dirac Semimetal in Three Dimensions

S. M. Young,[1] S. Zaheer,[2] J. C. Y. Teo,[2,*] C. L. Kane,[2] E. J. Mele,[2] and A. M. Rappe[1]
[1]*The Makineni Theoretical Laboratories, Department of Chemistry, University of Pennsylvania, Philadelphia, Pennsylvania 19104-6323, USA*
[2]*Department of Physics and Astronomy, University of Pennsylvania, Philadelphia, Pennsylvania 19104-6396, USA*
(Received 13 December 2011; published 6 April 2012)

We show that the pseudorelativistic physics of graphene near the Fermi level can be extended to three dimensional (3D) materials. Unlike in phase transitions from inversion symmetric topological to normal insulators, we show that particular space groups also allow 3D Dirac points as symmetry protected degeneracies. We provide criteria necessary to identify these groups and, as an example, present *ab initio* calculations of β-cristobalite BiO_2 which exhibits three Dirac points at the Fermi level. We find that β-cristobalite BiO_2 is metastable, so it can be physically realized as a 3D analog to graphene.

DOI: 10.1103/PhysRevLett.108.140405 PACS numbers: 05.30.Fk, 31.15.−p, 71.20.−b

In a Dirac semimetal, the conduction and valence bands contact only at discrete (Dirac) points in the Brillouin zone (BZ) and disperse linearly in all directions around these critical points. In two dimensions, spinless graphene exhibits such pointlike degeneracies between the conduction and valence bands: the low energy effective theory at each of the critical points takes the Dirac form, $\hat{H}(\mathbf{k}) = v(k_x\sigma_x + k_y\sigma_y)$ where $\vec{\sigma} = \{\sigma_x, \sigma_y, \sigma_z\}$ are the Pauli matrices and $v \neq 0$ [1]. The existence of Dirac points near the Fermi level is responsible for many important properties of graphene such as high electron mobility and conductivity. However, these Dirac points are not robust because they can be gapped by a perturbation proportional to σ_z. Spin-orbit coupling doubles the number of states and gaps the Dirac points [2]; however, the splitting is very small because carbon is a light atom.

In 3D, the analogous (and slightly generalized) Hamiltonian is $\hat{H}(\mathbf{k}) = v_{ij}k_i\sigma_j$. Provided $\det[v_{ij}] \neq 0$, $\hat{H}(\mathbf{k})$ is robust against perturbations because it uses all three Pauli matrices. This Hamiltonian is called a Weyl Hamiltonian because it describes two linearly dispersing bands that are degenerate at a (Weyl) point. The robustness of a Weyl point can be quantified by the Chern number of the valence band on a sphere surrounding the point, which takes values $\mathrm{sgn}(\det[v_{ij}]) = \pm 1$. If a Weyl point occurs at some BZ momentum $\mathbf{k}$, time reversal (T) symmetry requires that another Weyl point occur at $-\mathbf{k}$ with equal Chern number. However, the total Chern number associated with the entire Fermi surface must vanish. Hence there must exist *two more* Weyl points of opposite Chern number at $\mathbf{k}'$ and $-\mathbf{k}'$. Inversion (I) symmetry requires that Weyl points at $\mathbf{k}$ and $-\mathbf{k}$ have opposite Chern number. Hence under both T and I symmetries, $\mathbf{k} = \mathbf{k}'$ and the effective Hamiltonian involves four linearly dispersing bands around $\mathbf{k}$. Such a Hamiltonian is called a Dirac Hamiltonian, and it is not robust against perturbations because there are additional 4×4 Dirac matrices that can be used to open a gap at the Dirac point.

The Fermi surface of a Dirac semimetal consists entirely of such pointlike (Dirac) degeneracies. 3D Dirac semimetals are predicted to exist at the phase transition between a topological and a normal insulator when I-symmetry is preserved [3,4] (Ref. [5] demonstrates such a Dirac point degenerate with massive bands). If either I or T symmetry is broken at the transition, a Dirac point separates into Weyl points and one obtains a Weyl semimetal [Fig. 1(c)]. The topological nature of Weyl points gives rise to interesting properties such as Fermi-arc surface states [6] and pressure induced anomalous Hall effect [7]. Recent proposals to design a Weyl semimetal have been predicated upon the existence of a parent Dirac semimetal which splits into a Weyl semimetal by breaking I [8] or T symmetry [9]. Reference [10] demonstrates the existence of bulk chiral fermions due to crystal symmetry in single space groups.

Dirac points that arise in a topological phase transition described above are accidental degeneracies. In general, two Weyl points with opposite Chern numbers annihilate each other unless their degeneracy is protected by additional space-group symmetry. Therefore, we ask if a Dirac point can arise as a result of a crystallographic symmetry. Indeed certain double space groups allow Dirac points at high symmetry points on the boundary of the BZ. As an example we present *ab initio* calculations of β-cristobalite BiO_2 [Fig. 2(b)] which exhibits Dirac points at three symmetry related X points on the boundary of the FCC BZ [Figs. 1(b) and 3(c)]. This system realizes a Dirac degeneracy first encountered in a tight-binding model of s states in diamond in Ref. [11] [the Fu-Kane-Mele (FKM) model]. In the absence of T symmetry, two Weyl points with equal Chern numbers can be degenerate due to a point group symmetry as shown in Ref. [12].

A 3D double space group must satisfy the following criteria to allow a Dirac point. It must admit four dimensional irreducible representations (FDIRs) at some point $\mathbf{k}$ in the BZ such that the four bands degenerate at $\mathbf{k}$ disperse

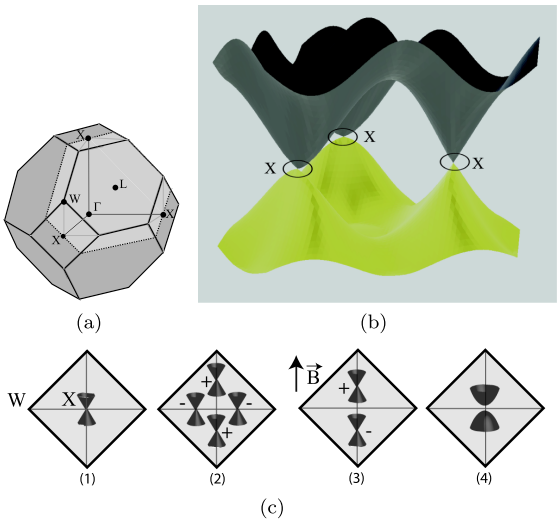

FIG. 1 (color online). 3D Dirac semimetal in β-cristobalite BiO_2. (a) Brillouin zone (BZ) of the FCC lattice. The plane highlighted in gray joins the three symmetry related X points. Other high symmetry points are also indicated. (b) Conduction and valence bands of β-cristobalite BiO_2 are plotted as functions of momentum on the plane highlighted in gray on the left. Each band is twofold degenerate due to inversion symmetry. Dirac points appear at the center of the three zone faces of the BZ. (c) Dirac, Weyl, and insulating phases in the diamond lattice. (1) The states at the Dirac point at X span a four dimensional projective representation of the little group at X which contains a fourfold rotation accompanied by a sublattice exchange operation. (2) Four Weyl points on the zone face due to a small inversion breaking perturbation. The Chern number of each Weyl point is indicated. (3) Two Weyl points appear on the line from X to W for a T-breaking Zeeman field $\mathbf{B}$ oriented along that direction. $\mathbf{B}$ oriented along other directions gaps all the Dirac points by breaking enough rotational symmetry that no two-dimensional representations are allowed. (4) Gapped phase obtained by breaking the fourfold rotation symmetry or by applying a magnetic field in any direction except along $\hat{x}$, $\hat{y}$, or $\hat{z}$. The insulating phase can be a normal, strong, or a weak topological insulator [11].

linearly in all directions around $\mathbf{k}$ and the two valence bands carry zero total Chern number. If the little group $G_{\mathbf{k}}$ at $\mathbf{k}$ contains a threefold or a sixfold rotation symmetry and the valence and conduction bands around $\mathbf{k}$ are nondegenerate, the Chern number of the FDIR is guaranteed to be nonzero. This rules out symmorphic space groups with FDIRs because they contain threefold rotations. This also rules out interior BZ momenta because nonsymmorphic little groups without threefold rotations exhibit FDIRs only on the boundary of the BZ [13]. To guarantee linear dispersion of bands around $\mathbf{k}$, the symmetric Kronecker product $[R_{\mathbf{k}} \times R_{\mathbf{k}}]$ of the FDIR with itself must contain the vector representation of $G_{\mathbf{k}}$ [14]. Finally, away from $\mathbf{k}$, the FDIR must split so that the valence and conduction bands are nondegenerate everywhere except at $\mathbf{k}$ (Fig. 4).

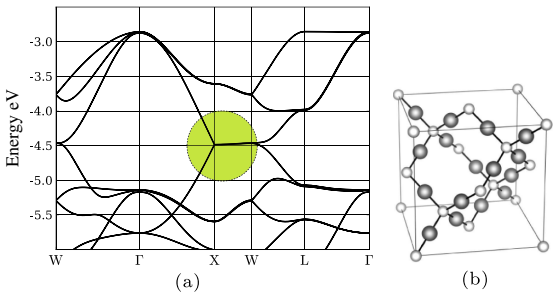

FIG. 2 (color online). (a) Band structure of β-cristobalite SiO_2. Energy bands are plotted relative to the Fermi level. Each band is twofold degenerate due to inversion symmetry. The (highlighted) FDIR at -4.5 eV is split into two linearly dispersing bands between X and Γ while the two degenerate bands along X and W are weakly split. This FDIR is buried deep below the Fermi level. (b) The β-cristobalite structure of SiO_2 (BiO_2). Silicon (bismuth) atoms (light gray) are arranged on a diamond lattice, with oxygen atoms (dark gray) sitting midway between pairs of silicon (bismuth).

We apply the above criteria to two important space groups. The space group of diamond (227, $Fd3m$), which is also the symmetry group of β-cristobalite BiO_2, exhibits FDIRs R_Γ at Γ and R_X at X. G_Γ contains threefold rotation symmetry and $[R_\Gamma \times R_\Gamma]$ does not contain the vector representation of G_Γ. Therefore the Γ point in a diamond lattice cannot host a Dirac point. R_X is a projective representation of G_X which does not have any threefold rotations because all the point group operations in G_X are those of the group D_{4h}. $[R_X \times R_X]$ contains the vector representation of G_X. Finally R_X splits into either two doublets or four singlets away from X [Figs. 4(a) and 4(b)]. Therefore the X point in space group 227 is a candidate to host a Dirac semimetal if its FDIR can be elevated to the Fermi level. Indeed, we show that β-cristobalite BiO_2 exhibits such a Dirac point at X, Fig. 3(c). The Dirac point at X in the FKM model is also spanned by states belonging to R_X [Fig. 3(d)].

The zinc blende lattice (space group 216, $F\bar{4}3m$) has a FDIR R'_Γ at Γ and the little group G'_Γ has a threefold rotation symmetry. $[R'_\Gamma \times R'_\Gamma]$ contains the vector representation of G'_Γ. Mirror symmetry in G'_Γ requires R'_Γ to split into a twofold degenerate representation and two nondegenerate representations along the (111) axis, which is also the symmetry axis for the threefold rotation. Time reversal symmetry requires that the twofold degenerate band remain flat along the (111) axis, Fig. 4(d). Thus the lowest band carries Chern number 0, while the two flat bands carry 1 and -1. Therefore the dispersion of R'_Γ is not Dirac-like along (111).

In HgTe, which takes the zinc blende lattice, the degenerate valence and conduction states at Γ span R'_Γ and constitute the entire Fermi surface. It is known that in HgTe the valence and conduction bands disperse linearly in two directions around Γ and quadratically in a third

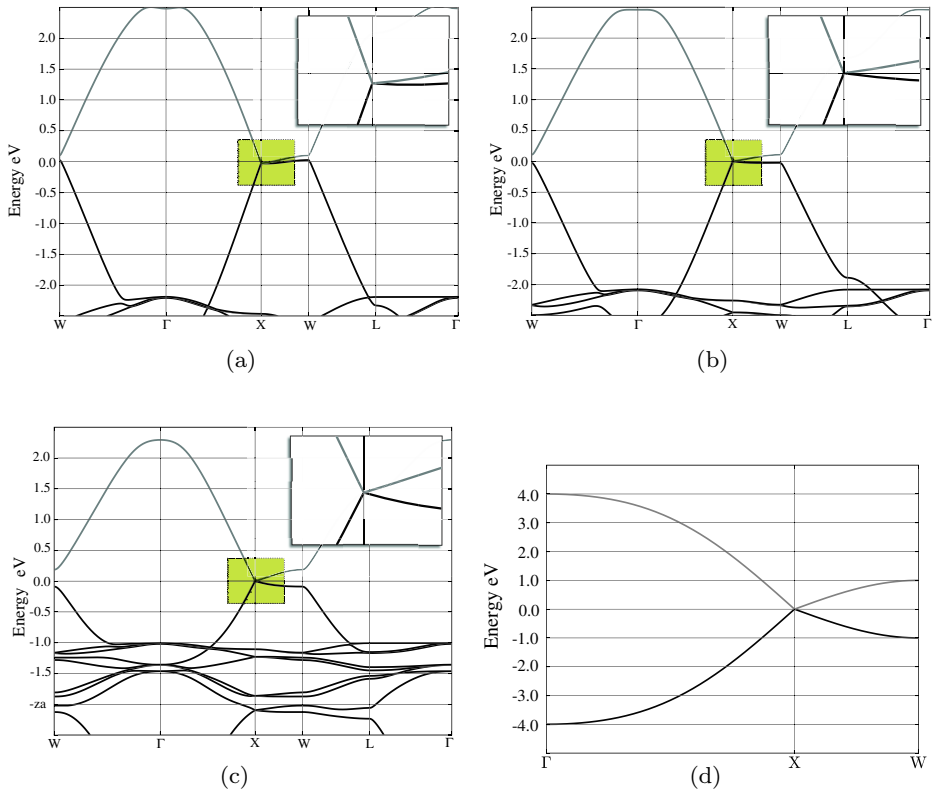

FIG. 3 (color online). Band structures of (a) AsO_2, (b) SbO_2, and (c) BiO_2 in the β-cristobalite structure, and (d) s states on a diamond lattice in the tight-binding model of Ref. [11]. Energy bands are plotted relative to the Fermi level. Each band is twofold degenerate due to inversion symmetry. Insets: with increasing atomic number of the cation, spin-orbit coupling widens the gap along the line V from X to W. In BiO_2 and SbO_2, the dispersion around the X point is linear in all directions indicating the existence of Dirac points at X. BiO_2 and SbO_2 are Dirac semimetals because their Fermi surface consists entirely of Dirac points.

[Fig. 4(d) and Ref. [15]]. One might ask if a perturbation might turn HgTe into a Dirac semimetal. However, the zinc blende lattice does not satisfy the criteria for 3D Dirac points as outlined above, so HgTe cannot host a Dirac semimetal. (a) Γ is an interior point of the BZ and the little group at Γ contains a threefold rotation. (b) Mirror symmetry requires two bands to be degenerate along the (111) axis but since the Chern number must vanish, the degenerate bands must be flat and consist of a conduction and a valence band. This is why we see quadratic dispersion along the (111) axis. (c) Breaking mirror symmetry splits the degenerate flat band but then the Fermi surface develops other non-Dirac-like pockets to compensate for the nonzero Chern number. (d) Breaking threefold rotation symmetry splits the degeneracy at Γ entirely and the material becomes a topological insulator [16].

We briefly discuss the theory behind the above criteria. We are interested in FDIRs of double space groups at points $\mathbf{k}$ such that the valence and conduction bands are distinct in a small region around $\mathbf{k}$ and carry zero total Chern number. The Chern number of a degenerate representation can be determined up to an integer by the rotation eigenvalues of the valence bands. Electron states spanning a FDIR are equivalent to a $p_{3/2}$ quadruplet exhibiting eigenvalues $e^{\pm i3\pi/n}$, $e^{\pm i\pi/n}$ for a $2\pi/n$ rotation symmetry. Rotation eigenvalues of states at time reversed momenta about the degenerate point are complex conjugates. Therefore the FDIR will carry Chern numbers ± 1 mod n for one valence band and ± 3 mod n for the other with total Chern number ± 4 mod n or ± 2 mod n for the FDIR. This is zero only for $n = 1, 2, 4$. If the conduction and valence bands are distinct in a small region around $\mathbf{k}$, the Chern number of the FDIR will be nonzero if the little group $G_{\mathbf{k}}$ contains a $2\pi/3$ or $2\pi/6$ rotation symmetry. In HgTe, however, the little group at Γ contains a threefold rotation symmetry but the FDIR at Γ has zero Chern number because one of the valence bands is degenerate with one of the conduction bands along the (111) axis.

Nonsymmorphic space groups contain point group operations coupled with nonprimitive lattice translations.

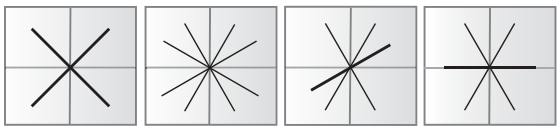

FIG. 4. Linear splitting of fourfold degenerate irreducible representations (FDIRs). If the symmetric Kronecker product of a FDIR with itself contains the vector representation of the group to which the FDIR belongs, it will split in one of the four possible ways displayed above. (a) The FDIR splits into two twofold degenerate bands. This situation is realized at the X point of the FCC Brillouin zone in a diamond lattice. (b) The FDIR splits into four nondegenerate bands. This situation arises at the Γ point in zinc blende if mirror symmetry is broken (although the FDIR in zinc blende develops a nonzero Chern number due to threefold rotation symmetry at Γ). (c) The FDIR splits into two nondegenerate and one twofold degenerate band with linear dispersion. (d) The splitting of the FDIR at Γ in zinc blende. The twofold degenerate band is constrained to be flat implying quadratic dispersion along that direction. The Chern number of this representation is zero in spite of a threefold rotation symmetry because the conduction and valence bands are degenerate away from Γ.

For example, inversion interchanges the FCC sublattices in the diamond space group. Representations of nonsymmorphic space groups at momenta inside the BZ momenta are obtained from regular representations, while those at the *surface* BZ momenta are obtained from *projective* representations of the associated crystal point group. The factor system of the projective representation is chosen to implement the required nonprimitive translation corresponding to the nonsymmorphic point group operation [13]. A theorem by Schur guarantees that projective representations of a group can be obtained by restricting to the group elements the regular representations of a larger group called the central extension group [13]. The central extension of a group is obtained by taking its product with another finite Abelian group. The important point to emphasize is that representations of nonsymmorphic space groups are obtained from representations of central extensions of the 32 point groups. Central extension groups exhibit FDIRs even without threefold rotations in the original point group. This is precisely why Dirac points can exist in 3D as symmetry allowed degeneracies.

To realize a Dirac-like dispersion in the vicinity of a FDIR, some of the matrix elements $\langle\psi_i|\mathbf{p}|\psi_j\rangle$, where $|\psi_i\rangle$ span the FDIR, must be nonzero. This is guaranteed if the symmetric Kronecker product of the FDIR with itself contains the vector representation of the central extension group to which the FDIR belongs [14]. We restrict to the symmetric part of the Kronecker product because matrix elements $\langle\psi_i|\mathbf{p}|\psi_j\rangle$ correspond to level transitions between states spanning the same representation [15]. Finally, the allowed representations in the vicinity of a FDIR should be such that each band disperses with nonzero slope in all directions. This is possible only if the valence band is distinct from the conduction band everywhere except at the Dirac point. Figure 4 illustrates the various possible ways in which a FDIR can split linearly.

Although crystallographic symmetries determine whether 3D Dirac points can exist, physical and chemical considerations dictate whether they arise at the Fermi level without additional non-Dirac-like pockets in the Fermi surface. In the FKM model, the Dirac point at X appears at the Fermi energy. However, in known materials on a diamond lattice s states appear below the Fermi energy. In realistic systems, additional orbitals hybridize with these s states and bands cross the Fermi level at other points besides X. The problem is especially severe in space group 227: without spin, the line V from X to W is twofold degenerate. With spin-orbit coupling, this line splits weakly for lighter atoms so the bands dispersing along this line can hybridize and introduce additional Fermi surface. Forcing species with s^1 valence states on the diamond lattice would fail to realize the FKM model. Indeed, *ab initio* calculations with group I elements and gold show that the splitting along V is insufficient to overcome this dispersion. In some cases, additional bands crossed the Fermi level. We performed *ab initio* calculations using the plane wave density functional theory package QUANTUM ESPRESSO [17], and designed nonlocal pseudopotentials [18,19] with spin-orbit interaction generated by OPIUM.

We consider derivatives of the diamond lattice that remain in space group 227. We place additional atoms in the lattice such that the configuration of added species allows its valence orbitals to either belong to the FDIR of interest, or appear away from the Fermi energy of the final structure. If the new species can split the nearby p states of the existing atoms away from the s levels, band crossing at the Fermi level can be avoided.

One such structure is β-cristobalite SiO_2 [Fig. 2(b)], which consists of silicon atoms on a diamond lattice with oxygen atoms placed midway along each silicon-silicon bond [20]. Oxygen atoms have two consequences: part of the O p shell strongly hybridizes with the Si p states, moving them away from the Si s states, while the remaining O p states span the same representation as the Si s states. A Dirac point can be realized by Si s-O p bonding/antibonding set of states. Figure 2(a) shows that the Si s-O p bands are present and take a configuration similar to the valence and conduction bands in the FKM model, but appear well below the Fermi energy. Additionally, the bands are nearly degenerate along the line V from X to W due to weak spin-orbit coupling.

Heavier atoms substituting Si both widen this gap and bring the FDIR of interest at X to the Fermi level. Figure 3 shows the band structures of compounds β-cristobalite MO_2, where $M = \mathrm{As/Sb/Bi}$. The change in chemical identity promotes the M s-O p fourfold degeneracy at X to the Fermi level, and stronger spin-orbit coupling widens

the gap along V. BiO_2 bears striking similarity to the FKM model, with linearly dispersing bands in a large energy range around a Dirac point at the Fermi level. Our calculations show that the phonon frequencies for β-cristobalite BiO_2 at Γ are positive, so it is a metastable structure. Further calculations reveal that it becomes unstable under uniform compression exceeding 2 GPa, which represents a stability barrier of approximately 0.025 eV per atom. On this basis, the possibility of synthesis appears promising. However, Bi_2O_4 is also likely to take the cervantite structure (after Sb_2O_4, which has similar stoichiometry [21]) which is 0.5 eV per atom lower in energy as compared to β cristobalite and 60% smaller in volume. Therefore we conclude that β-cristobalite BiO_2 would be metastable if synthesized, although preventing it from directly forming the cervantite structure would be challenging. Nonetheless, we have provided an existence proof of a Dirac semimetal in β-cristobalite BiO_2 due to real atomic potentials at the DFT level.

We thank Jay Kikkawa and Fan Zhang for helpful comments on the manuscript. This work was supported in part by the MRSEC program of the National Science Foundation under Grant No. DMR11-20901 (S. M. Y.), by the Department of Energy under Grant No. FG02-ER45118 (E. J. M. and S. Z.), and by the National Science Foundation under Grants No. DMR11-24696 (A. M. R.) and No. DMR09-06175 (C. L. K. and J. C. Y. T.). S. M. Y. acknowledges computational support from the High Performance Computing Modernization Office.

*Present address: Department of Physics, University of Illinois at Urbana-Champaign, Urbana, IL 61801-3080, USA.

[1] A. H. Castro Neto, F. Guinea, N. M. R. Peres, K. S. Novoselov, and A. K. Geim, Rev. Mod. Phys. **81**, 109 (2009).
[2] C. L. Kane and E. J. Mele, Phys. Rev. Lett. **95**, 226801 (2005).
[3] S. Murakami, New J. Phys. **9**, 356 (2007).
[4] S. M. Young, S. Chowdhury, E. J. Walter, E. J. Mele, C. L. Kane, and A. M. Rappe, Phys. Rev. B **84**, 085106 (2011).
[5] J. C. Smith, S. Banerjee, V. Pardo, and W. E. Pickett, Phys. Rev. Lett. **106**, 056401 (2011).
[6] X. Wan, A. M. Turner, A. Vishwanath, and S. Y. Savrasov, Phys. Rev. B **83**, 205101 (2011).
[7] K. Y. Yang, Y. M. Lu, and Y. Ran, Phys. Rev. B **84**, 075129 (2011).
[8] G. B. Halász and L. Balents, Phys. Rev. B **85**, 035103 (2012).
[9] A. A. Burkov and L. Balents, Phys. Rev. Lett. **107**, 127205 (2011).
[10] J. L. Mañes, arXiv:1109.2581v2.
[11] L. Fu, C. L. Kane, and E. J. Mele, Phys. Rev. Lett. **98**, 106803 (2007).
[12] C. Fang, M. J. Gilbert, X. Dai, and B. A. Bernevig, arXiv:1111.7309v1.
[13] C. J. Bradley and A. P. Cracknell, *The Mathematical Theory of Symmetry in Solids* (Clarendon Press, Oxford, 1972).
[14] M. Hamermesh, *Group Theory and its Applications to Physical Problems* (Addison-Wesley Publishing Company, Inc. New York, 1964).
[15] G. Dresselhaus, Phys. Rev. **100**, 580 (1955).
[16] M. Konig *et al.*, Science **318**, 766 (2007).
[17] P. Giannozzi *et al.*, J. Phys. Condens. Matter **21**, 395502 (2009).
[18] A. M. Rappe, K. M. Rabe, E. Kaxiras, and J. D. Joannopoulos, Phys. Rev. B **41**, 1227 (1990).
[19] N. J. Ramer and A. M. Rappe, Phys. Rev. B **59**, 12471 (1999).
[20] P. Villars and L. Calvert, *Pearson's Handbook of Crystallographic Data for Intermetallic Phases* (ASM International, Materials Park, Ohio, 1991), 2nd ed.
[21] G. Thornton, Acta Crystallogr. Sect. B **33**, 1271 (1977).

Spin texture on the Fermi surface of tensile-strained HgTe

Saad Zaheer,[1] S. M. Young,[2] D. Cellucci,[3] J. C. Y. Teo,[1,*] C. L. Kane,[1] E. J. Mele,[1] and Andrew M. Rappe[2]
[1]*Department of Physics and Astronomy, University of Pennsylvania, Philadelphia, Pennsylvania 19104-6396, USA*
[2]*The Makineni Theoretical Laboratories, Department of Chemistry, University of Pennsylvania, Philadelphia, Pennsylvania 19104-6323, USA*
[3]*Department of Physics and Astronomy, University of Georgia, Athens, Georgia 30602, USA*
(Received 4 June 2012; published 3 January 2013)

We present *ab initio* and $\mathbf{k}\cdot\mathbf{p}$ calculations of the spin texture on the Fermi surface of tensile-strained HgTe, which is obtained by stretching the zinc-blende lattice along the (111) axis. Tensile-strained HgTe is a semimetal with pointlike accidental degeneracies between a mirror symmetry protected twofold degenerate band and two nondegenerate bands near the Fermi level. The Fermi surface consists of two ellipsoids which contact at the point where the Fermi level crosses the twofold degenerate band along the (111) axis. However, the spin texture of occupied states indicates that neither ellipsoid carries a compensating Chern number. Consequently, the spin texture is locked in the plane perpendicular to the (111) axis, exhibits a nonzero winding number in that plane, and changes winding number from one end of the Fermi ellipsoids to the other. The change in the winding of the spin texture suggests the existence of singular points. An ordered alloy of HgTe with ZnTe has the same effect as stretching the zinc-blende lattice in the (111) direction. We present *ab initio* calculations of ordered $Hg_xZn_{1-x}Te$ that confirm the existence of a spin texture locked in a 2D plane on the Fermi surface with different winding numbers on either end.

DOI: 10.1103/PhysRevB.87.045202 PACS number(s): 71.18.+y, 71.20.Nr, 71.22.+i

Mercury telluride (HgTe) is a zero-band-gap zinc-blende semiconductor with an inverted ordering of states at Γ,[1] where the band gap and inversion can be controlled by alloying with CdTe. HgTe and CdTe are both zinc-blende materials, with the crucial difference that the stronger spin-orbit coupling of Hg causes the states at Γ to invert relative to each other (Fig. 1). Therefore, HgTe/CdTe quantum wells exhibit the quantum spin Hall effect.[2] The electronic properties of alloys of HgTe have been studied extensively for many decades. Recently there has been a surge of interest in so-called topological (Weyl) semimetals: three-dimensional materials which exhibit pointlike degeneracies (Weyl points)[3] between bulk conduction and valence bands and exhibit topologically protected surface modes.[4–6] These topological Weyl points are low-symmetry descendants of a so-called Dirac point, which is described by a massless four-band Dirac-like Hamiltonian.[7] The unique feature of a Dirac semimetal is a Fermi surface that surrounds discrete Dirac points, around which all bands disperse linearly in all directions. It turns out that HgTe is *almost* a Dirac semimetal: At Γ two conduction states are degenerate with two valence states; all four bands disperse linearly along the (110) and (100) axes; however, mirror and time-reversal symmetry guarantee that, along the (111) axis, two of the four bands must disperse *quadratically* [Refs. 7 and 8 and Fig. 2(a)].

Figure 2(a) shows another interesting feature of the bands at Γ. In addition to the symmetry-guaranteed fourfold degeneracy, there are *additional* pointlike accidental degeneracies along the (111) axis between two conduction states and one valence state. The rest of the band structure is completely gapped, so the Fermi surface is confined to a small region around Γ [Fig. 2(b)]. It is natural to ask what perturbations could turn HgTe into a Dirac semimetal. Since the quadratic dispersion of bands near Γ is enforced by mirror and time-reversal symmetry, any perturbation must break either one of these symmetries. A time-reversal-symmetry-breaking Zeeman field breaks at least one rotation symmetry of the tetrahedral group, splitting the fourfold degeneracy at Γ so the system either gaps or develops additional Fermi surface. Breaking mirror symmetry maintains the fourfold degeneracy at Γ, but the Dirac point develops a nonzero Chern number due to the threefold rotation symmetry of zinc blende. This inevitably leads to additional Fermi surface as well. Hence, zinc-blende materials cannot be Dirac semimetals.[7] A third option is to break, for instance, a fourfold rotation symmetry by straining the lattice. Such a procedure will split the fourfold degeneracy at Γ and will either gap the band structure completely or else shift the accidental degeneracy away from Γ along the (111) axis.

Reference 9 predicted that compressive strain along the (111) axis will gap HgTe into a topological insulator, since the states at Γ are already inverted [Fig. 3(a)]. The inverted ordering of bands at Γ is a direct consequence of spin-orbit coupling. To understand how it comes about, we compare the ordering of states in HgTe with and without spin (Fig. 1). At the Fermi level in spinless HgTe, the valence states span a p-type representation Γ_4 of space group 216. Slightly above Γ_4 in energy, there exists an s-type band which belongs to the symmetric representation Γ_1. When spin-orbit coupling is introduced, the representation Γ_4 splits into a $p_{3/2}$-type representation Γ_8 and a $p_{1/2}$-type representation Γ_7, whereas Γ_1 turns into an $s_{1/2}$-type representation Γ_6. Since Hg is a heavy atom, its contribution to the spin-orbit coupling is strong enough to push the $s_{1/2}$-type band Γ_6 below Γ_8, resulting in an inverted band structure. This is in contrast with a normal ordered zinc-blende semiconductor (e.g., CdTe), where Γ_6 appears above Γ_8 in energy. Reference 2 demonstrated that if Γ_8 is split and the inversion of Γ_6 relative to the split band Γ_8 is controlled by a "mass" parameter, the insulating phases that ensue have a nontrivial $\mathbb{Z}_2$ index $+1$ in the inverted regime, versus a trivial index 0 in the normal regime. The splitting of Γ_8 was achieved in a HgTe/CdTe quantum-well structure, while the tuning of Γ_6 above or below the split

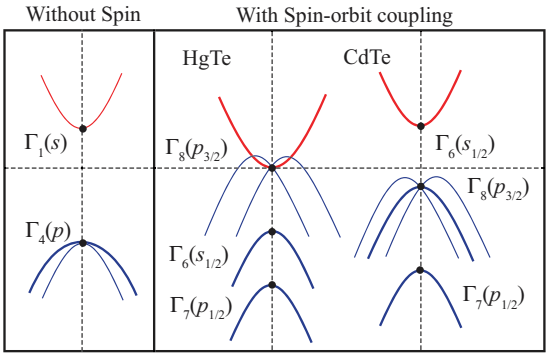

FIG. 1. (Color online) Schematic illustration of band inversion in HgTe due to strong spin-orbit coupling. Twofold degenerate bands are drawn as thick lines, whereas nondegenerate bands are drawn as thin lines. (Left) Without spin, HgTe/CdTe have an s-type conduction band and a p-type valence band. (Middle) The spin-orbit coupling in HgTe is strong enough to push the $s_{1/2}$-type representation Γ_6 below the $p_{3/2}$-type representation Γ_8. (Right) Normal ordering of states in CdTe, which has a weaker spin-orbit coupling as compared with HgTe. The $s_{1/2}$-type representation Γ_6 appears above the $p_{3/2}$-type representation Γ_8, as expected from the spinless case.

representation Γ_8 was controlled by the well thickness, leading to the first experimental observation of the quantum spin Hall effect.[10]

In this paper, we show that whereas compressive strain along the (111) axis gaps the system entirely [Fig. 3(a)], tensile strain along the same axis shifts the accidental degeneracies further along the (111) axis after splitting Γ_8 [Fig. 3(b)]. Tensile-strained HgTe remains a semimetal where the dispersion of bands around the accidental degeneracies is linear in all directions (Fig. 4). However, there is a caveat. Each accidental degeneracy involves *three* states so it is neither a Dirac point nor a Weyl point. As discussed earlier, this is due to the presence of mirror symmetry about a plane that contains the (111) axis. If we could break the mirror symmetry, the twofold degenerate band in Fig. 2(a) would split and the system will develop two Weyl points (Fig. 5).

A Weyl point carries a nonzero Chern number (charge) ± 1 and cannot be annihilated unless brought in contact with another Weyl point of opposite charge. In other words, the spin texture of valence states around a Weyl point has nonzero divergence; if interpreted as a magnetic field, the spin texture would correspond to a magnetic monopole with charge ± 1. However, mirror symmetry constrains all points on its mirror plane to have zero Chern number. Hence, Weyl points cannot exist on mirror planes, and so the integral of the normal component of spins on a closed surface that encloses points on a mirror plane must be zero.

This has important implications for the Fermi surface of tensile-strained HgTe (Fig. 4). The two Fermi ellipsoids contact at a point due to mirror symmetry. They can be separated only if mirror symmetry is broken. Consequently, their corresponding spin textures will develop a nonzero divergence. We ask the following: What is the nature of the spin texture on the ellipsoidal Fermi surface *before* mirror symmetry is broken? It turns out that spin texture on both ellipsoids is locked in a plane perpendicular to the (111) axis and exhibits a nonzero winding number about that axis. Furthermore, the winding number changes as one sweeps across the Fermi ellipsoids from one end to the other and inevitably exhibits spin singularities on the Fermi surface where the winding number must change (Fig. 6).

We alloy HgTe with ZnTe by replacing half the Hg atoms with Zn atoms. The size mismatch between Hg and Zn causes the lattice to relax so that the Zn and Hg atoms move off center towards the Te atoms. This has the same effect as tensile strain along the (111) axis in zinc blende (Fig. 7).

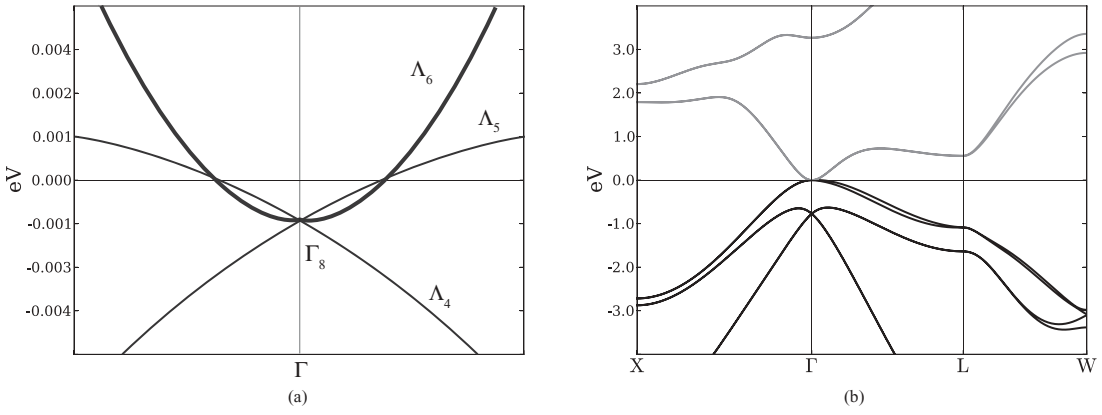

FIG. 2. Band structure of HgTe. (a) Energy bands near the Fermi level as a function of momentum along the (111) axis. At Γ the four degenerate states span the irreducible representation Γ_8 of the group T_d. $\Lambda_{4,5,6}$ are irreducible representations of the group C_{3v}. The twofold degenerate (solid) band labeled Λ_6 disperses quadratically to lowest order, whereas the nondegenerate bands Λ_4 and Λ_5 disperse linearly. There are threefold accidental degeneracies at $\mathbf{k} = \pm 0.004(1,1,1)$ because the bands Λ_4 and Λ_5 have negative mass, whereas Λ_6 has positive mass. (b) Band structure of HgTe as a function of crystal momentum across the entire Brillouin zone. The valence and conduction bands are gapped everywhere except near Γ.

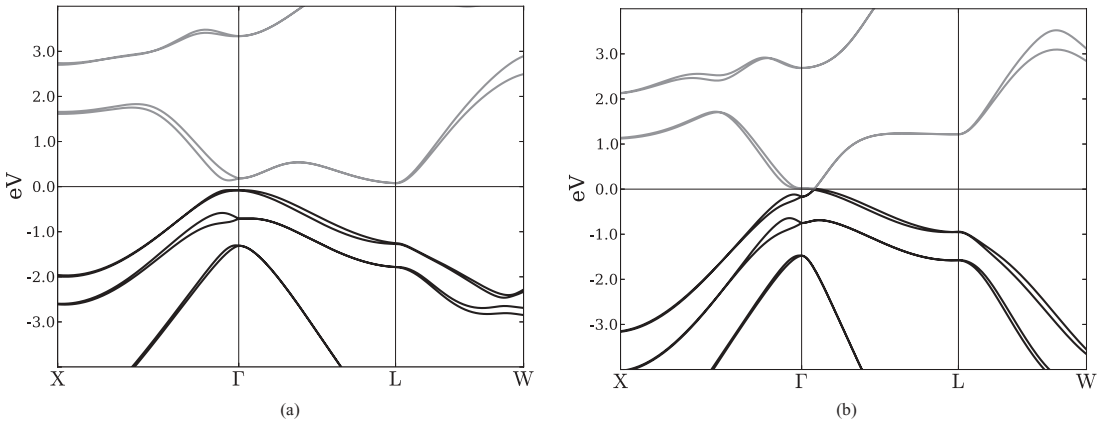

FIG. 3. (a) Band structure of HgTe under compressive strain along the (111) axis. The fourfold degenerate representation Γ_8 is split, and the material becomes a topological insulator (Ref. 9). (b) Band structure of HgTe under tensile strain along the (111) axis. Although Γ_8 splits under tensile strain as well, the accidental degeneracy along the (111) axis shifts away from Γ and the material remains semimetallic.

Indeed, *ab initio* calculations indicate that the spin texture on the Fermi surface of $Hg_xZn_{1-x}Te$ ($x = 0.5$) is locked in a two-dimensional plane and exhibits spin singular points identical to tensile-strained HgTe (Fig. 8). However, it is likely that density functional theory (DFT) overestimates[11] the amount of band inversion for $x = 0.5$ given that $Hg_xCd_{1-x}Te$ is a band insulator for $x < 0.8$.[12] Nonetheless, for small-enough concentrations of Zn, this symmetry-protected spin texture may indeed by realized physically. It is difficult to span the full range of intermediate compositions within DFT to make a prediction of the composition where the inversion occurs.

In Sec. I, we describe the Fermi surface of tensile-strained HgTe. In Sec. II, we derive a simple $\mathbf{k} \cdot \mathbf{p}$ model to understand band dispersion in tensile-strained HgTe. In Sec. III, we derive the spin texture at the $\mathbf{k} \cdot \mathbf{p}$ level and provide *ab initio* calculations of $Hg_{0.5}Zn_{0.5}Te$ in support of the predictions of the $\mathbf{k} \cdot \mathbf{p}$ theory. Finally, we conclude with some brief remarks.

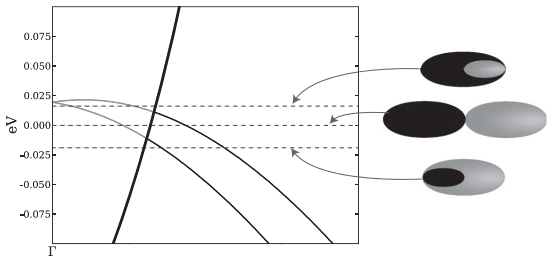

FIG. 4. Band dispersion in tensile-strained HgTe at the Fermi level as a function of momentum along the (111) axis. The twofold degenerate band (drawn as a thick line) is accidentally degenerate with both the nondegenerate bands (drawn as thin lines) within a very small energy range. Band dispersion around the accidental degeneracies is linear to leading order in the (111) direction. (Right) Schematic illustration of the Fermi surface. The Fermi surface for various choices of Fermi energy (drawn in dashed lines) near the accidental degeneracies consists of two ellipsoids which contact at a point. This indicates that the bands disperse linearly in transverse directions as well around the accidental degeneracies.

I. FERMI SURFACE

The band structure of HgTe has been of considerable interest in recent years because HgTe alloyed with CdTe exhibits a tunable direct band gap from 0 to 1.5 eV at Γ. We focus our attention to the four-dimensional irreducible representation Γ_8 at the Fermi level. The point group elements of the little group at Γ belong to T_d (the tetrahedral group with mirror planes). Since the zinc-blende lattice lacks inversion symmetry, the matrix elements $\langle|\psi_i|\hat{\mathbf{p}}|\psi_j\rangle$, where $\{|\psi_i\rangle\}$ span Γ_8, are nonzero. Therefore, the four bands degenerate at Γ can, in principle, disperse linearly in all directions around Γ (Ref. 7). However, along the (111) axis, Γ_8 splits into a two-dimensional representation Λ_6 and two one-dimensional representations Λ_4 and Λ_5 of the little group along that axis. Since Γ is invariant under time-reversal symmetry, Λ_6 is constrained to be flat, whereas Λ_4 and Λ_5 must disperse with nonzero slope. Along other directions such as (110) and (100), Γ_8 splits into either four singlets or two doublets, and none

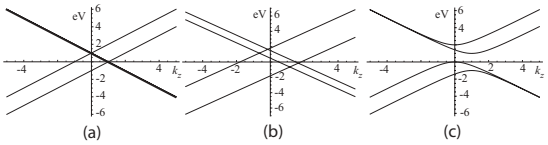

FIG. 5. (a) Energy bands plotted as a function of momentum in the k_z direction in the $\mathbf{k} \cdot \mathbf{p}$ theory. There is a twofold degenerate band (thick line) intersecting two nondegenerate bands (thin lines) analogous to Fig. 4. (b) Mirror- and time-reversal-symmetry-breaking perturbation proportional to J_z splits the twofold degenerate band into two nondegenerate bands, giving rise to four Weyl points. (c) Rotation- and mirror-symmetry-breaking perturbation proportional to $\tau_z\sigma_x$ gaps the system entirely.

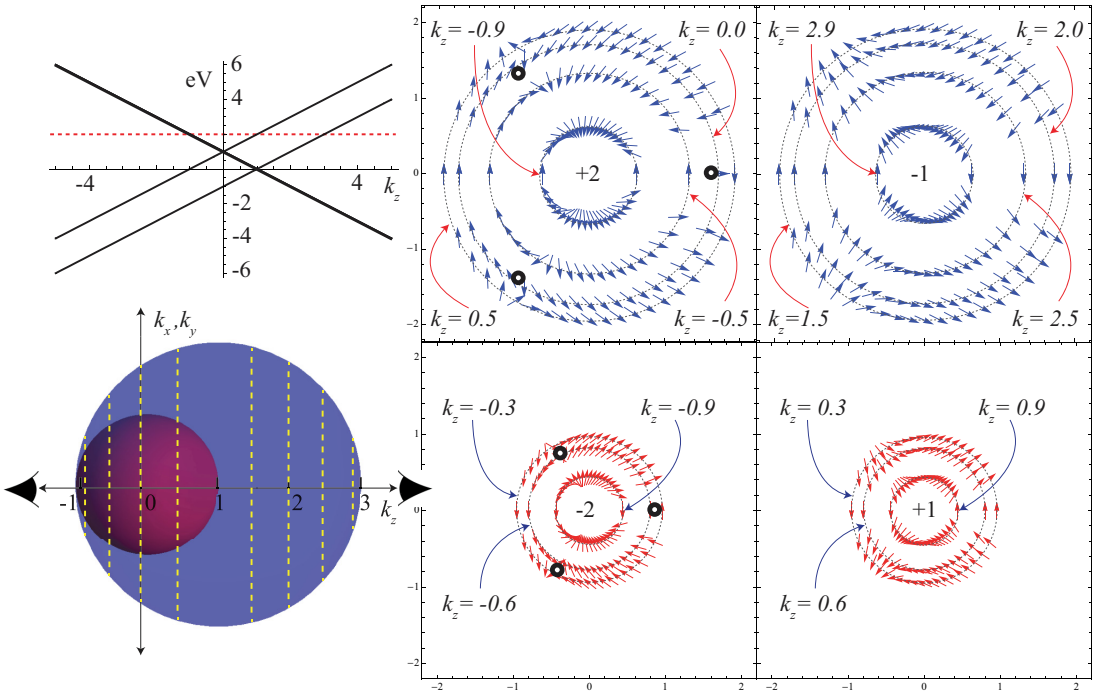

FIG. 6. (Color online) Spin texture on the Fermi surface of tensile-strained HgTe as predicted by the $\mathbf{k}\cdot\mathbf{p}$ theory of Eq. (1). (Top left) Band dispersion in the $\mathbf{k}\cdot\mathbf{p}$ theory as a function of momentum along the (111) axis. The Fermi level $\mathcal{E}_F$ (dashed line) is set to be 2 eV in the units of Eq. (1). (Bottom left) The Fermi surface for $\mathcal{E}_F = 2$ eV at the $\mathbf{k}\cdot\mathbf{p}$ level consists of two spherical shells which touch at the point $k_z = -1$. (Top right) The spin texture of valence states on the blue Fermi spherical shell as a function of momentum in the k_x,k_y plane. Each circle corresponds to a constant k_z (indicated by dashed yellow lines cutting through the Fermi surface on the left). (Bottom right) The spin texture of valence states on the red Fermi spherical shell as a function of momentum in the k_x,k_y plane. The spins are locked in the k_x,k_y plane for both Fermi shells. The winding number of spins on each Fermi shell changes as one moves from one end along k_z to the other. There are three points indicated in yellow where the spin texture vanishes. The spin winding number flips from ± 2 to ∓ 1 at these spin singular points.

of the bands are constrained to be flat to linear order in $\mathbf{k}$ (Refs. 7 and 8). This is why the four-band model describing states $\{|\Gamma_8,3/2\rangle,|\Gamma_8,-3/2\rangle,|\Gamma_6,1/2\rangle,|\Gamma_6,-1/2\rangle\}$ in Ref. 2 was written as a Dirac Hamiltonian in *two* dimensions.

It turns out that the bands belonging to Λ_4 and Λ_5 have negative mass [Fig. 2(b)]. Therefore, to $\mathcal{O}(\mathbf{k}^2)$ and above, the bands labeled Λ_4 and Λ_5 must bend back below the Fermi level and cross Λ_6 somewhere along the (111) axis. High-resolution *ab initio* calculations confirm that these degeneracies indeed occur very close to Γ at $\pm 0.004(1,1,1)$ [Fig. 2(a)]. Since this occurs so close to Γ, the Fermi surface of HgTe is only effectively pointlike.

Under tensile strain along the (111) axis, the representation Γ_8 splits, because the tetrahedral group T_d reduces to the trigonal group $C_{3v} = \{1,x,x^2,y,xy,x^2y\}$. Here x corresponds to threefold rotation symmetry about the (111) axis while $\{y,xy,x^2y\}$ represent the three mirror planes that contain the (111) axis and are rotated by $2\pi/3$ with respect to each other. Since tensile strain preserves the little group along the line from Γ to L, the representation Λ_6 does not split. Therefore, the accidental degeneracies between Λ_4/Λ_5 and Λ_6 only shift further away from Γ, and HgTe remains a semimetal.

Figure 4 shows the band structure along the (111) direction for 8% tensile strain in HgTe. The set of momenta corresponding to a fixed energy form two ellipsoidal surfaces that contact at a point. This implies that the bands Λ_4, Λ_5, and Λ_6 disperse linearly in all directions around the accidental degeneracies. Therefore, under tensile strain the Fermi surface of HgTe grows from a point to a set of four ellipsoids in two sets of Kramers paired momenta in the Brillouin zone. The two ellipsoids on one side of Γ are connected to each other at the point $\mathbf{k}$ along the (111) axis where the Fermi level crosses the band Λ_6.

We note that 8% tensile strain corresponds to 4% strain in plane, which is relatively large. This effect ensues as soon as a perturbation breaking the fourfold symmetry of zinc blende turns on; there is no critical value of strain below which the unusual spin texture of the Fermi surface would disappear. While 8% tensile strain, which corresponds to 4% strain in plane, is quite high, the ellipsoidal Fermi surfaces ought to be observable at reduced strains; at 2% tensile strain the energy difference between the threefold degeneracies is still 18 meV, down from 25 meV. Even so, very high strains may be achievable through epitaxial growth of HgTe on an appropriate substrate.[13]

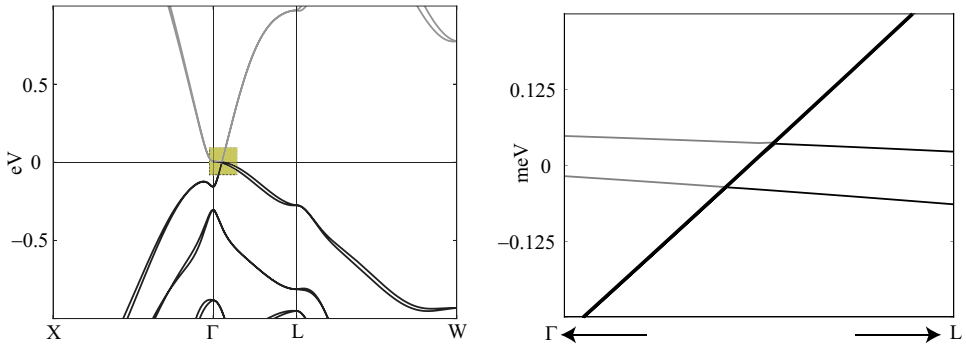

(a) (b)

FIG. 7. (Color online) (a) Band structure of $Hg_{0.5}Zn_{0.5}Te$ is the same as tensile-strained HgTe [Fig. 3(b)], except the shape and size of the Fermi surface and the Fermi velocities in the two materials. (b) Band dispersion at the Fermi level near the accidental degeneracies along the (111) axis. There is a twofold degenerate band (thick line) intersecting two nondegenerate bands (thin lines), essentially identical to tensile-strained HgTe (Fig. 4).

Alternatively, strain can be introduced chemically. Alloying HgTe with ZnTe introduces a size mismatch between Hg and Zn, causing both Zn and Hg atoms to move off center toward a Te atom; if all the Zn atoms move in the same direction, the symmetry breaking is the same as that created by tensile strain. A similar effect has also been reported in $Cd_xZn_{1-x}Te$ (Ref. 14), which shows rhombohedral distortions and Zn off centering for a wide range of Zn concentration. Figure 7 shows the band structure of ordered $Hg_{0.5}Zn_{0.5}Te$, which is qualitatively the same as that of strained HgTe. The difference lies in the shape and size of the Fermi surface and the Fermi velocities in the two materials. As a caveat, it is important to note that DFT overestimates the magnitude of band inversion;[11] $Hg_xCd_{1-x}Te$ for $x < 0.8$ is a band insulator,[12] and $Hg_{0.5}Zn_{0.5}Te$ is likely to be gapped in actuality. However, calculations for $Hg_{0.75}Zn_{0.25}Te$ suggest that significant symmetry-breaking distortion persists for lower Zn concentration, consistent with the observations of similar behavior in $Cd_xZn_{1-x}Te$ (Ref. 14). Therefore, if some ordered compound $Hg_xZn_{1-x}Te$ exists with x such that distortion due to Zn substitution sufficiently splits the degeneracy at the Fermi level while still allowing band inversion, then it would possess an experimentally observable ellipsoidal Fermi surface. We assert that a time-reversal- and mirror-symmetry-breaking Zeeman field would split the degenerate band Λ_6 and turn $Hg_xZn_{1-x}Te$ into a Weyl semimetal. This is confirmed by our $\mathbf{k}\cdot\mathbf{p}$ theory in Sec. II. A Weyl semimetal obtained by a Zeeman perturbation to $Hg_xZn_{1-x}Te$ will have interesting phenomenological consequences such as Fermi-arc surface states[5] and pressure-induced anomalous Hall effect.[6]

While some experimental studies have been performed on $Hg_{1-x}Zn_xTe$, it is difficult to draw any direct conclusions without more detailed structural characterization of the samples.[15,16] We performed a phonon analysis of

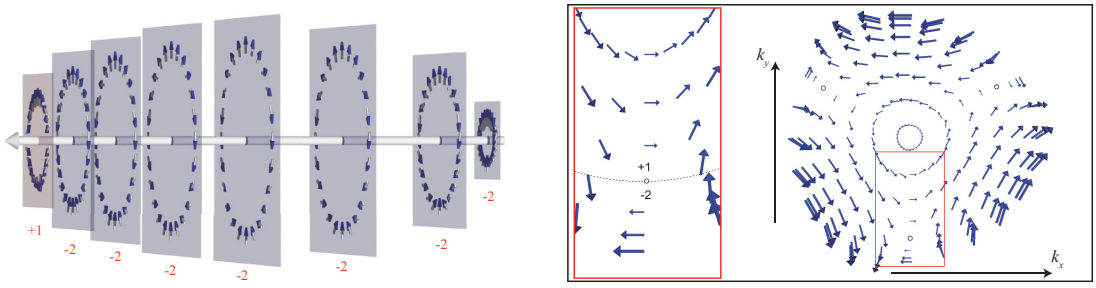

(a) (b)

FIG. 8. (Color online) Spin texture on the Fermi surface of $Hg_{0.5}Zn_{0.5}Te$ at the *ab initio* DFT level. (a) Spins on a Fermi surface ellipsoid of $Hg_{0.5}Zn_{0.5}Te$ are locked in the plane perpendicular to the (111) axis. The spin winding number around the (111) axis changes from $+1$ to -2 from the left end of the ellipsoid to the right end. (b) Spin texture in the two-dimensional plane transverse to the (111) direction. Each concentric loop of spins corresponds to a fixed value of momentum along the (111) axis. The spin winding number around the (111) axis changes from the inner circles to the outer circles on the Fermi ellipsoid. Since spins are locked on the transverse plane, their winding number changes as they vanish at three rotation-symmetry-related singular points (drawn as white circles outlined in black). (Left) A higher-resolution image showing the change in the spin winding number from $+1$ to -2 as we move from the inner radii to the outer radii on the right. For visual clarity, the magnitude of all vectors is normalized in (a), while in (b) the size of each vector equals the square root of its magnitude.

tensile-strained HgTe and $Hg_{0.5}Zn_{0.5}Te$ and found no structural instability.

II. K · P THEORY

We model the low-energy physics of the states that span the representations Λ_4, Λ_5, and Λ_6 along the (111) axis in terms of a four-band $\mathbf{k}\cdot\mathbf{p}$ theory around the accidental degeneracies. The states which belong to Λ_6 are $|p,\pm\frac{3}{2}\rangle$, whereas the ones belonging to Λ_4 and Λ_5 are $|p,\pm\frac{1}{2}\rangle$. The symmetry group is $C_{3v} = \{1,x,x^2,y,xy,x^2y\}$ with the group multiplication rules $x^3 = y^2 = 1, yx = x^2y$ in addition to time-reversal symmetry. Here x represents a threefold rotation symmetry while y represents a mirror symmetry. The accidental degeneracies occur at points $\mathbf{k}_0 \neq 0$ along the line from Γ to L, which are not time-reversal symmetric. So the time-reversal operator Θ maps the $\mathbf{k}\cdot\mathbf{p}$ Hamiltonian around $\mathbf{k}_0$ to its time-reversed partner around $-\mathbf{k}_0$.

We choose an angular momentum basis for the $\mathbf{k}\cdot\mathbf{p}$ theory. Since we are dealing with four half-integer spin states, we require a double valued representation of C_{3v}, such that x and y take the form of matrices $\hat{R}$ and $\hat{M}$ belonging to SU(4) that satisfy $\hat{R}^3 = \hat{M}^2 = -1$. These operators satisfy the group multiplication rules and are consistent with the interpretation of the operators $\hat{M}, \hat{R}\hat{M}, \hat{R}^2\hat{M}$ as mirror symmetries (all of which square to -1) for particles with half-integer spin.

Orienting the k_z direction along the (111) axis, the threefold rotation operator is diagonal and can be written as $\hat{R} = \exp(i\hat{J}_z 2\pi/3)$, where $\hat{J}_z$ is the angular momentum operator. The mirror operator in this basis takes the form $\hat{M} = i\tau_y \otimes \sigma_x$. $\vec{\tau}$ and $\vec{\sigma}$ denote Pauli matrices. Tensor products of Pauli matrices can be used as basis vectors for 4×4 Hermitian matrices. Neither $\vec{\tau}$ nor $\vec{\sigma}$ *individually* corresponds to a real or pseudospin degree of freedom. In what follows, we write $\tau_i \otimes \sigma_j$ as $\tau_i\sigma_j$, where the tensor product is implied. In the absence of inversion symmetry $\mathcal{P}$, the local antiunitary operator $\mathcal{P}\Theta$ is not a symmetry. $\mathcal{P}\Theta$ is a local operator because both $\mathcal{P}$ and Θ send $\mathbf{k}$ to $-\mathbf{k}$. In the angular momentum basis, it can be written as $\mathcal{P}\Theta = i\tau_x\sigma_y K$, where K is the complex conjugation operator.

A Hamiltonian linear in $\mathbf{k}$ which respects these symmetries is

$$\hat{H}(\mathbf{k}) = k_x\tau_x + k_y\tau_y + k_z\tau_z\sigma_z + \kappa, \tag{1}$$

where

$$\kappa = \begin{pmatrix} 0 & 0 & 0 & -i \\ 0 & 1 & 0 & 0 \\ 0 & 0 & 1 & 0 \\ i & 0 & 0 & 0 \end{pmatrix}$$

is chosen to break the local antiunitary symmetry $\mathcal{P}\Theta$. With this choice of κ, time reversal symmetry is preserved while inversion is broken if we require that $\Theta\hat{H}(\mathbf{k})\Theta^{-1} = \tau_x k_x + \tau_y k_y + \tau_z\sigma_z k_z + \kappa^T$ is the effective $\mathbf{k}\cdot\mathbf{p}$ Hamiltonian around the time-reversed location of the accidental degeneracies. Such a constraint is allowed because the $\mathbf{k}\cdot\mathbf{p}$ theory is localized around a Brillouin zone momentum $\mathbf{k}_0 \neq 0$ along the (111) axis.

Figure 5 shows the energy spectrum of the Hamiltonian in Eq. (1) along the k_z axis. The degenerate band Λ_6 splits to give four Weyl points under a mirror- and time-reversal-symmetry-breaking Zeeman term proportional to σ_z or J_z where J_z is the angular momentum operator of $p_{3/2}$ states. Figure 5(b) shows the splitting of Λ_6 to give four Weyl points due to a perturbation proportional to J_z. A rotation- and mirror-symmetry-breaking perturbation such as $\tau_z\sigma_x$ gaps the system entirely [Fig. 5(c)].

It is possible to split Λ_6 into two parallel bands as in Fig. 5(b) by a mirror-preserving term $\tau_y\sigma_x$, which breaks time-reversal and rotation symmetry. This, however, does not lead to Weyl points; even though the degeneracies involve two states, the bands develop a quadratic dispersion in one direction. Mirror symmetry about a plane constrains all points $\mathbf{k}$ on the plane to have zero Chern number. This is explained as follows: The Chern number of a certain point $\mathbf{k}$ in the Brillouin zone is given by an integer $n = 1/(2\pi i)\oint_S \mathrm{Tr}\vec{\mathcal{F}}\cdot\hat{n}$, where $\vec{\mathcal{F}}_{ij} = \nabla_{\mathbf{k}} \times \langle\psi_i|\nabla_{\mathbf{k}}|\psi_j\rangle$ is the Berry curvature, $\hat{n}$ is a unit vector normal to the surface S that contains $\mathbf{k}$, and the trace includes only valence states $|\psi_i\rangle, i = 1,\ldots,N$. A mirror symmetry about a plane that contains $\mathbf{k}$ reverses the orientation of the surface S while the integrand is the same for opposing points on S. Hence, the Chern number of all points on a mirror plane must be zero. Therefore, as long as mirror symmetry is present, tensile-strained HgTe cannot host Weyl points along the (111) axis.

III. SPIN TEXTURE

Since the dispersion of bands around the accidental degeneracies in Figs. 4 and 5(a) is linear in $\mathbf{k}$, it is natural to ask if the accidental degeneracies have an associated Chern number. However, since the (111) axis belongs to a mirror plane, the Chern number of all points on that axis should be zero. In other words, the surface integral of the normal component of the spin texture over a closed surface enclosing the accidental degeneracies will be zero. The ellipsoidal Fermi surface in $Hg_{0.5}Zn_{0.5}Te$ also encloses the accidental degeneracies, as shown in Fig. 4. At the $\mathbf{k}\cdot\mathbf{p}$ level, this corresponds to two spheres in $\mathbf{k}$ space parametrized as $S_1 : \mathcal{E}^2 = k_x^2 + k_y^2 + (1-k_z)^2$ and $S_2 : (\mathcal{E}-1)^2 = k_x^2 + k_y^2 + k_z^2$, where $\mathcal{E}$ is the Fermi energy. The average spin field is given by $\langle\psi_i|\hat{\mathbf{S}}|\psi_i\rangle$, where $|\psi_i\rangle$ is a valence state on one of the Fermi ellipsoids parametrized by $\mathcal{E}$ and $\hat{\mathbf{S}}$ is the spin operator for the $p_{3/2}$ states. In the $\mathbf{k}\cdot\mathbf{p}$ theory, this evaluates to

$$\begin{aligned}\langle\hat{\mathbf{S}}\rangle_i = {}& \alpha_i(\mathcal{E},k_z)[\sin(\theta)\hat{\mathbf{i}} + \cos(\theta)\hat{\mathbf{j}}] \\ & + \beta_i(\mathcal{E},k_z)[\sin(2\theta)\hat{\mathbf{i}} - \cos(2\theta)\hat{\mathbf{j}}],\end{aligned} \tag{2}$$

where the subscript $i = 1,2$ identifies one of the Fermi ellipsoids S_i and θ is the azimuthal angle in the k_xk_y plane that parametrizes the ellipsoids. The coefficients α_i, β_i are

$$\alpha_1(\mathcal{E},k_z) = -\sqrt{\frac{4(\mathcal{E}+1-k_z)}{3(\mathcal{E}-1+k_z)}}, \quad \beta_1(\mathcal{E},k_z) = -\frac{\alpha_1(\mathcal{E},k_z)^2}{2},$$

$$\alpha_2(\mathcal{E},k_z) = \sqrt{\frac{4(\mathcal{E}-1-k_z)}{3(\mathcal{E}-1+k_z)}}, \quad \beta_2(\mathcal{E},k_z) = \frac{\alpha_2(\mathcal{E},k_z)^2}{2}.$$

The three mirror planes of the group C_{3v}, all of which contain the k_z axis, lock the spin expectation values in the k_xk_y plane. Figure 6 shows how the spin texture evolves as a function of k_z around the Fermi ellipsoids. For fixed $\mathcal{E}$, k_z ranges between $1-|\mathcal{E}|$ and $1+|\mathcal{E}|$ on S_1 and between $-|1-\mathcal{E}|$ and $|1-\mathcal{E}|$ on S_2. When k_z is close to $1-\mathcal{E}$ on either ellipsoid, the term with the coefficient β_i dominates and the spin winding number is -2, whereas when k_z is close to $\mathcal{E}+1$ on S_1 or $\mathcal{E}-1$ on S_2 the term with the coefficient α_i dominates, and the spin winding number is $+1$. Therefore, the spin winding number must change abruptly from one end of the Fermi ellipsoids to the other, since the spins cannot develop a component in the k_z direction due to mirror symmetry. Hence, there must exist singular points on the Fermi ellipsoids where the spin expectation values vanish. Figure 6 shows the points on the Fermi ellipsoids where the spin expectation value goes to zero. There are three such singular points which are related to each other by threefold symmetry, and their exact location can be calculated in the $\mathbf{k}\cdot\mathbf{p}$ theory. Note that although the α_i diverge in the limit $k_z\to 1-\mathcal{E}$, the points where $k_z=1-\mathcal{E}$ correspond to the degenerate band Λ_6, and since α_1,β_1 and α_2,β_2 have opposite signs, the total spin $\langle\hat{\mathbf{S}}\rangle_1+\langle\hat{\mathbf{S}}\rangle_2=0$ for states in Λ_6.

We have carried out *ab initio* calculations to confirm that tensile-strained HgTe and $Hg_{0.5}Zn_{0.5}Te$ exhibit identical spin texture at the Fermi surface. Figure 8 illustrates the spin texture on the Fermi surface of $Hg_{0.5}Zn_{0.5}Te$. The spins are locked in a two-dimensional plane perpendicular to the (111) axis, and their winding number changes from one end of the Fermi ellipsoid to the other. Furthermore, the abrupt change in the winding number is accommodated by the vanishing of the spin expectation value at three rotation-symmetry-related points on the Fermi ellipsoid. Density functional theory calculations were performed in the QUANTUM ESPRESSO suite using the Perdew-Burke-Ernzerhof-type generalized gradient approximation (GGA).[17] All calculations used an $8\times8\times8$ Monkhorst-Pack **k**-point mesh with a plane-wave cutoff of 50 Ry. The pseudopotentials representing the atoms in these simulations were generated by the OPIUM package; the pseudopotentials were norm-conserving and optimized and included the full relativistic correction.[18,19]

We have shown that HgTe tensile strained in the (111) axis is semimetallic and exhibits a Fermi surface consisting of two ellipsoids that contact at a point. Due to mirror and threefold symmetry of the zinc-blende lattice, the spin texture on the Fermi ellipsoids is locked in a two-dimensional plane and vanishes at special singular points. We have derived a $\mathbf{k}\cdot\mathbf{p}$ theory to understand this phenomenon at a qualitative level. We propose that this symmetry-protected spin texture can be observed in $Hg_{1-x}Zn_xTe$ for values of x small enough to allow band inversion while sufficiently breaking symmetry.

Note added. We recently became aware that the authors of Ref. 20 studied the effects of biaxial strain (referred to as "strain" in that paper) along the (111) axis in HgTe. They found that the fourfold degeneracy at Γ was lifted and no accidental degeneracies resulted for either positive or negative strain. Therefore, biaxial strain (compressive or tensile) is similar to compressive uniaxial strain in terms of its effect on band structure. In contrast, we find that uniaxial tensile strain not only maintains the accidental degeneracies already present in HgTe but shifts them further away from Γ.

ACKNOWLEDGMENTS

We thank David Vanderbilt and Alexey A. Soluyanov for helpful discussions. This work was supported in part by the MRSEC program of the National Science Foundation under Grant No. DMR11-20901 (S.M.Y.), by the Department of Energy under Grant No. FG02-ER45118 (E.J.M. and S.Z.), and by the National Science Foundation under Grants No. DMR11-24696 (A.M.R.) and No. DMR09-06175 (C.L.K. and J.C.Y.T.). D.C. was supported by the REU Program at LRSM, University of Pennsylvania. S.M.Y. acknowledges computational support from the High Performance Computing Modernization Office.

*Present address: Department of Physics, University of Illinois at Urbana-Champaign, Urbana, Illinois 61801-3080, USA.

[1] O. Madelung, U. Rössler, and M. Schulz (eds.), *Mercury Telluride (HgTe) Band Structure, Band Energies at Symmetry Points*, Vols. III/17B-22A-41B (Springer Materials, The Landolt-Börnstein Database).

[2] B. A. Bernevig, T. L. Hughes, and S. C. Zhang, Science **314**, 1757 (2006).

[3] The Weyl Hamiltonian describes two linearly dispersing bands around a degenerate point. In simplest terms, it can be written as $\hat{H}(\mathbf{k})=k_x\sigma_x+k_y\sigma_y+k_z\sigma_z$.

[4] A. A. Burkov and L. Balents, Phys. Rev. Lett. **107**, 127205 (2011).

[5] X. Wan, A. M. Turner, A. Vishwanath, and S. Y. Savrasov, Phys. Rev. B **83**, 205101 (2011).

[6] K.-Y. Yang, Y.-M. Lu, and Y. Ran, Phys. Rev. B **84**, 075129 (2011).

[7] S. M. Young, S. Zaheer, J. C. Y. Teo, C. L. Kane, E. J. Mele, and A. M. Rappe, Phys. Rev. Lett. **108**, 140405 (2012).

[8] G. Dresselhaus, Phys. Rev. **100**, 580 (1955).

[9] L. Fu and C. L. Kane, Phys. Rev. B **76**, 045302 (2007).

[10] M. König *et al.*, Science **318**, 766 (2007).

[11] A. Svane, N. E. Christensen, M. Cardona, A. N. Chantis, M. van Schilfgaarde, and T. Kotani, Phys. Rev. B **84**, 205205 (2011).

[12] M. W. Scott, J. Appl. Phys. **40**, 4077 (1969).

[13] J. P. Faurie, S. Sivananthan, X. Chu, and P. S. Wijewarnasuriya, Appl. Phys. Lett. **48**, 785 (1986).

[14] R. Weil, R. Nkum, E. Muranevich, and L. Benguigui, Phys. Rev. Lett. **62**, 2744 (1989).

[15] A. Sher, D. Eger, A. Zemel, H. Feldstein, and A. Raizman, J. Vac. Sci. Technol. A **4**, 2024 (1986).

[16] M. Berding, S. Krishnamurthy, A. Sher, and A.-B. Chen, J. Vac. Sci. Technol. A **5**, 3014 (1987).

[17] P. Giannozzi *et al.*, J. Phys.: Condens. Matter **21**, 395502 (2009).

[18] A. M. Rappe, K. M. Rabe, E. Kaxiras, and J. D. Joannopoulos, Phys. Rev. B **41**, 1227(R) (1990).

[19] N. J. Ramer and A. M. Rappe, Phys. Rev. B **59**, 12471 (1999).

[20] A. A. Soluyanov and D. Vanderbilt, Phys. Rev. B **83**, 235401 (2011).

Bulk Dirac Points in Distorted Spinels

Julia A. Steinberg,[1,2,*] Steve M. Young,[1] Saad Zaheer,[2] C. L. Kane,[2] E. J. Mele,[2] and Andrew M. Rappe[1]
[1]*The Makineni Theoretical Laboratories, Department of Chemistry, University of Pennsylvania, Philadelphia, Pennsylvania 19104-6323, USA*
[2]*Department of Physics and Astronomy, University of Pennsylvania, Philadelphia, Pennsylvania 19104-6396, USA*
(Received 23 September 2013; published 22 January 2014)

We report on a Dirac-like Fermi surface in three-dimensional bulk materials in a distorted spinel structure on the basis of density functional theory as well as tight-binding theory. The four examples we provide in this Letter are $BiZnSiO_4$, $BiCaSiO_4$, $BiAlInO_4$, and $BiMgSiO_4$. A necessary characteristic of these structures is that they contain a Bi lattice which forms a hierarchy of chainlike substructures, with consequences for both fundamental understanding and materials design.

DOI: 10.1103/PhysRevLett.112.036403 PACS numbers: 71.18.+y, 71.27.+a, 81.05.Zx

Following the discovery of topological insulators [1], there has been considerable interest in studying semimetallic phases that exist at the phase transition between a topological and a trivial insulator. One such example is graphene, which has two Dirac points at its Fermi surface. A Dirac point is characterized by four degenerate states that disperse linearly with momentum around a single point $\mathbf{k}$ in the Brillouin zone. The resulting low energy theory is pseudorelativistic, and it is responsible for many of the interesting properties of graphene [2]. In a previous communication, we described such Dirac points occurring as symmetry-protected fourfold degeneracies in three-dimensional crystal systems. Such a Dirac point was encountered first in a tight-binding model of s states on the diamond lattice [3]. We showed that the occurrence of this Dirac point is a feature of the symmetry of diamond, which occurs in space group 227. While no realistic system of atoms in a primitive diamond lattice produces this feature, through first-principles calculations we found that substituting bismuth for silicon in β-cristobalite, also in space group 227, elevates a candidate Dirac point degeneracy to the Fermi level, making BiO_2 the first realistic Dirac semimetal proposed [4]. While this material is predicted to be metastable, it is highly unfavorable thermodynamically. This led us to consider alternative crystal structures and symmetries. Three-dimensional Dirac points have also been predicted to exist at the phase transition between a topological and a normal insulator when inversion symmetry is present [5,6]. If either inversion or time-reversal symmetry is broken at the transition, a Dirac point separates into Weyl points which have been shown to exist in Refs. [7–9]. Here we find, on the basis of density functional theory and tight-binding calculations, that a family of three-dimensional materials in a distorted spinel structure supports robust Dirac points in their bulk electronic spectra. A common characteristic of these materials is the presence of a hierarchy of chainlike substructures created by the bismuth atoms in the A site of the crystal structure.

The spinel structure hosts a family of chalcogenides which have the general formula AB_2X_4. A and B are cations that are coordinated by anions of species X, which may be O, S, Se, or Te. The A sites are tetrahedrally coordinated in a diamond lattice, with the octahedrally coordinated B sites in the interstices [10]. Most known spinels are insulators with band gaps of a few eV; this natural tendency toward insulating behavior makes the spinel structure a prime candidate to host a material with a distinct Dirac point degeneracy formed by bands that do not elsewhere cross the Fermi level. By contrast, though the Laves structure contains the required symmetry for a Dirac point, materials in this structure tend to be metallic and our attempts to engineer Dirac semimetals in this structure were plagued by additional band crossings at the Fermi level.

$BiAl_2O_4$ and $BiSc_2O_4$ in the spinel structure exhibit Dirac points at the X points in the Brillouin zone (BZ). However, these materials are not stable and spontaneously break symmetry. Fortunately, one of the child symmetry groups is space group 74, which our crystallographic symmetry criteria [4] admit as a potential host for a Dirac semimetal. As shown in Fig. 1, the cubic unit cell distorts to an orthorhombic cell and the bismuth atoms shift from their previous locations along one of the axes of twofold rotation symmetry in the diamond lattice. This symmetry breaking also distinguishes the two B atoms of the formula unit, which we label B' and B'' Figs. 1 and 2, so that the composition becomes $BiB'B''O_4$. While this new space group has much lower symmetry, it inherits the nonsymmorphic symmetry of diamond and retains one of the three Dirac points among its representations. This Dirac point occurs at the point T in the BZ and, as in diamond, there is a gap at W determined by the strength of the spin-orbit interaction. The effects of reduced symmetry are manifest in the elongation of the octahedral cages of the B' site. This allows the diamond lattice of bismuth to separate into distinct, parallel zig-zag chains. Through first principles DFT calculations we have determined that $BiZnSiO_4$, $BiCaSiO_4$,

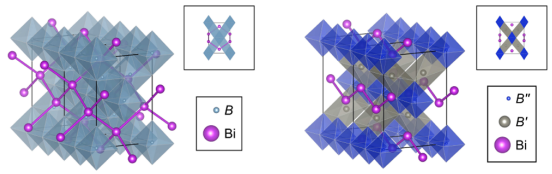

(a)227 (b)74

FIG. 1 (color online). The (a) spinel and (b) distorted spinel structures. Conventionally, the high-symmetry spinel unit cell is cubic; here we have chosen a reduced supercell allowing for direct comparison with the distorted structure. The A sites, populated by Bi, are surrounded by a tetrahedral oxygen cage (not shown for clarity) and the B sites are surrounded by octahedral oxygen cages. In the high-symmetry spinel all Bi neighbors are equidistant, and the Bi atoms form a diamond lattice. Upon distortion, bonds lying in the (0, 1, 0) plane elongate, and the structure can be described as coupled, close-packed, corrugated chains running parallel to [0, 1, 0].

$BiAlInO_4$, and $BiMgSiO_4$ are each metastable and exhibit Dirac point degeneracies at T with no other band crossings at the Fermi level (Fig. 3). Both the crystal and electronic structures are very similar for these materials, and in the following we take $BiZnSiO_4$ to be representative of all four. For these electronic structure and atomic relaxation calculations, we used the plane wave density functional theory package QUANTUM ESPRESSO [11] and designed nonlocal pseudopotentials [12,13] with spin-orbit interaction generated by OPIUM. For all calculations an energy cutoff of 50 Ry and k-point grids of $8 \times 8 \times 8$ for the primitive cell were used.

The states near the Fermi surface are dominated by p-like states on the Bi atoms, as revealed by the angular-momentum-projected density of states in Fig. 4(a), suggesting that each Bi possesses a pair of $5s$ electrons and an unpaired $5p$ electron. This contrasts with both the Fu-Kane-Mele tight-binding model and BiO_2, where the electronic character of the Dirac point derives from an unpaired $5s$ electron. The presence of an unpaired electron is required by symmetry considerations. Nonsymmorphic space groups have at least one sublattice degree of freedom, and at the $\mathbf{k}$ points hosting Dirac points, the only representations are fourfold. Thus, for a fourfold degeneracy to be bisected by the Fermi level there must be an odd number of electrons per formula unit. This symmetry constraint signifies physics being driven by these unpaired electrons. In Fig. 4(c) the Bloch states (excluding the spin degree of freedom) of the Dirac point degeneracy are shown, with a cartoon representation in Fig. 4(b) added for clarity. The character of these states confirms that the unpaired p electrons give rise to the observed Dirac point physics: the two states are related by the symmetry between the two bismuth sublattices that makes the space group nonsymmorphic. Additionally, the system must lie at a critical point between the two configurations where bismuth atoms pair into dimers and is protected by the sublattice symmetry in all three directions; otherwise the interaction between the zig-zag chains could gap the system. This symmetry, which prevents the unpaired electrons from forming bonds in either direction, only belongs to the little group at T; elsewhere it is absent and the degeneracy between the two states is lifted. These chains are reminiscent of polyacetylene, which is characterized by a pattern of alternating single and double bonds along carbon sites leading to a twofold degenerate ground state. This suggests that the individual chains of bismuth sites behave like coupled one-dimensional metal wires running through an otherwise insulating structure. An isolated chain of this kind would be described by the Su-Schrieffer-Heeger [14] model and would suffer from the Peierls instability intrinsic to the half-filled state, breaking the Dirac point. However, the coupling between the chains (Fig. 2) requires a three-dimensional model, and the stability against dimerization depends on microscopic details. First, upon dimerization, the oxidation state of bismuth becomes defined as 2+. This is highly unfavorable for bismuth, which is known to prefer oxidation states of 3+ or 5+. Second, the other cations are small, encouraging a more closely packed lattice and increasing the favorability of the delocalized, metallic character of the Dirac point. Thus the critical point, where the oxidation state of bismuth is formally undefined and the unpaired electrons are delocalized, is locally stable.

Focusing now on the bismuth lattice, Fig. 2 shows an annotated structure of a distorted spinel. The bismuth atoms form a chainlike structure going into the plane, and adjacent chains have a different ordering of the two types of bismuth atoms. Figure 2(a) illustrates chains of α- and β-type Bi atoms along the y axis, while Fig. 2(b) illustrates that adjacent atoms along the x and z axes form an additional chainlike structure. Therefore the Dirac point at T can be understood to be arising from three levels of chainlike structures, resulting in a Dirac point that is protected by the sublattice symmetry of space group 74.

We may model the low-energy theory of distorted spinels by a tight-binding model of p states on the Bi atoms. The two bismuth atoms in each unit cell each have p_x, p_y, and p_z orbitals. We distinguish between the two bismuth sites (and associated sublattices) with the labels A and B. There are four bonds possible for each site; these are $\mathbf{d}^{1\pm} = (\pm a/2, 0, [1-2\gamma]c)$ and $\mathbf{d}^{2\pm} = (0, \pm b/2, 2\gamma c)$, where a, b, and c are the lengths of the orthorhombic lattice vectors, and γ describes an internal distortion; when $a = b = c/\sqrt{2}$ and $\gamma = 1/8$, the lattice becomes diamond. Excluding spin for the moment, the tight-binding Hamiltonian becomes

$$\mathcal{H}_{\mathrm{tb}} = \sum_{\langle ij \rangle} c^{\dagger}_{i,\alpha} c_{j,\beta} [(t_\sigma - t_\pi)(\alpha \cdot \mathbf{d}_{ij})(\beta \cdot \mathbf{d}_{ij}) + t_\pi(\alpha \cdot \beta)]. \quad (1)$$

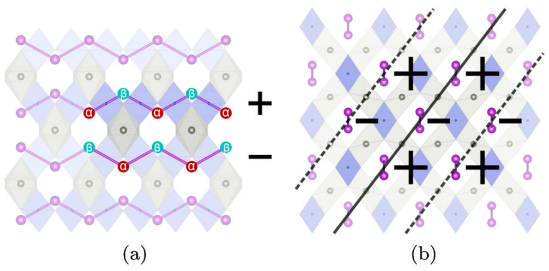

FIG. 2 (color online). The distorted spinel structure with the Bi network annotated. B'' cages are blue, B' cages are gray, and the Bi atoms are in purple. The chains (a) are composed of Bi atoms with alternating bond directions, labeled α and β, forming chains with distinct orientations from their nearest neighbors, signified by $+$ and $-$. Running parallel to [0, 1, 0], the alternatingly oriented chains form their own chainlike structure in the [1, 0, 1] direction, so that each chain is now an object coupling to its neighbors in 1D. The resulting parallel planes of alternating sense (denoted by solid and dashed lines), constructed from the sheets of coupled chains, themselves couple with one another in the [1, 0, −1] direction. Thus, at each level of structure the elements (atoms, chains, and planes) alternate in orientation along a particular direction, resulting in a fourfold representation for a point on the BZ surface corresponding to one half of a reciprocal lattice vector for each of those directions, and a Dirac point at the Fermi level for half-filling.

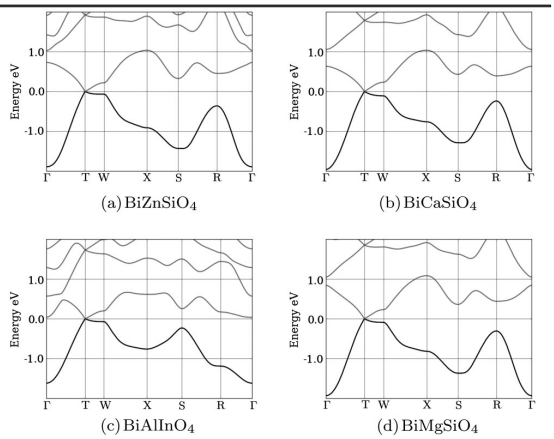

FIG. 3. The band structures of $BiZnSiO_4$ (a), $BiCaSiO_4$ (b), $BiAlInO_4$ (c), and $BiMgSiO_4$ (d) in the distorted spinel structure all contain a Dirac point at T that is completely split along the line in the Brillouin zone from T to W due to the spin orbit interaction between the bismuth sites in the lattice.

The bismuth sites are indexed by i and j, and the sets of p-orbital orientations for site i are labeled by α whereas those for site j are labeled by β, which may be the unit vectors $\hat{x}$, $\hat{y}$, and $\hat{z}$. t_σ and t_π are phenomenological coupling parameters for the σ and π character of the p-p bonds, and $\mathbf{d}_{ij}$ is one of the aforementioned bond vectors that connect sites i and j.

The resulting Hamiltonian produces three pairs of bands, each with a degeneracy from T to W, with bonding and antibonding pairs split off below and above the middle nonbonding pair by energy proportionate to $|t_\sigma - t_\pi|$. Since each bismuth contributes a single electron, we expect the lowest, bonding pair of bands to be half-filled. By inspection we find that these bands at T are dominated by the p orbitals in the plane of the chain, corroborating our first principles results, and confirming that the crucial physics is due to the bismuth lattice. Introducing a spin-orbit term of the form

$$\mathcal{H}_{\mathrm{so}} = \sum_{\ll ij \gg, ss', \alpha\beta} i\lambda_{i\alpha j\beta} \mathbf{d}^1_{ij} \times \mathbf{d}^2_{ij} \cdot \vec{\sigma}_{ss'} c^\dagger_{i,\alpha s} c_{j,\beta,s'}, \qquad (2)$$

where $\mathbf{d}^1_{ij}$ and $\mathbf{d}^2_{ij}$ are nearest neighbor bond vectors that connect sites i and j on the same sublattice, we find that the degeneracies at W are split, allowing Dirac points at T. The effect, however, is not strong enough to mix the three sets of bands with one another, again in agreement with first-principles calculations. Removing the distortion in space group 74 to restore the diamond lattice in Eq. (2) provides the three Dirac points originally known to exist at the X points in diamond. Thus, high symmetry diamond exists as a critical point between the single Dirac-point phases allowed by the three directions in which the symmetry may be reduced to space group 74. This provides a simple understanding of how the Dirac point in diamond is connected to the Dirac point in space group 74.

To evaluate the possibility of synthesizing a Dirac semimetal in the laboratory, we calculated the energy difference associated with synthesizing $ZnBiSiO_4$ from zinc silicate, bismuth metal, and oxygen gas, and found that the $ZnBiSiO_4$ distorted spinel structure is lower in energy by about 0.25 eV per formula unit. A major challenge involved in this synthesis would be to prevent bismuth from further oxidizing and causing the constituents to segregate. The conventionally determined oxidation state of bismuth appears to pose a significant obstacle in synthesizing the proposed materials. However, that this oxidation state characterizes nearby insulating states is crucial to providing an odd electron formula unit and stabilizing the Dirac-semimetal state. Similar configurations of bismuth atoms have been achieved in the laboratory in the construction of bulk materials built from stacks of two-dimensional topological insulators [15]. We therefore propose that synthesis be conducted under reducing conditions (high temperature and low partial pressure of O_2).

Finally, we note that additional symmetry breaking may allow access to exotic insulating phases. The low-energy theory at the Fermi surface can be written as $\mathcal{H}(\mathbf{k}) = v_x k_x \gamma_x + v_y k_y \gamma_y + v_z k_z \gamma_z$, centered at T, where v_i are the Fermi velocities and γ_i are 4×4 Dirac matrices.

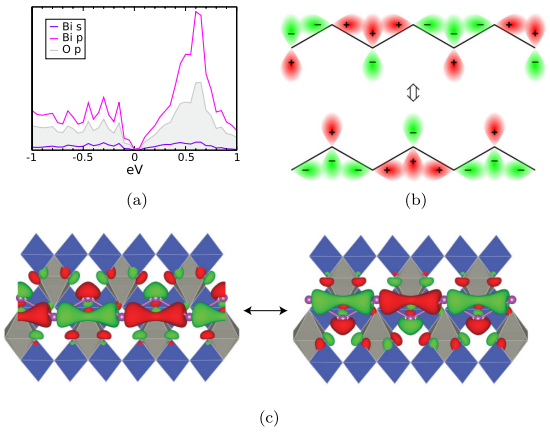

FIG. 4 (color online). Projected density of states near the Dirac point in the $ZnBiSiO_4$ structure (a). States near the Dirac point are primarily Bi p states, with a vanishing density at the Fermi energy. The angular portion of the wave functions (i.e., without the spin degree of freedom) of the $ZnBiSiO_4$ structure at T is shown in (c), with a cartoon depiction in (b) emphasizing their p-like nature. The neighboring bismuth sites interact in a way that can be depicted as chains of Bi p orbitals running through an insulating structure, in which individual chains are analogous to polyacetylene; nonsymmorphic operation of "inversion followed by translation between A sites" results in an equivalent but different state, creating a twofold degeneracy at the Dirac point, which then becomes fourfold due to the spin degree of freedom. Breaking inversion symmetry in this structure is analogous to having inequivalent coupling constants between Bi sites and single and double bonds in polyacetylene, and will lift the degeneracy, gapping the system.

The Dirac matrices are constrained by the invariance of $\mathcal{H}(\mathbf{k})$ under the little group at T. Orienting the k_z axis to point along the line from T to Γ, $\mathcal{H}(\mathbf{k})$ takes the form,

$$\mathcal{H}(\mathbf{k}) = v_x k_x \sigma_x \otimes \sigma_z + v_y k_y (\cos\theta \sigma_x \otimes \sigma_x + \sin\theta \sigma_x \otimes \sigma_y) + v_z k_z \sigma_y \otimes \mathbb{I}. \quad (3)$$

Here θ is an arbitrary real parameter, σ_i are the usual Pauli matrices, and $\mathbb{I}$ is the 2×2 identity matrix. The exact values of θ and v_i depend on microscopic features.

The elements of the little group that stabilize the Dirac point at T are: mirror symmetry $\mathcal{M}_z$ about the $k_x k_y$ plane, sublattice (inversion) symmetry $\mathcal{I}$, and time-reversal symmetry Θ. In the basis of Eq. (3), these operators can be represented as, $\mathcal{M}_z = \sigma_x \otimes \mathbb{I}$, $\mathcal{I} = \sigma_z \otimes \mathbb{I}$, and $\Theta = i\sigma_y \otimes \mathbb{I} K$ where K denotes complex conjugation. Symmetry breaking perturbations lead to insulating (topological and normal) as well as topological semimetallic (Weyl) phases. The distorted spinel structures discussed in this Letter, if engineered or discovered naturally, can be used to access such phases. Dirac semimetals are unique in that they exist at a multicritical point from which many exotic insulating and topological semimetallic phases can be reached [4].

We emphasize that the crucial feature of these materials is the network of interpenetrating, symmetry-related sublattices of bismuth atoms with unpaired electrons, a physical manifestation of the symmetry-derived result that Dirac points can only exist in nonsymmorphic space groups on the BZ surface. The rest of the atoms of the lattice can be thought of as an insulating scaffolding that stabilizes this metallic bismuth network that hosts the Dirac point. The combination of close packing and unconventional oxidation state reduces the tendency towards dimerization and the system remains at the critical point of this half-filled state. These offer important insight into both the physics and materials science of the Dirac semimetal state, and will inform efforts to realize such a material.

This work was supported in part by the MRSEC program of the National Science Foundation under Grant No. DMR11-20901 (S. M. Y.), by the Department of Energy under Grant No. FG02-ER45118 (E. J. M. and S. Z.), and by the National Science Foundation under Grants No. DMR11-24696 (A. M. R.) and No. DMR09-06175 (C. L. K.). J. A. S. was supported by the REU program at LRSM, University of Pennsylvania, and by the Department of Energy under Grant No. DE-FG02-07ER46431. S. M. Y. acknowledges computational support from the High Performance Computing Modernization Office.

Note added.—We have recently learned of two independent experiments [16,17] that report the existence of a three-dimensional Dirac point in Cd_3As_2. We note that the mechanism underpinning the Dirac point in this material combines band inversion with rotational symmetry [18], which is different from our theory that relies solely on crystal symmetry. However, these experiments show that the Dirac semimetal phase is stable, despite the Fermi level being somewhat above the Dirac point due to disorder, and that the Dirac point is responsible for the high electron mobility in Cd_3As_2. We hope that these insights will accelerate efforts to observe similar Dirac points in distorted spinels.

*Corresponding author.
stjulia@sas.upenn.edu

[1] C. L. Kane and E. J. Mele, Phys. Rev. Lett. **95**, 226801 (2005).
[2] A. H. C. Neto, F. Guinea, N. M. R. Peres, K. S. Novoselov, and A. K. Geim, Rev. Mod. Phys. **81**, 109 (2009).
[3] L. Fu, C. L. Kane, and E. J. Mele, Phys. Rev. Lett. **98**, 106803 (2007).
[4] S. M. Young, S. Zaheer, J. C. Y. Teo, C. L. Kane, E. J. Mele, and A. M. Rappe, Phys. Rev. Lett. **108**, 140405 (2012).
[5] S. Murakami, New J. Phys. **9**, 356 (2007).

[6] S. M. Young, S. Chowdhury, E. J. Walter, E. J. Mele, C. L. Kane, and A. M. Rappe, Phys. Rev. B **84**, 085106 (2011).
[7] X. Wan, A. M. Turner, A. Vishwanath, and S. Y. Savrasov, Phys. Rev. B **83**, 205101 (2011).
[8] A. A. Burkov and L. Balents, Phys. Rev. Lett. **107**, 127205 (2011).
[9] G. B. Halász and L. Balents, Phys. Rev. B **85**, 035103 (2012).
[10] J. K. Burdett, G. D. Price, and S. L. Price, J. Am. Chem. Soc. **104**, 92 (1982).
[11] P. Giannozzi *et al.*, J. Phys. Condens. Matter **21**, 395502 (2009).
[12] A. M. Rappe, K. M. Rabe, E. Kaxiras, and J. D. Joannopoulos, Phys. Rev. B **41**, 1227 (1990).
[13] N. J. Ramer and A. M. Rappe, Phys. Rev. B **59**, 12 471 (1999).
[14] W. P. Su, J. R. Schrieffer, and A. J. Heeger, Phys. Rev. Lett. **42**, 1698 (1979).
[15] B. Rasche, A. Isaeva, M. Ruck, S. Borisenko, V. Zabolotnyy, B. Büchner, K. Koepernik, C. Ortix, M. Richter, and J. van den Brink, Nat. Mater. **12**, 422 (2013).
[16] S. Borisenko *et al.*, arXiv:1309.7978.
[17] M. Neupane *et al.*, arXiv:1309.7982.
[18] Z. Wang, H. Weng, Q. Wu, X. Dai, and Z. Fang, Phys. Rev. B **88**, 125427 (2013).

BIBLIOGRAPHY

Abrikosov, A. A., Gorkov, L. P., and Dzialoshinski, I. E. (1965). *Quantum field theoretical methods in statistical physics*, volume 4. Pergamon.

Berding, M. A., Krishnamurthy, S., Sher, A., and Chen, A. (1987). Electronic and transport properties of hgcdte and hgznte. *Journal of Vacuum Science & Technology A*, 5(5):3014–3018.

Bernevig, B. A., Hughes, T. L., and Zhang, S.-C. (2006). Quantum spin hall effect and topological phase transition in hgte quantum wells. *Science*, 314(5806):1757–1761.

Borisenko, S., Gibson, Q., Evtushinsky, D., Zabolotnyy, V., Buechner, B., and Cava, R. J. (2013). Experimental realization of a three-dimensional dirac semimetal. *arXiv preprint arXiv:1309.7978*.

Bradley, C. and Cracknell, A. (1976). *The mathematical theory of symmetry in solids*. Oxford: Clarendon.

Burdett, J. K., Price, G. D., and Price, S. L. (1982). Role of the crystal-field theory in determining the structures of spinels. *Journal of the American Chemical Society*, 104(1):92–95.

Burkov, A. A. and Balents, L. (2011). Weyl semimetal in a topological insulator multilayer. *Phys. Rev. Lett.*, 107:127205.

Calvert, L. and Villars, P. (1991). Pearsons handbook of crystallographic data for intermetallic phases. *ASM, Materials Park, OH*.

Castro Neto, A. H., Guinea, F., Peres, N. M. R., Novoselov, K. S., and Geim, A. K. (2009). The electronic properties of graphene. *Rev. Mod. Phys.*, 81:109–162.

Dresselhaus, G. (1955). Spin-orbit coupling effects in zinc blende structures. *Phys. Rev.*, 100:580–586.

Fang, C., Gilbert, M. J., Dai, X., and Bernevig, B. A. (2012). Multi-weyl topological semimetals stabilized by point group symmetry. *Phys. Rev. Lett.*, 108:266802.

Faurie, J. P., Sivananthan, S., Chu, X., and Wijewarnasuriya, P. S. (1986). Molecular beam epitaxial growth of a novel strained layer type iii superlattice system: Hgteznte. *Applied Physics Letters*, 48(12):785–787.

Fu, L. and Kane, C. L. (2007). Topological insulators with inversion symmetry. *Phys. Rev. B*, 76:045302.

Fu, L., Kane, C. L., and Mele, E. J. (2007). Topological insulators in three dimensions. *Phys. Rev. Lett.*, 98:106803.

Giannozzi, P., Baroni, S., Bonini, N., Calandra, M., Car, R., Cavazzoni, C., Ceresoli, D., Chiarotti, G. L., Cococcioni, M., Dabo, I., Corso, A. D., de Gironcoli, S., Fabris, S., Fratesi, G., Gebauer, R., Gerstmann, U., Gougoussis, C., Kokalj, A., Lazzeri, M., Martin-Samos, L., Marzari, N., Mauri, F., Mazzarello, R., Paolini, S., Pasquarello, A., Paulatto, L., Sbraccia, C., Scandolo, S., Sclauzero, G., Seitsonen, A. P., Smogunov, A., Umari, P., and Wentzcovitch, R. M. (2009). Quantum espresso: a modular and open-source software project for quantum simulations of materials. *Journal of Physics: Condensed Matter*, 21(39):395502.

Halász, G. B. and Balents, L. (2012). Time-reversal invariant realization of the weyl semimetal phase. *Phys. Rev. B*, 85:035103.

Hamermesh, M. (1989). *Group theory and its application to physical problems*. Courier Dover Publications.

Hasan, M. Z. and Kane, C. L. (2010). *Colloquium*: Topological insulators. *Rev. Mod. Phys.*, 82:3045–3067.

Hosur, P., Parameswaran, S. A., and Vishwanath, A. (2012). Charge transport in weyl semimetals. *Phys. Rev. Lett.*, 108:046602.

Hsieh, D., Xia, Y., Qian, D., Wray, L., Meier, F., Dil, J. H., Osterwalder, J., Patthey, L., Fedorov, A. V., Lin, H., Bansil, A., Grauer, D., Hor, Y. S., Cava, R. J., and Hasan, M. Z. (2009). Observation of time-reversal-protected single-dirac-cone topological-insulator states in bi_2te_3 and sb_2te_3. *Phys. Rev. Lett.*, 103:146401.

Jay-Gerin, J.-P., Aubin, M., and Caron, L. (1977). The electron mobility and the static dielectric constant of cd3as2 at 4.2 k. *Solid State Communications*, 21(8):771 – 774.

Jeon, S., Zhou, B. B., Gyenis, A., Feldman, B. E., Kimchi, I., Potter, A. C., Gibson, Q. D., Cava, R. J., Vishwanath, A., and Yazdani, A. (2014). Landau quantization and quasiparticle interference in the three-dimensional diracsemimetal cd3as2. *Nature Materials*, pages –.

Kane, C. L. and Mele, E. J. (2005a). Quantum spin hall effect in graphene. *Phys. Rev. Lett.*, 95:226801.

Kane, C. L. and Mele, E. J. (2005b). Z_2 topological order and the quantum spin hall effect. *Phys. Rev. Lett.*, 95:146802.

Konig, M., Wiedmann, S., Brne, C., Roth, A., Buhmann, H., Molenkamp, L. W., Qi, X.-L., and Zhang, S.-C. (2007). Quantum spin hall insulator state in hgte quantum wells. *Science*, 318(5851):766–770.

Liu, J., Xu, Y., Wu, J., Gu, B.-L., Zhang, S., and Duan, W. (2014a). Manipulating topological phase transition by strain. *Acta Crystallographica Section C: Structural Chemistry*, 70(2):118–122.

Liu, Z., Zhou, B., Zhang, Y., Wang, Z., Weng, H., Prabhakaran, D., Mo, S.-K., Shen, Z., Fang, Z., Dai, X., et al. (2014b). Discovery of a three-dimensional topological dirac semimetal, na3bi. *Science*, 343(6173):864–867.

Mañes, J. L. (2012). Existence of bulk chiral fermions and crystal symmetry. *Phys. Rev. B*, 85:155118.

Maciejko, J. and Nandkishore, R. (2014). Weyl semimetals with short-range interactions. *Phys. Rev. B*, 90:035126.

Madelung, O., Rössler, U., and Schulz, M. (2010). Mercury telluride (hgte) band structure, band energies at symmetry points, landolt-brnstein - group iii condensed matter.

Moore, J. E. and Balents, L. (2007). Topological invariants of time-reversal-invariant band structures. *Phys. Rev. B*, 75:121306.

Murakami, S. (2007). Phase transition between the quantum spin hall and insulator phases in 3d: emergence of a topological gapless phase. *New Journal of Physics*, 9(9):356.

Nandkishore, R., Huse, D. A., and Sondhi, S. L. (2014). Rare region effects dominate weakly disordered three-dimensional dirac points. *Phys. Rev. B*, 89:245110.

Neupane, M., Xu, S.-Y., Sankar, R., Alidoust, N., Bian, G., Liu, C., Belopolski, I., Chang, T.-R., Jeng, H.-T., Lin, H., et al. (2014). Observation of a three-dimensional topological dirac semimetal phase in high-mobility cd_3as_2. *Nature communications*, 5.

Novoselov, K. S., Geim, A. K., Morozov, S. V., Jiang, D., Zhang, Y., Dubonos, S. V., Grigorieva, I. V., and Firsov, A. A. (2004). Electric field effect in atomically thin carbon films. *Science*, 306(5696):666–669.

Potter, A. C., Kimchi, I., and Vishwanath, A. (2014). Quantum Oscillations from Surface Fermi-Arcs in Weyl and Dirac Semi-Metals. *ArXiv e-prints*.

Ramer, N. J. and Rappe, A. M. (1999). Designed nonlocal pseudopotentials for enhanced transferability. *Phys. Rev. B*, 59:12471–12478.

Rappe, A. M., Rabe, K. M., Kaxiras, E., and Joannopoulos, J. D. (1990). Optimized pseudopotentials. *Phys. Rev. B*, 41:1227–1230.

Roy, R. (2009). Topological phases and the quantum spin hall effect in three dimensions. *Phys. Rev. B*, 79:195322.

Sa, B., Zhou, J., Sun, Z., and Ahuja, R. (2012). Strain-induced topological insulating behavior in ternary chalcogenide $ge_2sb_2te_5$. *EPL (Europhysics Letters)*, 97(2):27003.

Sato, T., Segawa, K., Kosaka, K., Souma, S., Nakayama, K., Eto, K., Minami, T., Ando, Y., and Takahashi, T. (2011). Unexpected mass acquisition of dirac fermions at the quantum phase transition of a topological insulator. *Nature Physics*, 7(11):840–844.

Scott, M. W. (1969). Energy gap in hg1-xcdxte by optical absorption. *Journal of Applied Physics*, 40(10):4077–4081.

Sekine, A. and Nomura, K. (2013). Electron correlation induced spontaneous symmetry breaking and weyl semimetal phase in a strongly spinorbit coupled system. *Journal of the Physical Society of Japan*, 82(3):033702.

Sekine, A. and Nomura, K. (2014). Stability of Multi-Node Dirac Semimetals against Strong Long-Range Correlation. *ArXiv e-prints*.

Sher, A., Eger, D., Zemel, A., Feldstein, H., and Raizman, A. (1986). Properties of hg1-xznxte grown by liquid-phase epitaxy. *Journal of Vacuum Science & Technology A*, 4(4):2024–2027.

Steinberg, J. A., Young, S. M., Zaheer, S., Kane, C. L., Mele, E. J., and Rappe, A. M. (2014). Bulk dirac points in distorted spinels. *Phys. Rev. Lett.*, 112:036403.

Su, W. P., Schrieffer, J. R., and Heeger, A. J. (1979). Solitons in polyacetylene. *Phys. Rev. Lett.*, 42:1698–1701.

Svane, A., Christensen, N. E., Cardona, M., Chantis, A. N., van Schilfgaarde, M., and Kotani, T. (2011). Quasiparticle band structures of β-hgs, hgse, and hgte. *Phys. Rev. B*, 84:205205.

Thornton, G. (1977). A neutron diffraction study of-sb2o4. *Acta Crystallographica Section B: Structural Crystallography and Crystal Chemistry*, 33(4):1271–1273.

Wallace, P. R. (1947). The band theory of graphite. *Phys. Rev.*, 71:622–634.

Wan, X., Turner, A. M., Vishwanath, A., and Savrasov, S. Y. (2011). Topological semimetal and fermi-arc surface states in the electronic structure of pyrochlore iridates. *Phys. Rev. B*, 83:205101.

Wang, Z., Sun, Y., Chen, X.-Q., Franchini, C., Xu, G., Weng, H., Dai, X., and Fang, Z. (2012). Dirac semimetal and topological phase transitions in A_3bi (a = Na, k, rb). *Phys. Rev. B*, 85:195320.

Wang, Z., Weng, H., Wu, Q., Dai, X., and Fang, Z. (2013). Three-dimensional dirac semimetal and quantum transport in cd_3as_2. *Phys. Rev. B*, 88:125427.

Wang, Z. and Zhang, S.-C. (2013). Chiral anomaly, charge density waves, and axion strings from weyl semimetals. *Phys. Rev. B*, 87:161107.

Wei, H., Chao, S.-P., and Aji, V. (2012). Excitonic phases from weyl semimetals. *Phys. Rev. Lett.*, 109:196403.

Weil, R., Nkum, R., Muranevich, E., and Benguigui, L. (1989). Ferroelectricity in zinc cadmium telluride. *Phys. Rev. Lett.*, 62:2744–2746.

Xu, G., Weng, H., Wang, Z., Dai, X., and Fang, Z. (2011). Chern semimetal and the quantized anomalous hall effect in hgcr2se4. *Phys. Rev. Lett.*, 107:186806.

Young, S. M., Chowdhury, S., Walter, E. J., Mele, E. J., Kane, C. L., and Rappe, A. M. (2011). Theoretical investigation of the evolution of the topological phase of bi_2se_3 under mechanical strain. *Phys. Rev. B*, 84:085106.

Young, S. M., Zaheer, S., Teo, J. C. Y., Kane, C. L., Mele, E. J., and Rappe, A. M. (2012). Dirac semimetal in three dimensions. *Phys. Rev. Lett.*, 108:140405.

Zaheer, S., Young, S. M., Cellucci, D., Teo, J. C. Y., Kane, C. L., Mele, E. J., and Rappe, A. M. (2013). Spin texture on the fermi surface of tensile-strained hgte. *Phys. Rev. B*, 87:045202.

Zdanowicz, L., Portal, J., and Zdanowicz, W. (1983). Shubnikov-de haas effect in amorphous cd3as2. In Landwehr, G., editor, *Application of High Magnetic Fields in Semiconductor Physics*, volume 177 of *Lecture Notes in Physics*, pages 386–395. Springer Berlin Heidelberg.

Zhang, H., Liu, C.-X., Qi, X.-L., Dai, X., Fang, Z., and Zhang, S.-C. (2009). Topological insulators in $bi_2se_3, bi_2te_3 and sb_2te_3$ with a single dirac cone on the surface. *Nature Physics*, 5(6):438–442.